

# A REFINED ESTIMATE OF THE IONIZING EMISSIVITY FROM GALAXIES AT $z \simeq 3$ : SPECTROSCOPIC FOLLOW-UP IN THE SSA22A FIELD<sup>1</sup>

DANIEL B. NESTOR, ALICE E. SHAPLEY<sup>2</sup>, KATHERINE A. KORNEI

Department of Astronomy, University of California, Los Angeles, 430 Portola Plaza, Los Angeles, CA 90095

CHARLES C. STEIDEL

California Institute of Technology, MS 105–24, Pasadena, CA 91125

BRIAN SIANA

Department of Physics and Astronomy, University of California, Riverside, CA 92521

*Draft version January 3, 2013*

## ABSTRACT

We investigate the contribution of star-forming galaxies to the ionizing background at  $z \sim 3$ , building on previous work based on narrowband (NB3640) imaging in the SSA22a field. We use new Keck/LRIS spectra of Lyman break galaxies (LBGs) and narrowband-selected Ly $\alpha$  emitters (LAEs) to measure redshifts for 16 LBGs and 87 LAEs at  $z > 3.055$ , such that our NB3640 imaging probes the Lyman-continuum (LyC) region. When we include the existing set of spectroscopically-confirmed LBGs, our total sample with  $z > 3.055$  consists of 41 LBGs and 91 LAEs, of which nine LBGs and 20 LAEs are detected in our NB3640 image. With our combined imaging and spectroscopic data sets, we critically investigate the origin of NB3640 emission for detected LBGs and LAEs. We remove from our samples 3 LBGs and 3 LAEs with spectroscopic evidence of contamination of their NB3640 flux by foreground galaxies, and statistically model the effects of additional, unidentified foreground contaminants. The resulting contamination and LyC-detection rates, respectively, are  $62 \pm 13\%$  and  $8 \pm 3\%$  for our LBG sample, and  $47 \pm 10\%$  and  $12 \pm 2\%$  for our LAE sample. The corresponding ratios of non-ionizing UV to LyC flux-density, corrected for intergalactic medium (IGM) attenuation, are  $18.0^{+34.8}_{-7.4}$  for LBGs, and  $3.7^{+2.5}_{-1.1}$  for LAEs. We use these ratios to estimate the total contribution of star-forming galaxies to the ionizing background and the hydrogen photoionization rate in the IGM, finding values larger than, but consistent with, those measured in the Ly $\alpha$  forest. Finally, the measured UV to LyC flux-density ratios imply model-dependent LyC escape fractions of  $f_{esc}^{LyC} \sim 5 - 7\%$  for our LBG sample and  $f_{esc}^{LyC} \sim 10 - 30\%$  for our fainter LAE sample.

*Subject headings:* galaxies: high-redshift – intergalactic medium – cosmology: observations – diffuse radiation

## 1. INTRODUCTION

Identifying the sources of the radiation that re-ionized the intergalactic medium (IGM) at redshift  $z \gtrsim 6$  is a key challenge for observational cosmology. Massive stars in star-forming galaxies are considered the most likely source of the Lyman-continuum (LyC) photons necessary for reionization. QSOs, while also efficient producers of ionizing radiation, appear to be too rare at high redshift to produce sufficient ionizing flux (Hopkins et al. 2007; Cowie et al. 2009). Unfortunately, direct observation of ionizing radiation from high-redshift star-forming galaxies is not possible, as the Universe remains opaque to LyC photons above redshifts  $z \sim 4$  due to the abundance of residual neutral gas in the IGM. Thus, empirical constraints on the sources responsible for reionization come primarily from (i) the determination of the non-ionizing UV luminosity function of the highest-redshift galaxies

currently observable, and (ii) direct measurements of ionizing radiation from lower-redshift analogs of the  $z \gtrsim 6$  galaxies responsible for reionization.

Progress has recently been made in both of the above approaches. Bright, color-selected  $z \sim 6 - 7$  candidate galaxies have recently been spectroscopically confirmed (e.g., Pentericci et al. 2011; Ono et al. 2012; Schenker et al. 2012). Searches for fainter, line-emitting galaxies using narrowband imaging techniques have uncovered significant samples of Ly $\alpha$  emitters (LAEs) at redshifts as high as  $z \sim 7$  (e.g., Krug et al. 2012; Ota et al. 2010; Ouchi et al. 2010). At even higher redshift, deep near-IR observations of the Hubble Ultra Deep Field using the WFC3 camera on the Hubble Space Telescope (*HST*), combined with optical *HST*/ACS data, have revealed populations of redshift  $z \sim 7 - 10$  galaxies (e.g., Bouwens et al. 2010; Bunker et al. 2010; Lorenzoni et al. 2011; McLure et al. 2011; Vanzella et al. 2011; Wilkins et al. 2011; Oesch et al. 2012; Trenti et al. 2012). Among the results of such studies, the emerging  $z \sim 8$  luminosity functions suggest that there are too few bright galaxies to reionize the IGM, implying that relatively low-mass galaxies are important contributors

<sup>1</sup> Based, in part, on data obtained at the W.M. Keck Observatory, which is operated as a scientific partnership among the California Institute of Technology, the University of California, and NASA, and was made possible by the generous financial support of the W.M. Keck Foundation.

<sup>2</sup> David and Lucile Packard Fellow

to the ionizing flux budget.

The effort to unambiguously identify low-redshift analogs of the galaxies responsible for reionization has been difficult. Observations to directly detect ionizing continuum escaping from galaxies at  $0 < z \lesssim 2$  have been unsuccessful (e.g., Malkan et al. 2003; Cowie et al. 2009; Grimes et al. 2009; Siana et al. 2010; Bridge et al. 2010). Thus, searches have turned to the highest redshifts at which the opacity to LyC photons through the IGM,  $\tau_{LyC}$ , is  $\lesssim 1$ , i.e.,  $z \sim 3$ . The expected rest-frame UV flux levels are low at such redshifts, requiring deep observations to identify sources and to detect escaping LyC emission. The low flux levels also complicate the interpretation of presumed detections of LyC flux, as the sky surface density of faint foreground sources is large ( $\sim 75$  arcmin $^{-1}$ ), leading to the possibility of contamination from lower-redshift sources. With these caveats in mind, there have been several reported detections of escaping LyC flux from galaxies at  $z \sim 3$  through both spectroscopy of Lyman break galaxies (LBGs) (Steidel et al. 2001; Shapley et al. 2006) and narrowband imaging of LBGs and LAEs (Iwata et al. 2009; Nestor et al. 2011; Vanzella et al. 2011).

In Nestor et al. (2011), we searched for escaping LyC flux from  $z \geq 3.055$  LBGs and photometrically-selected LAE candidates in the SSA22a field, which contains a large over-density of galaxies at  $z = 3.09$  (Steidel et al. 1998). In that paper we reported the detection of six  $z \geq 3.09$  LBGs and 27 candidate  $z \simeq 3.09$  LAEs through a narrowband filter that is opaque to non-ionizing flux from sources at  $z \gtrsim 3.055$ , and thus probes light blueward of the Lyman limit for sources at  $z \simeq 3.09$ . We interpreted these detections as direct evidence of escaping LyC flux, which we in turn used to estimate the comoving ionizing emissivity,  $\epsilon_{LyC}$ , at  $z \sim 3$ . Our primary conclusions were that the contribution to  $\epsilon_{LyC}$  from star-forming galaxies at  $z \sim 3$  exceeds, but is roughly consistent with, given our uncertainty, that expected from determinations of the photoionization rate in the Ly $\alpha$  forest (e.g., Bolton & Haehnelt 2007; Faucher-Giguère et al. 2008), and that the bulk of this contribution comes from relatively faint sources ( $M_{AB} \gtrsim -20$ ) such as those that compose our sample of LAEs.

Our ability to constrain  $\epsilon_{LyC}$ , however, was limited by our fairly small sample of LBG detections, which is very likely to contain contamination by foreground interlopers (see, e.g., Vanzella et al. 2012). As our seeing-limited observations restricted our ability to account for contamination by foreground galaxies in individual systems, we used a statistical approach for the sample as a whole. Furthermore, many of the results in Nestor et al. (2011) were based on the sample of LAEs, the majority of which were not spectroscopically confirmed. Each of these limitations can be alleviated with follow up spectroscopy. Therefore, in order to increase the size of our LBG sample, we obtained spectra of additional color selected LBG candidates lacking prior spectroscopic redshift confirmation. We also obtained spectra of as many of our narrowband-selected LAE candidates as possible, in order to confirm their redshifts. These data have the additional benefit that, in most cases, we can directly search for evidence of foreground contamination in individual objects. We also obtained particularly deep

spectra of many of the sources having apparent LyC detections, which allow us to perform a detailed analysis (e.g., of the spatial distribution) of the detected Ly $\alpha$ , non-ionizing UV, and LyC fluxes.

The organization of this paper is as follows. In Section 2 we describe the observations and reduction of the data used in this study. We update our LBG and LAE samples based on the results of our new spectroscopy in Section 3. In Section 4 we discuss individual LBGs and LAEs with presumed LyC detections. In Section 5 we describe our techniques for statistically accounting for foreground contamination and attenuation of LyC flux by the IGM. We present updated estimates of  $\epsilon_{LyC}$  and discuss LyC escape fractions in Section 6, and summarize our results in Section 7. Throughout the paper all magnitudes are in the AB system, and we assume a cosmology with  $\Omega_m = 0.3$ ,  $\Omega_\Lambda = 0.7$ , and  $H_0 = 70$  km s $^{-1}$  Mpc $^{-1}$ .

## 2. OBSERVATIONS AND DATA REDUCTION

### 2.1. Photometric Observations and Sample

Our analyses make use of deep multiband imaging available in the SSA22a field. These data, which are described in detail in Nestor et al. (2011), include ground-based broad  $B$ -,  $V$ - and  $R$ -band images and narrowband images with effective wavelengths at  $\lambda \sim 3640\text{\AA}$  and  $\lambda \sim 4980\text{\AA}$  (hereafter NB3640 and NB4980, respectively). The NB3640 and part of the NB4980 data were obtained using the Keck/LRIS imaging spectrograph, while the broadband imaging and the remainder of the NB4980 data were obtained with the Subaru/Suprime-Cam. Additionally, archival *HST*/ACS F814W imaging is available for 70% of the field.

The NB3640 filter has a central wavelength of  $3635\text{\AA}$  and FWHM of  $100\text{\AA}$ . For sources at  $z \simeq 3.09$ , NB3640 samples the rest-frame spectral range  $\lambda \simeq 875 - 900\text{\AA}$ . It is opaque to wavelengths longward of the redshifted Lyman limit for sources above  $z \simeq 3.055$  and therefore provides a clean probe of escaping LyC emission for such galaxies. The effective wavelength of the broad  $R$ -band filter ( $\lambda \simeq 6510\text{\AA}$ ) corresponds to rest-frame  $\lambda \simeq 1600\text{\AA}$  at  $z \simeq 3.09$ . The NB3640- $R$  color is accordingly a measure of the non-ionizing to ionizing UV flux-density ratio,  $F_{UV}/F_{LyC}$ , for galaxies with  $z \geq 3.055$ . The ACS/WFC F814W filter has an effective wavelength of  $\lambda \simeq 8090\text{\AA}$  and also probes the non-ionizing UV continuum at  $z \sim 3.09$ . The footprint of our NB3640 image contains 109 color-selected LBG candidates, of which 28 (including 2 QSOs) have previous spectroscopically confirmed redshifts  $z \geq 3.055$ , as well as 41 LBG candidates without previous spectroscopic confirmation. The footprint also contains 110 LAE candidates identified by Nestor et al. (2011).

LAE candidates were selected using the  $B$ ,  $V$ , and NB4980 data. The NB4980 filter covers redshifted HI Ly $\alpha$   $\lambda 1216\text{\AA}$  for galaxies with  $3.05 \lesssim z \lesssim 3.12$ . We created a linear combination of the broad  $B$  and  $V$  images after scaling to a common photometric zero-point, such that our so-called “ $BV$ ” image has an effective wavelength of  $\lambda \simeq 4980\text{\AA}$ . The  $BV - \text{NB4980}$  color is therefore a measure of Ly $\alpha$  equivalent width for galaxies with  $3.05 \lesssim z \lesssim 3.12$ . The LAEs in the sample described by Nestor et al. (2011) were required to have  $\text{NB4980} \leq 26$  and  $BV - \text{NB4980} \geq 0.7$ , which corresponds to a Ly $\alpha$

rest-frame equivalent width (REW) of  $\gtrsim 20\text{\AA}$ . We also subtracted the  $BV$  image from the NB4980 image to create a so-called “ $LyA$ ” image, which was used to define the centroids of  $Ly\alpha$  emission from the LAE candidates.

## 2.2. Spectroscopic Observations

We performed spectroscopy in the SSA22a field using both shallow and deep observations. The purpose of the shallow observations was to obtain spectroscopic redshifts for LBG and LAE photometric candidates, while the deep observations were intended to provide detailed information for objects with NB3640 detections. Multi-object spectroscopy was performed using the blue arm of the LRIS dichroic spectrograph on Keck I (Oke et al. 1995; Steidel et al. 2004). Nine shallow slit masks were observed over the course of five observing runs in 2009 June, 2009 September, 2010 July, 2010 August, and 2011 May. A single deep mask was observed in 2010 August. Typical exposure times for the shallow masks were 5400 seconds (ranging from 3600 to 6270 seconds), while the deep mask was observed for 23700 seconds. For most runs, the conditions were photometric, with seeing ranging from  $0''.5$  to  $0''.7$ . In 2011 May, when additional data were collected for one of the shallow masks, conditions featured variable cloudiness and seeing ranging from  $0''.8$  to  $1''.0$ .

The primary targets for shallow masks were LBG and LAE photometric candidates without previously-determined spectroscopic redshifts. LBGs with spectroscopic redshifts were added as filler targets on the mask. A total of 50 LBGs and 114 LAEs were targeted on the shallow masks. Slits were centered on the detections in the NB4980 (i.e.,  $Ly\alpha$ ) for LAEs, and in the  $R$ -band (i.e., rest-frame UV continuum) for LBGs. Seven out of nine shallow masks were observed using a 300 line  $\text{mm}^{-1}$  grism blazed at 5000  $\text{\AA}$ , along with the “d680” dichroic beam splitter, sending light with wavelengths bluer than  $\sim 6800\text{\AA}$  to the blue arm of LRIS. The spectral resolution for these masks was  $R = 530$ . The two remaining shallow masks were observed at higher spectral resolution using a 600 line  $\text{mm}^{-1}$  grism blazed at 4000  $\text{\AA}$ , one with the “d560” dichroic (splitting the incoming light beam at  $\sim 5600\text{\AA}$ ), and the other with the “d680” dichroic. The spectral resolution for these two masks was  $R = 1200$ .

The primary targets for the deep mask were LBGs and LAEs with NB3640 detections. A sample of 4 LBGs and 13 LAEs with NB3640 detections were targeted on the deep mask (along with one LBG and 4 LAEs lacking NB3640 detections, but added as filler). Slits for objects with NB3640 detections were centered on the detections in the NB3640 image (i.e.,  $LyC$  for objects at  $z \geq 3.055$ ), while the NB4980 and  $R$ -band detections were used, respectively, for centering the slits for the filler LAEs and LBG without NB3640 detections. The deep mask was observed using a 400 line  $\text{mm}^{-1}$  grism blazed at 3400  $\text{\AA}$ , along with the “d680” dichroic beam splitter, sending light with wavelengths bluer than  $\sim 6800\text{\AA}$  to the blue arm of LRIS. The spectral resolution for this mask was  $R = 700$ .

The data were primarily reduced using IRAF tasks, with scripts designed for cutting up the multi-object slit-mask images into individual slitlets, flat-fielding using spectra of the twilight sky, rejecting cosmic rays, sub-

tracting the sky background, averaging individual exposures into final stacked two-dimensional spectra, extracting to one dimension, wavelength and flux calibrating, and shifting into the vacuum frame. These procedures are described in detail in Steidel et al. (2003). There were a couple of notable differences in the data reduction procedures used for this sample, relative to the typical LBG reduction strategy. First, we used a custom IDL script (N. Reddy 2010, private communication) to rectify the curved slitlets before performing any of the standard IRAF reduction tasks. Since the majority of our targets are LAEs with negligible continuum and a single emission line, we required slit rectification in order to extract a spectrum over a broad wavelength range at the location of the object indicated by the isolated bright  $Ly\alpha$  feature. Likewise, for deep-mask spectra, the faintness of the continuum level in the  $LyC$  region precluded a robust trace without rectification. We also followed the procedures outlined in Shapley et al. (2006) for background subtraction of deep-mask spectra. Accordingly, to avoid potential over-subtraction of the background, the object continuum location was excluded from the estimate of the background fit at each dispersion point. We used the maximum possible number of pixels to fit the sky emission for each object. In practice, the widths of the sky regions on either side of the continuum location depended on the length of each slitlet and the position of the object along the slit.

For LAEs, redshifts were calculated from the observed centroid of the  $Ly\alpha$  emission feature (rest-frame  $\lambda_{Ly\alpha} = 1215.67\text{\AA}$ ). For LBGs, emission redshifts were estimated from the observed centroid of  $Ly\alpha$ , and absorption redshifts from the centroids of interstellar metal absorption features when present.

Finally, as described in Siana et al. (in preparation), near-IR spectra of several objects in the sample were obtained in 2011 August with NIRSPEC (McLean et al. 1998) on Keck II. These data were collected for a separate project; we refer to these data here as, in three cases, the near-IR spectra reveal emission features relevant to the interpretation of the NB3640 detections (see Sections 4.1.2 and 4.1.3).

## 3. THE UPDATED LBG AND LAE SAMPLES

The Nestor et al. (2011) sample contained 26 LBGs with spectroscopic redshifts  $z \geq 3.055$ . Our new data include spectra of 11 LBGs and 1 QSO with previously determined redshifts, and 41 candidate LBG sources. For each of the 12 re-observed galaxies, the redshifts determined from our new data agree with the previous determinations within  $\Delta z = 0.012$ . The spectrum of one of the newly observed LBGs candidates reveals it to be a star. Of the 40 remaining galaxies, we were able to determine redshifts for 26 objects by identifying  $Ly\alpha$  emission and/or interstellar metal absorption features. All 26 galaxies have  $z > 2.45$ , 16 of which have  $z > 3.055$ . Thus, our updated sample of LBGs with redshifts  $z \geq 3.055$  contains 42 galaxies (26 previously known and 16 new). For this sample, the NB3640 filter probes the redshifted  $LyC$  spectral region. Coordinates, redshifts, and  $R$ -band photometry are listed in Table 1 for the 42  $z > 3.055$  sources, and in Table 2 for the 10  $z < 3.055$  newly confirmed LBGs.

Nestor et al. (2011) identified 110 LAE candidates having  $BV - \text{NB4980} \geq 0.7$  and  $\text{NB4980} \leq 26$ . Our new data include spectra of 96 of the 110 LAE candidates. Four of the LAEs for which we did not acquire new spectra are also LBGs with previously determined spectroscopic redshifts: C4, C28, M28 and MD23. The other 10 LAE candidates for which we did not acquire a spectrum are relatively faint in NB4980 ( $25.25 \lesssim \text{NB4980} \lesssim 26$ ) but are randomly distributed in  $BV - \text{NB4980}$  color. Thus, this incompleteness should not bias our results. We detect an emission line in the expected spectral region,  $\approx 4935\text{\AA} - 5015\text{\AA}$ , in the spectra of 88 of the candidates. One of the 88 is D3, which is also in our LBG sample with a previous spectroscopic redshift, and another two, C9 and M13, were LBG candidates that are now spectroscopically confirmed members of our LBG sample. Thus, there are seven objects that appear in both our LBG and LAE samples.

In principle, some of the emission lines detected in our spectra could be  $[\text{OII}]\lambda 3727$ , or in some cases  $\text{H}\beta$  or  $[\text{OIII}]\lambda 5007$ , from very faint lower-redshift systems. However, 76 of the 88 (86%) of the sources with a line detection have spectra with sufficient spectral coverage that, if the detected line was  $[\text{OII}]$ ,  $\text{H}\beta$ , or  $[\text{OIII}]$  at lower redshift, at least one of the other rest-frame optical features should have been detected as well. In no cases do we detect such corresponding lines. Furthermore, in a similar LAE survey at  $z = 3.1$  in the Extended Chandra Deep Field–South, Gronwall et al. (2007) argue that, given the relatively small volume covered by the narrow-band filter at  $z = 0.34$  relative to  $z = 3.1$  and the rarity of  $[\text{OII}]$  emitting galaxies with REW above their threshold ( $\text{REW} > 60\text{\AA}$  at  $z = 0.34$ ), their level of contamination by low- $z$   $[\text{OII}]$  emitters is negligible. As our filter is  $\sim 60\%$  broader than that used by Gronwall et al. (2007), we recognize a slight possibility of misidentification of a small number of emission lines. However, we continue with the assumption that all 88 of the lines that we determined to be  $\text{HI Ly}\alpha$  are correctly identified as such. One of these spectroscopically confirmed objects, LAE034, has  $z = 3.044$ . At this redshift some non-ionizing UV flux will contribute to the NB3640 detection, and therefore we excluded it from our sample.

Of the eight candidates for which we did not detect any emission line in the  $\approx 4975 \pm 40\text{\AA}$  spectral region, seven are relatively faint in NB4980, and the other is very diffuse in the  $\text{Ly}\alpha$  image with an extent significantly larger than the slit width. Thus, these objects may also be  $\text{Ly}\alpha$  emitting galaxies at  $z \geq 3.055$  that have insufficient line fluxes and/or sufficient slit losses such that the  $\text{Ly}\alpha$  emission line is not detectable in our data. In order to quantify the expected detection significance levels of  $\text{Ly}\alpha$  emission lines in our spectra, we predicted the  $\text{Ly}\alpha$  line fluxes for each LAE candidate using the measured  $BV$  and NB4980 magnitudes. We then measured the noise properties of the calibrated spectra in the wavelength interval corresponding to the width of the NB4980 filter in order to assess the minimum detectable line fluxes assuming unresolved lines. In practice, this method will underestimate the detection limit in some of our spectra, as we do not quantitatively account for slit losses or the possibility of resolved line profiles.

Figure 1 shows the predicted detection significance

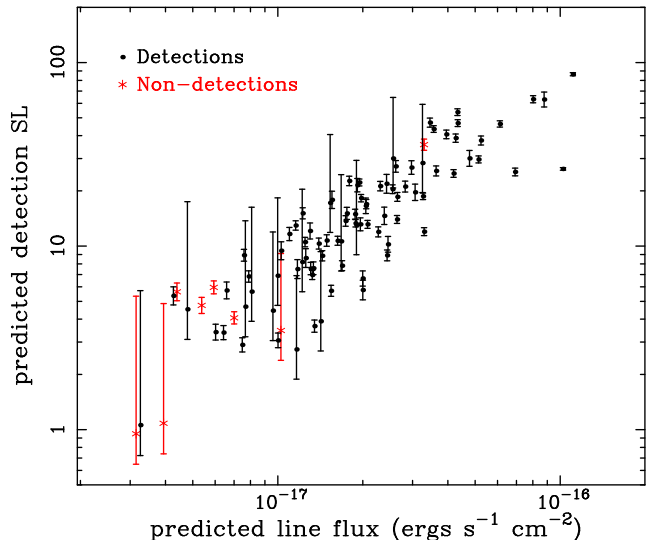


FIG. 1.— The predicted detection significance level ( $SL$ ) for emission lines in the spectra of our LAE candidates. The  $SL$  values are calculated using the photometrically-estimated line fluxes and the noise properties of the spectra. They do not account for slit losses or the possibility of resolved lines, and are thus upper limits. The predicted  $SL$  values for spectra with and without a detected emission line are represented by the black dots and red stars, respectively. Only one of our non-detections, LAE020, has a relatively high predicted  $SL$  value. LAE020 appears very diffuse in the  $\text{Ly}\alpha$  image, however, and thus its spectrum is expected to suffer from large slit losses.

level ( $SL$ ), i.e., the ratio of the photometrically-predicted line flux to the approximated line flux uncertainty, for each LAE candidate observed. For objects with multiple spectra having different resolutions, we show the smallest  $SL$  value if  $\text{Ly}\alpha$  is detected, and the largest  $SL$  value if it is not. We do not consider spectra in which the slit did not cover the position of the  $\text{Ly}\alpha$  flux, as is the case for some of the deep-mask spectra for which the slit was positioned over the offset NB3640 flux. All of the detections are consistent with having predicted  $SL > 3$ , with a median value of  $SL = 13$ . Seven of the eight objects without a detected emission line have, relative to those with detections, small upper-limits to their predicted detection significance,  $SL \lesssim 6$ , with a median value of  $SL = 4$ ; the other object is the diffuse system (LAE020) mentioned above. Thus, we can not rule the non-detections out as being  $z \approx 3.09$  LAEs. Additionally, considering the high success rate ( $\geq 91\%$ ) of our photometric selection at identifying  $z \geq 3.055$  LAEs, it is likely that most of the 10 candidates for which we have no spectroscopic data are also at  $z \geq 3.055$ . Nonetheless, we conservatively removed the 18 candidate LAEs without spectroscopic confirmation from the statistical sample discussed in this work, leaving a spectroscopic LAE sample of 91 galaxies spanning  $3.057 \leq z \leq 3.108$ . We summarize our photometric and spectroscopic results for the LAE sample in Table 3.

Nestor et al. (2011) also identified an additional 20 “faint sample” LAE candidates with  $26 < \text{NB4980} \leq 26.5$  and  $BV - \text{NB4980} \geq 1.2$ , corresponding to LAE IDs 111 – 130. We obtained spectra for 18 of these faint LAE candidates. We were unable to determine redshifts for two such systems (again, in data with low  $SL$  val-



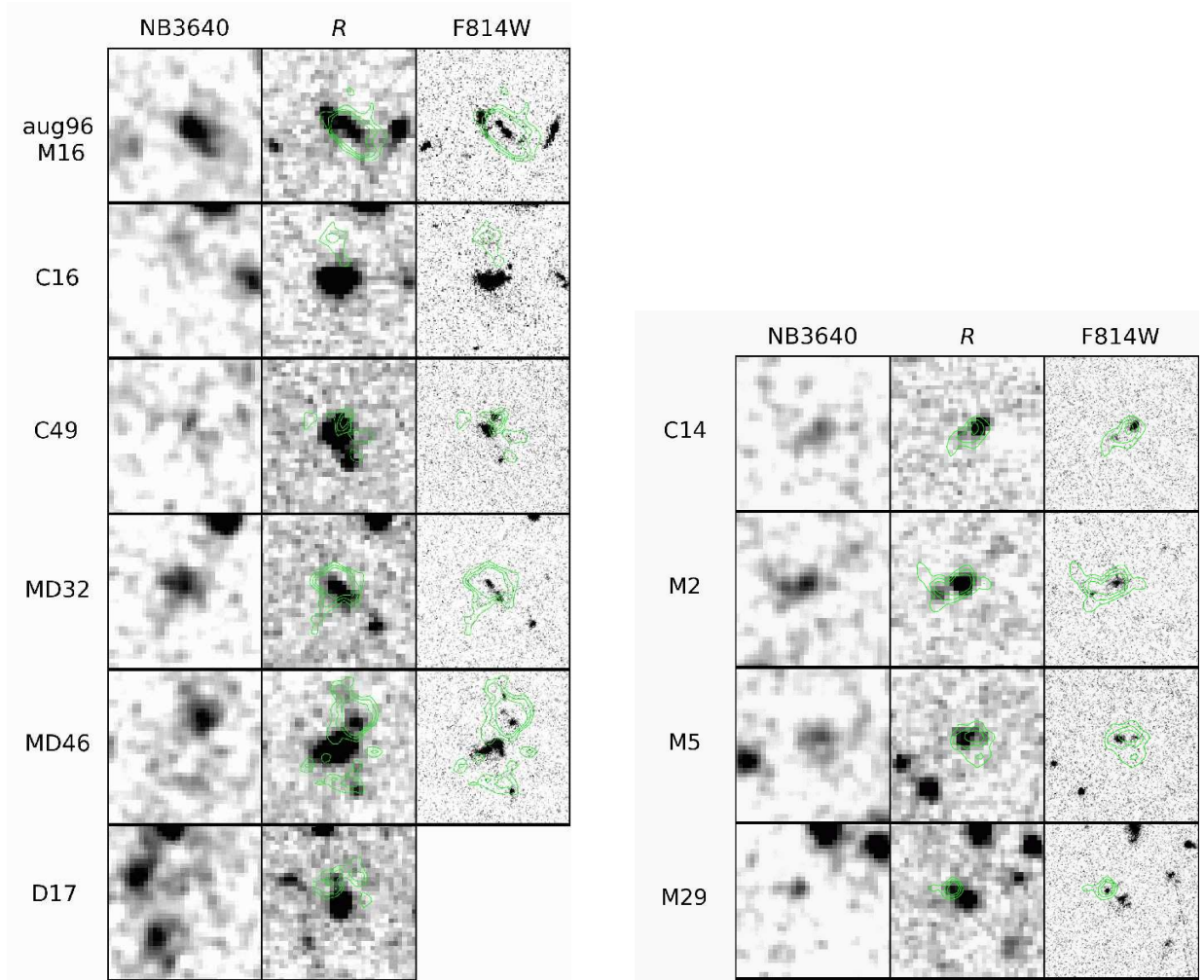


FIG. 2.— LBGs with  $z \geq 3.055$  detected in NB3640. Images are centered on the  $R$ -band centroid and span  $7'' \times 7''$ . The orientation is such that north is up and east is to the left. At these redshifts, the NB3640 filter (image shown here after smoothing by a Gaussian kernel with  $\text{FWHM}=0''.5$ ) samples the rest-frame LyC, while the  $R$  and F814W filters sample the rest-frame non-ionizing UV continuum. The green contours indicate NB3640 flux levels. Left: LBGs discussed in Nestor et al. (2011). Right: Newly confirmed  $z \geq 3.055$  LBGs.

ues). All of the other 16 systems were determined to have  $3.069 \leq z \leq 3.111$ . The faint sample LAEs have larger photometric uncertainties than the main sample LAEs and were selected with slightly different photometric criteria (Nestor et al. 2011). Thus, they are not included in the statistical analyses presented in this work. We include them in Table 3 for completeness.

#### 4. SYSTEMS WITH NB3640 DETECTIONS

With our updated spectroscopic sample of LBGs and LAEs in place, we now consider the set of objects with detections in our NB3640 image. Of the 26  $z \geq 3.055$  LBGs discussed in Nestor et al. (2011), six are detected in NB3640. Four of our 16 newly confirmed high-redshift LBGs are also detected in NB3640: C14, M2, M5, and M29. Their NB3640-,  $R$ -, and  $HST$  F814W images are shown in Figure 2, with the contours corresponding to 28.81, 28.06 and 27.62 mag arcsec $^{-2}$  in the NB3640 image. All four of the newly confirmed LBGs with NB3640 detections appear clumpy in the  $HST/ACS$  images, with multiple discrete regions of non-ionizing continuum. The NB3640 flux appears to cover all of the clumps in C14, M2 and M5. In M29, the NB3640 flux appears to be

associated with only the more compact clump, which is  $\simeq 0''.75$  to the northeast of a more extended region of non-ionizing UV flux. With the addition of these four new NB3640 detections, we now have 10 NB3640 detections associated with 42  $z \geq 3.055$  LBGs. Their NB3640 magnitudes, the spatial offset between the  $R$ -band and NB3640 flux centroids, and the inferred non-ionizing to ionizing UV flux-density ratios are presented in Table 1.

In our sample of 91 spectroscopically confirmed LAEs, 20 have NB3640 detections. An additional 6 LAE candidates from Nestor et al. (2011) have NB3640 detections: one was not targeted in our spectroscopy, and we were unable to confirm the redshifts of five other candidates. Thus, these six objects are not discussed here. For the 20 LAEs with associated NB3640 detections, we report in Table 3 the NB3640 magnitudes, spatial offsets between both  $R$ -band and LyA and NB3640 flux centroids, and the inferred non-ionizing to ionizing UV flux-density ratios.

Below, we discuss in detail the combined spectroscopic and imaging data sets for the individual objects in our updated samples that were considered LyC detections

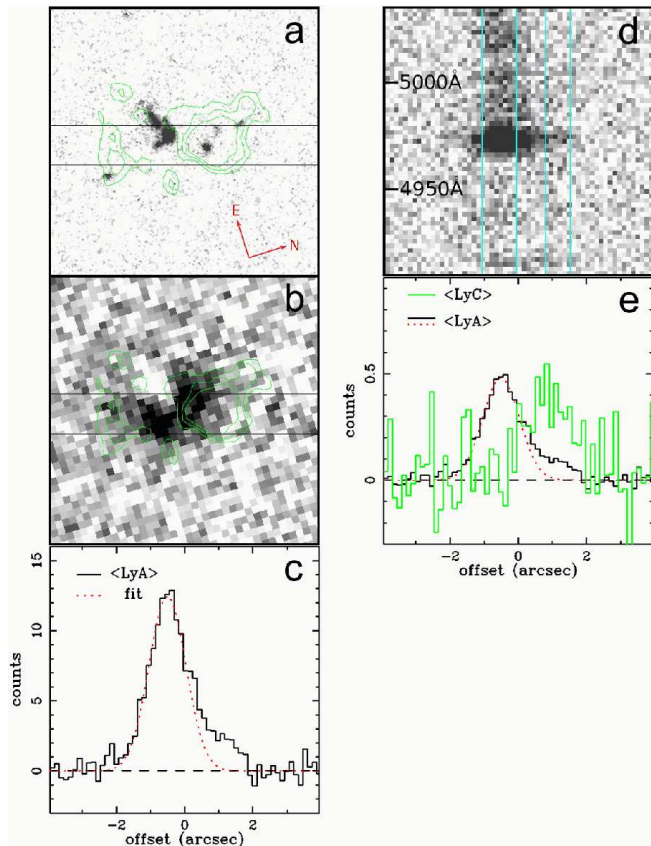


FIG. 3.— The emission structure of MD46. Left: The spatial extent of  $\text{Ly}\alpha$  emission compared to the rest-frame non-ionizing UV continuum emission and putative  $\text{LyC}$  radiation (green contours). Panel (a) shows the *HST*/ACS-F814W image (spatial resolution  $\simeq 0''.1$ ) while panel (b) is our “ $\text{LyA}$ ” (seeing  $\simeq 0''.8$ ) image. The slit position for our deep-mask spectrum is indicated in both images. Panel (c) displays the spatial (i.e., along the slit) extent of the  $\text{Ly}\alpha$  line, averaged over (rest-frame)  $\approx 4\text{\AA}$  of our deep-mask spectrum and registered to the images. The dotted curve is a Gaussian fit to the profile, excluding the excess at positive offset. Right: The relative spatial extents of  $\text{LyC}$  and  $\text{Ly}\alpha$  emission. Panel (d) shows the two-dimensional spectrum in the redshifted  $\text{Ly}\alpha$  region. The two extraction apertures applied in Figure 4 are indicated with cyan boxes. In panel (e), we show the profile for the region of the two-dimensional spectrum averaged in the spectral direction from rest-frame  $\lambda \simeq 875\text{\AA}$  to  $\lambda \simeq 910\text{\AA}$  (green), as well as that of the  $\text{Ly}\alpha$  region, re-scaled for ease of comparison (black).

in Nestor et al. (2011), as well as the newly determined  $z > 3.055$  LBGs. The data are shown in Figures 3–15. *HST*/ACS-F814W images are shown when available, *BV* images are shown otherwise, and all of the images span  $8''$  per side. Slit positions are indicated by blue (deep mask) and/or black (shallow mask) boxes. Green contours represent NB3640 flux levels (see above). The LAE images also contain red contours, representing  $\text{LyA}$  (see Section 2.1) flux levels.<sup>3</sup> Two-dimensional spectra, when shown, are registered in the spatial direction to match the accompanying imaging and span  $\simeq 125\text{\AA}$  in the spectral direction. Unless otherwise noted, one-

<sup>3</sup> Due to the large range of  $\text{LyA}$  fluxes in our LAE sample, the flux levels represented by the red contours vary from image to image.

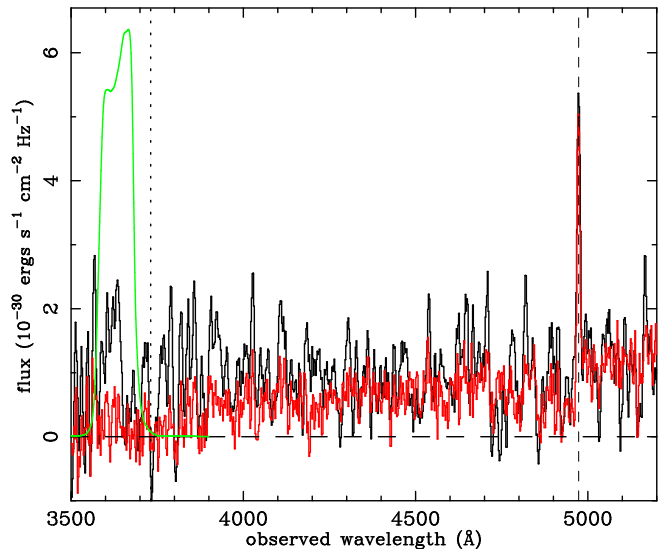


FIG. 4.— The extracted deep-mask spectra of MD46. We identify the emission feature at  $\lambda = 4973\text{\AA}$  as  $\text{Ly}\alpha$  at redshift  $z = 3.091$  (vertical dashed line). The corresponding Lyman break is marked with a vertical dotted line. The black spectrum, which has been boxcar smoothed (5 pixels), is the extraction containing only the northwestern clump (see Figure 3), which is spatially consistent with the detected NB3640 flux. The red spectrum represents the extraction that excludes the northwestern clump. The red spectrum has been scaled such that the average flux levels redward of  $\text{Ly}\alpha$  are approximately equal. Also shown in green, below the Lyman limit, is the NB3640 filter transmission curve.

dimensional spectra are shown without smoothing or binning. When multiple one-dimensional spectra are shown, the additional spectra are offset for clarity and the non-offset spectrum corresponds to the horizontal slit in the imaging (by default, the deep-mask slit when available).

#### 4.1. LBGs

In this section, we discuss the individual LBGs having NB3640 detections for which we have new data. We begin with the four systems which we retain as possible  $\text{LyC}$ -leaking galaxies. We next discuss the three LBGs for which we find evidence for the presence of a foreground interloper in our new data. We then discuss the special case of aug96M16, and conclude the section with a summary of our LBG NB3640 detection sample.

##### 4.1.1. LBG Lyman-continuum Candidates

###### MD46

The LBG MD46 ( $z = 3.091$ ) has a complex multi-component morphology, which can be clearly seen in Figure 3. Panel (a) shows the *HST*/ACS-F814W image, in which the flux appears to originate from at least three distinct clumps. Panel (b) shows the ground-based  $\text{LyA}$  image. The clump to the east, which partly enters the slit, is spatially coincident with negative flux in the  $\text{LyA}$  image (corresponding to  $\text{Ly}\alpha$  absorption at  $z \simeq 3.09$ ). The bulk of the  $\text{Ly}\alpha$  emission appears to emanate from in and around the central clump, while the bulk of the NB3640 flux avoids this central clump and is instead spatially coincident with the clump  $\simeq 1''.1$  to the northwest, which also falls on the slit. Thus, it is important to determine if the northwestern clump is also at  $z \simeq 3.09$ .

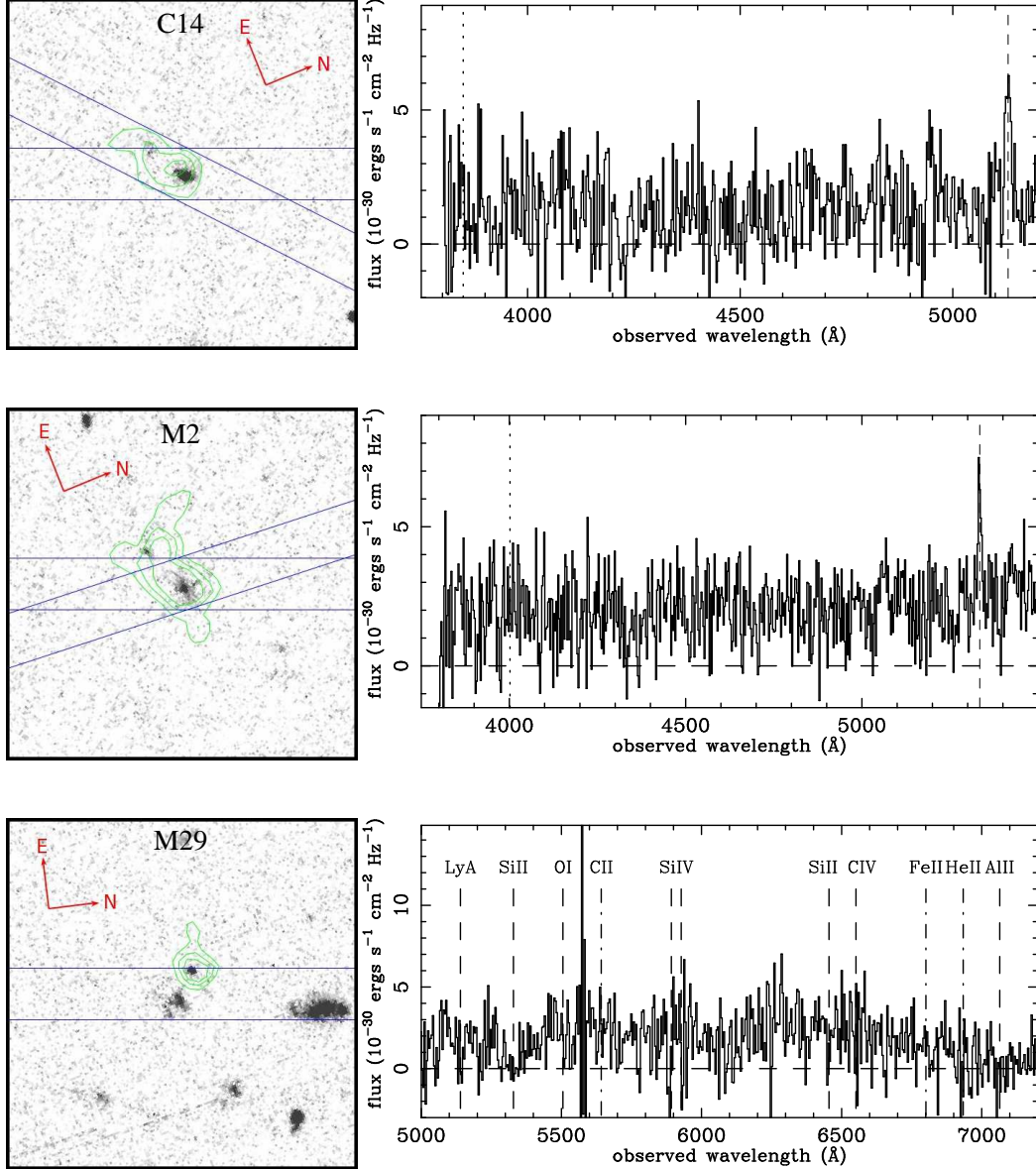


FIG. 5.— *HST*/ACS F814W images ( $8''$  per side) and spectra of LBGs with NB3640 detections retained as possible LyC emitters. The positions and sizes of the slits are indicated with boxes, and green contours indicate NB3640 flux levels. When present, vertical dashed and dotted lines in the spectra indicate the position of the redshifted Ly $\alpha$  line and Lyman break, respectively. Top: Image and shallow-mask spectrum C14. The other shallow-mask spectrum of C14 (corresponding to the diagonal slit) has a very low signal to noise ratio and is not shown. Middle: The F814W image and combined shallow-mask spectrum of M2. Bottom: Image and shallow-mask spectrum of M29. The locations of several common interstellar absorption features are marked with vertical dashed (detected) and dash-dotted (non-detected) lines.

The region of the two-dimensional spectrum corresponding to redshifted Ly $\alpha$  emission is shown in panel (d). The Ly $\alpha$  emission line appears asymmetric, which can be seen more clearly in panel (c), where we have averaged over  $\approx 4 \text{\AA}$  (rest-frame) in the spectral direction, centered on the peak of the Ly $\alpha$  emission line, and fitted a Gaussian profile (dotted curve) constrained only by the data south of the spatial zero-point indicated by the figure axis. This fit highlights the asymmetric northwestern extension, which is spatially coincident with the northwestern clump seen in the *HST* imaging and the NB3640 flux in our Keck imaging. The spatial coincidence of the Ly $\alpha$  and NB3640 emitting region implies that the northwestern clump is also very likely to be emitting Ly $\alpha$  at

$z \simeq 3.091$ , which in turn indicates that the NB3640 flux is indeed escaping LyC emission.

Panel (e) shows the spatial profile for the region of the two-dimensional spectrum just below the redshifted Lyman-limit (green histogram), averaged in the spectral direction over  $\lambda \simeq 880 \text{\AA} - 910 \text{\AA}$  in the rest-frame, as well as that of the Ly $\alpha$  region (black histogram, re-scaled by factor of 26 for ease of comparison). Again, the NB3640 flux is spatially aligned with the extended Ly $\alpha$ , suggesting that it is actually LyC flux escaping from a galaxy at  $z = 3.09$ . We extracted one-dimensional spectra in two locations in the two-dimensional spectrum. The extraction apertures are shown in panel (d). Figure 4 displays the resulting one-dimensional spectra. The black spec-



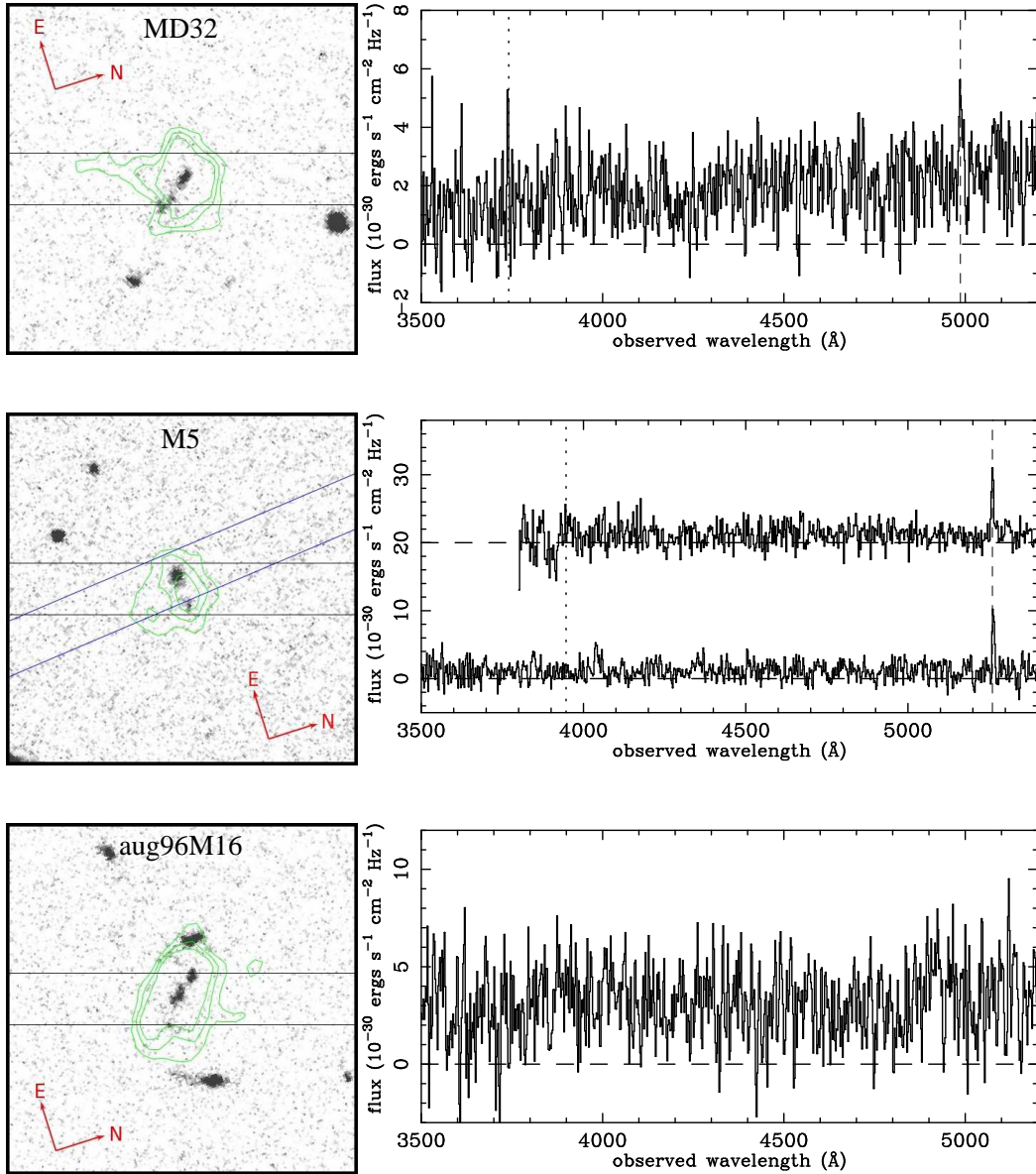


FIG. 6.— As in Figure 5, but for systems with evidence of contamination (top and middle) or with unconfirmed redshift (bottom). Top: Image and deep-mask spectrum of MD32. Middle: Image and shallow- (offset, upper) and deep-mask (lower) spectra of M5. Bottom: Image of aug96M16 and the deep-mask spectrum. We were unable to determine the redshift of the region most closely associated with the NB3640 emission.

trum, which has been smoothed with a 5-pixel boxcar, represents the northwestern extraction corresponding to the extended  $\text{Ly}\alpha$  emission and the detected NB3640 flux. The red spectrum, which has been scaled down by a factor of 5.6 such that the average flux level redward of  $\text{Ly}\alpha$  emission is equal to that of the black spectrum, represents the southern extraction, corresponding to the central clump, which is undetected in our NB3640 imaging. The spectrum of the central clump appears to exhibit a strong break at the Lyman limit, the position of which is indicated by the vertical dashed line. In contrast, the northwestern clump appears to lack a sharp break at the Lyman limit. We also note that several  $\text{Ly}\alpha$  forest absorption lines appear to be present in both spectra (e.g., at  $\lambda \simeq 4720\text{\AA}$ ,  $4860\text{\AA}$ ,  $4925\text{\AA}$ , etc.) suggestive of the continua originating at similar emission redshifts. However, the poor signal to noise ratios prevent quanti-

tative analysis of any perceived correlation.

We conclude that the  $z = 3.091$  LBG MD46 contains three distinct (rest-frame) UV-bright regions. The southeastern region is a  $\text{Ly}\alpha$  absorber as seen from our viewing perspective, while the central and northwestern regions exhibit  $\text{Ly}\alpha$  in emission. Of these latter regions, the fainter region (in both continuum and line emission) is more compact and can be seen in ionizing continuum along our sightline. Thus we retain MD46 in our  $\text{LyC}$ -emitting LBG sample.

#### C14

We obtained spectra of the LBG candidate C14 on two of the shallow masks. Each spectrum exhibits an emission line at  $\lambda \simeq 5130\text{\AA}$ , which we attribute to  $\text{Ly}\alpha$  at  $z = 3.220$ . C14 is detected in our NB3640 image (Figure 2). In the *HST*/ACS image, shown in the top panel



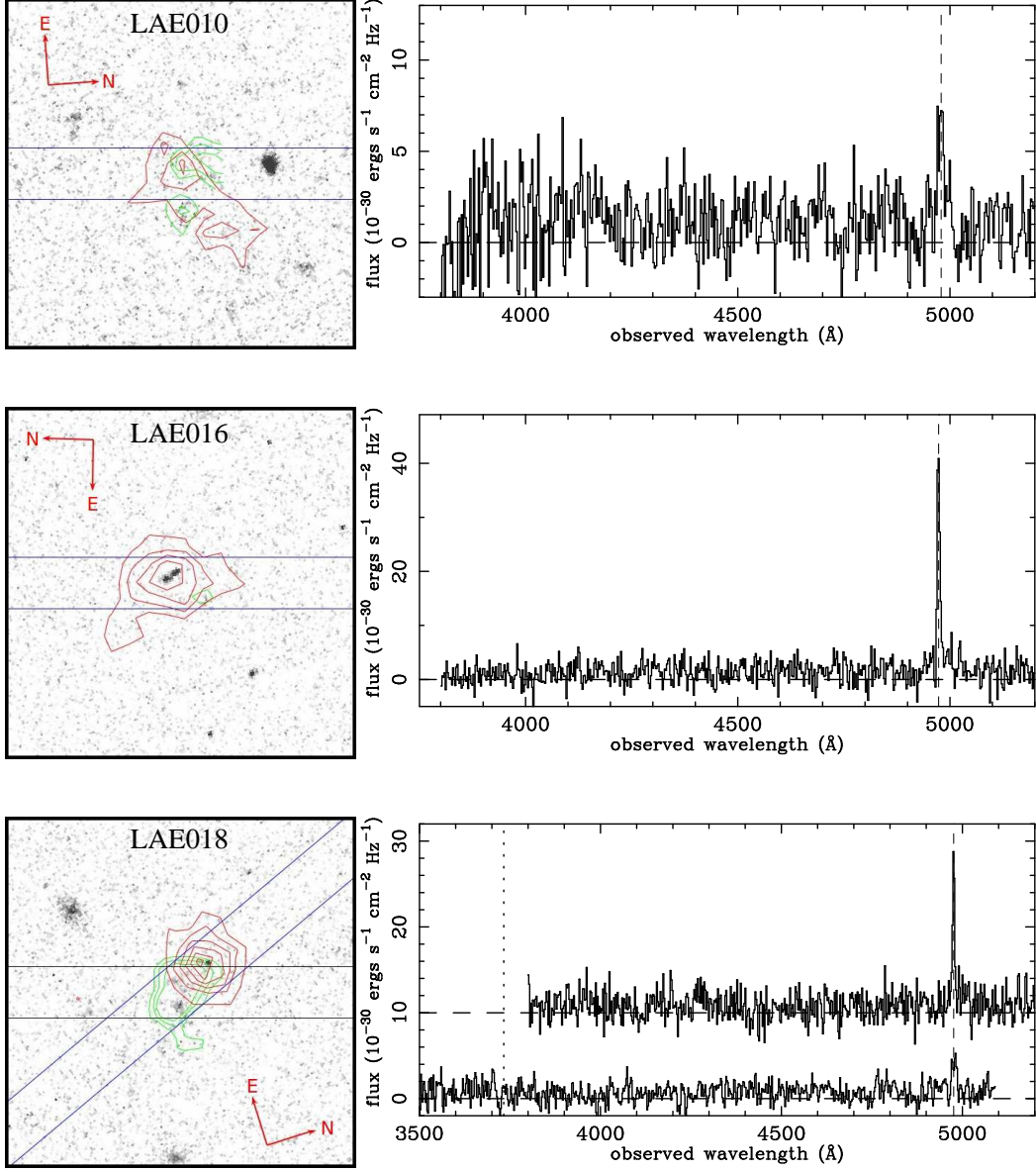


FIG. 7.— The emission structures of (from top down) LAE010, LAE016, and LAE018. The left panels show the *HST*/ACS-F814W images. The boxes indicate the positions of all shallow- (blue) and deep- (black) mask slits. Green and red contours represent flux levels in the NB3640 and *LyA* images, respectively. The right panels display the one-dimensional extracted spectra. The vertical dashed/dotted lines indicate the position of the redshifted  $\text{Ly}\alpha$ /Lyman limits, respectively. For LAE018, we show both the shallow- (offset, upper) and deep-mask (lower) spectra.

of Figure 5, C14 breaks into a brighter and a fainter clump, with the NB3640 emission appearing to span the two clumps. As no other emission features were robustly detected in either spectrum, we retain C14 as a possible LyC-emitting galaxy. We note, however, that the spectrum corresponding to the slit position that is better aligned with both clumps (not shown) is of relatively poor quality, and therefore our limits on the absence of other emission features from the fainter clump are relatively weak.

### M2

We obtained spectra of the LBG candidate M2 on two of the shallow masks. Both spectra exhibit an emission line at  $\lambda \simeq 5334\text{\AA}$ , which we attribute to  $\text{Ly}\alpha$  at  $z = 3.388$ . M2 is detected in our NB3640 image (Fig-

ure 2). In the *HST*/ACS image, shown in the middle panel of Figure 5, M2 breaks into a brighter and a fainter clump, with the NB3640 emission appearing to span the two clumps. No other emission features were robustly detected in either spectrum. Thus, we retain M2 as a possible LyC-emitting galaxy.

### M29

We obtained a spectrum of the LBG candidate M29 on one of the shallow masks. The spectrum does not exhibit emission lines. However, we identify interstellar absorption lines from OI, SiIV, SiII, and CIV corresponding to a redshift of  $z = 3.228$ . M29 is detected in our NB3640 image (Figure 2). Two clumps of emission are seen in the *HST*/ACS image, shown in the bottom panel of Figure 5. The NB3640 emission only covers the

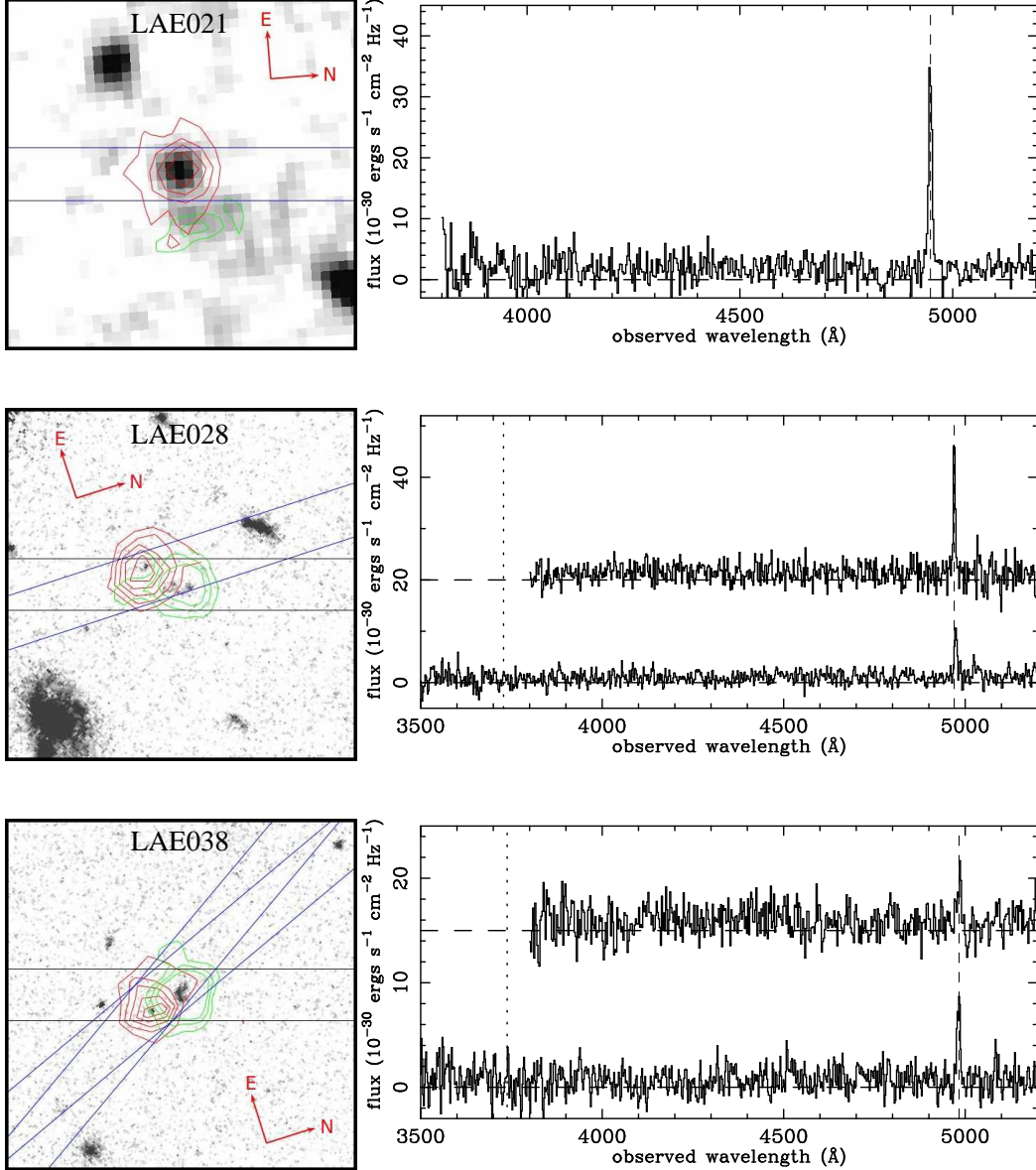


FIG. 8.— Same as Figure 7, but for LAE021, LAE028, and LAE038. Our BV image is shown for LAE021 as it does not have *HST*/ACS-F814W imaging. For LAE028 and LAE038, we show both the shallow- (offset, upper) and deep-mask (lower) spectra.

more compact clump. It is possible that both clumps are at  $z = 3.228$ , with the NB3640 emission emanating from a compact star-forming clump. Alternatively, the more diffuse source may be at high redshift while the compact source associated with the NB3640 emission is in the foreground. Lacking any direct evidence to favor either scenario, we retain M29 as a possible LyC-emitting galaxy and account for the possibility of contamination with our Monte Carlo simulation (Section 5).

#### 4.1.2. LBGs With Evidence For Contamination

##### MD32

The *HST*/ACS image and our deep-mask spectrum of MD32 ( $z = 3.102$ ) are shown in the top panel of Figure 6. Our spectrum exhibits flux below the redshifted Lyman limit, and contains no evidence for foreground contaminants. However, in the NIRSPEC observations

the slit was aligned along the direction of elongation of MD32. The resulting two-dimensional spectrum exhibits an additional line within  $\sim 0''.7$  of MD32 which, if [OIII]  $\lambda 5007$ , would correspond to a redshift of  $z = 2.88$ . Due to this evidence of contamination, we remove MD32 from our list of possible LyC-emitting galaxies.

##### M5

We obtained spectra of the LBG candidate M5 with both the deep mask and one of the shallow masks. Each spectrum exhibits an emission line at  $\lambda \simeq 5260 \text{ \AA}$ , which we attribute to Ly $\alpha$  at  $z = 3.327$ . M5 is detected in our NB3640 image (Figure 2). Two clumps of emission are observed in the *HST*/ACS image, shown in the middle panel of Figure 6. The NB3640 emission appears to span the two clumps. However, our deep-mask spectrum of M5, also shown in Figure 6 along with the shallow-mask spectrum, reveals the presence of an additional, bluer,

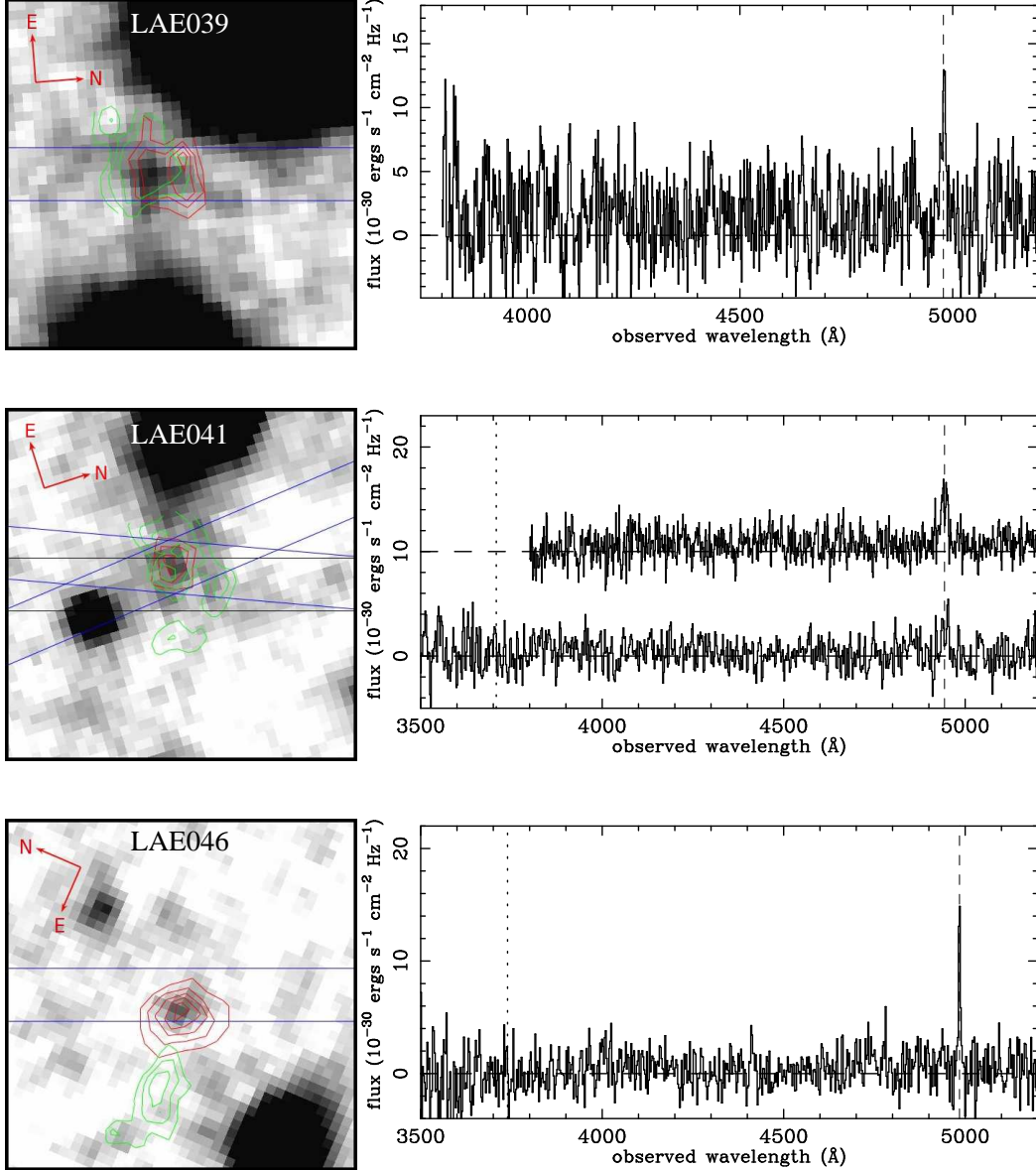


FIG. 9.— Same as Figure 7, but for LAE039, LAE041, and LAE046. BV images are shown as LAE039, LAE041 and LAE046 do not have *HST*/ACS-F814W imaging. For LAE041, we show both the shallow- (offset, upper) and deep-mask (lower) spectra.

emission line at  $\lambda \simeq 4040\text{\AA}$ , indicating the presence of a lower-redshift interloper. It is noteworthy, however, that the detected NB3640 flux covers both clumps of continuum emission. Thus, if the interloper is associated with only one of the clumps, it may be that M5 is indeed being detected in LyC emission. Nonetheless, we conservatively remove M5 from our list of possible LyC detections.

#### C49

Although we did not obtain a new LRIS spectrum of C49 ( $z = 3.163$ ), it was observed with NIRSPEC. As shown in Figure 2, the *HST*/ACS image reveals that C49 comprises two distinct clumps. The NIRSPEC slit was positioned to capture the spectra of both of these clumps. While the spectrum of the southern clump confirms the redshift  $z = 3.16$ , that of the northern clump, which is spatially closer to the NB3640 detection, has an

additional emission line which, if [OIII]  $\lambda 5007$ , would correspond to a redshift of  $z = 2.97$ . We therefore remove C49 from our list of possible LyC-emitting galaxies.

#### 4.1.3. Unconfirmed LBG redshift

##### aug96M16

The *HST*/ACS image of aug96M16 is shown in the bottom panel of Figure 6. As with MD46, the *HST* imaging reveals the emission from aug96M16 to comprise several distinct clumps. The detected NB3640 flux is coincident with the central region of emission that spans the  $1''.2$  width of our LRIS slit. Only the western-most clump ( $\approx 1''.3$  west of the slit edge) was resolved as a distinct clump, separate from LBG candidate aug96M16, in the ground-based data originally used to select LBG candidates based on  $U - G$  and  $G - R$  colors in the SSA22a field (Steidel et al. 2003). This western-most clump has

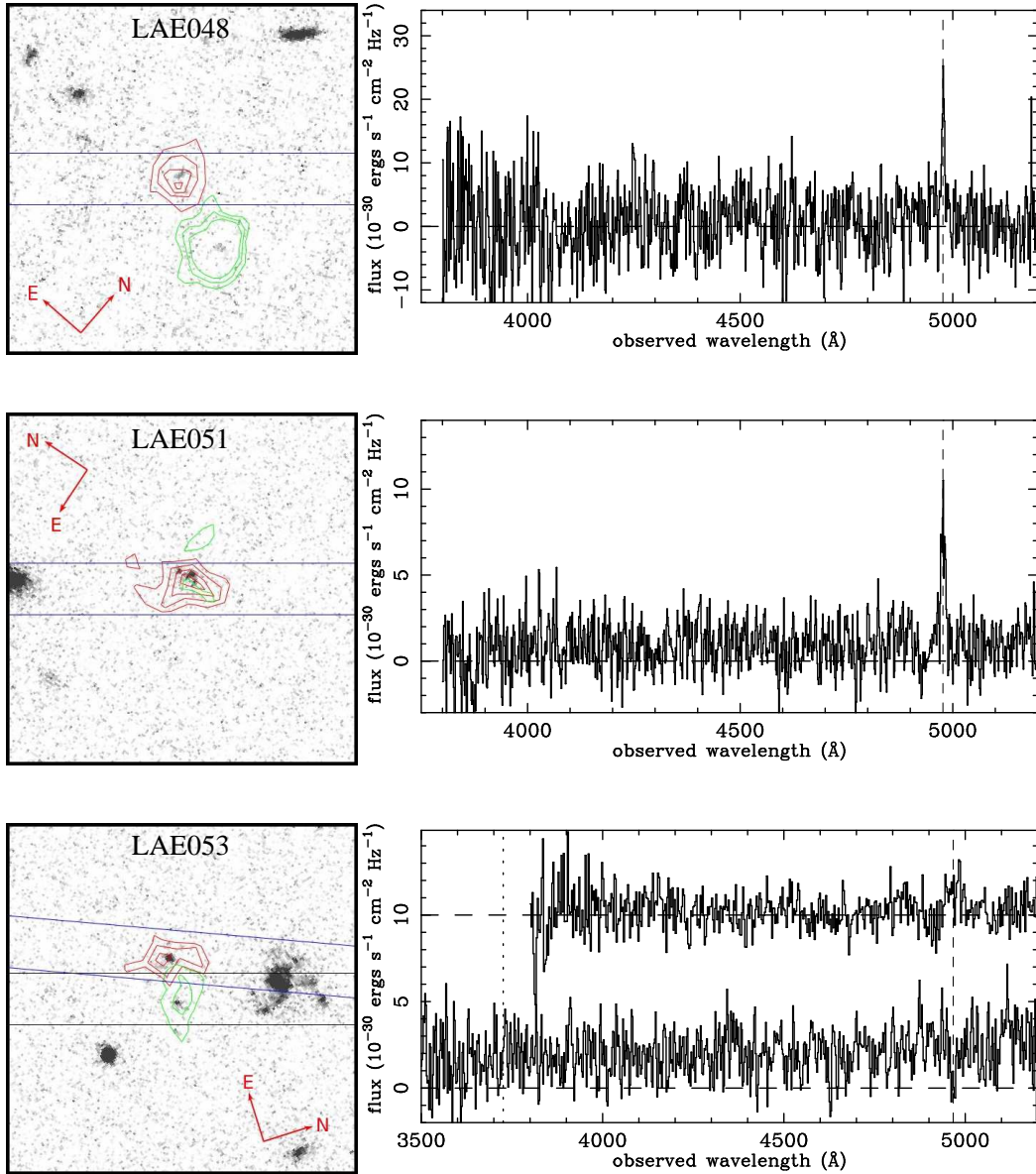


FIG. 10.— Same as Figure 7, but for LAE048, LAE051, and LAE053. For LAE053, we show both the shallow- (offset, upper) and deep-mask (lower) spectra.  $\text{Ly}\alpha$  appears in absorption in the deep-mask spectrum of LAE053, as the slit was centered on the NB3640 detection which is offset by  $\approx 0''.9$  from the  $\text{Ly}\alpha$  emission.

a previously determined spectroscopic redshift  $z = 3.285$ , which was also (erroneously) attributed to aug96M16 in Nestor et al. (2011). The slit position in our LRIS deep mask covered neither the western-most nor eastern-most clump ( $\approx 0''.75$  east of the slit edge). The slit position of our NIRSPEC spectrum (Siana et al., in preparation; see Section 2.2) of aug96M16 was aligned to cover all of the emission clumps, however. Using the NIRSPEC data, we determine a redshift  $z = 3.09$  for the eastern-most clump and confirm the redshift of the western-most clump as  $z = 3.29$ . The large difference in redshift between the eastern-most and western-most clumps indicates that, although both are at  $z > 3.055$ , they are physically unrelated. Our deep-mask spectrum of the central clumpy region, which is coincident with the NB3640 detection, is also shown in Figure 6. We are unable to determine a redshift for this region from either our deep mask or NIRSPEC spectra. Therefore, although it was photo-

metrically selected as an LBG candidate and is within  $\sim 1''$  on the sky to a spectroscopically-confirmed galaxy at  $z = 3.09$ , we conservatively remove aug96M16 from our list of possible LyC-emitting galaxies as well as from the parent  $z \geq 3.055$  LBG sample.

#### 4.1.4. Summary of LBGs

As discussed above, our sample began with 10 LBGs with possible LyC detections. Our new data includes spectra of seven of these 10 objects. In these spectroscopic data we find evidence for the presence of a foreground object in close proximity on the sky to three of these LBGs – MD32, C49, and M5 – and are unable to confirm the redshift of the source associated with the NB3640 flux in a fourth – aug96M16. Of the seven LBGs having NB3640 detections with new spectroscopic data, we retain as possible LyC emission NB3640 detections in four: MD46, C14, M2, and M29, as well as two detections



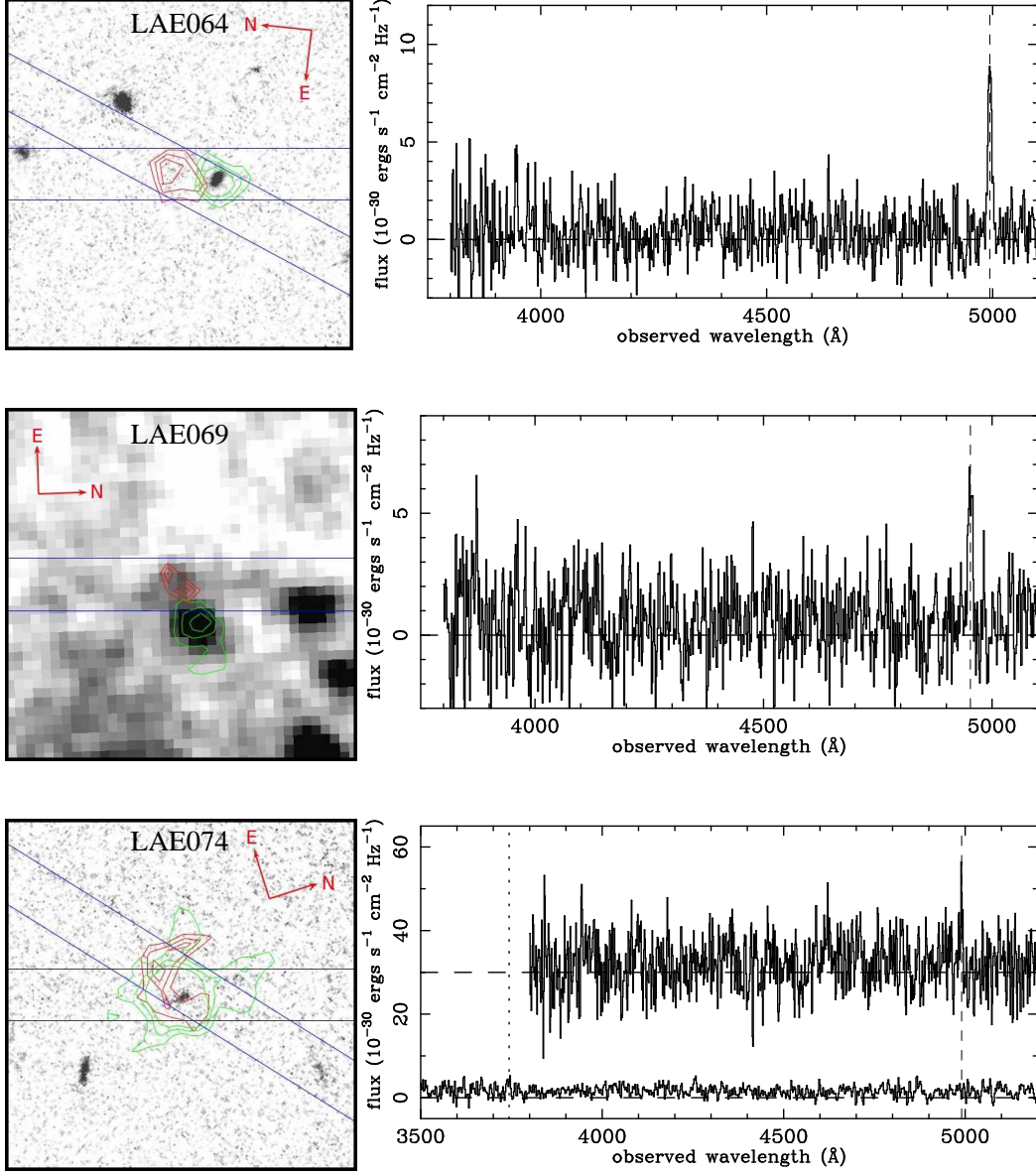


FIG. 11.— Same as Figure 7, but for LAE064, LAE069, and LAE074. Our BV image is shown for LAE069 as it does not have *HST*/ACS-F814W imaging. For LAE074, we show both the shallow- (offset, upper) and deep-mask (lower) spectra. Ly $\alpha$  emission is not detected in the deep-mask spectrum. As the slit was centered on the NB3640 detection the bulk of the Ly $\alpha$  emission fell outside of the slit.

for which we do not have new data: D17 and C16. Thus, our LBG sample now contains a total of six putative LyC-leaking galaxies from a parent sample of 41 LBGs (i.e., excluding aug96M16; see Section 4.1.3). Notably, we are able to study the spatial distribution of the Ly $\alpha$  and NB3640 emission in detail for MD46, and find compelling evidence that the NB3640 emission is escaping LyC flux.

It is possible that some of the 32 LBGs with no NB3640 detections have levels of escaping LyC flux that are below our detection limit of  $m_{\text{NB3640}} \sim 27.3$ . To investigate this possibility, we stacked cut outs of the NB3640 image centered on the locations of these 32 LBGs. We detect no flux in the stacked image down to a  $3\sigma$  limit on the average magnitude of  $m_{\text{NB3640}} = 27.96$ .

#### 4.2. LAEs

As above, in this section we discuss the individual LAEs with NB3640 detections. We begin with an overview of the 17 systems which we retain as possible LyC-leaking galaxies. We next discuss the three LAEs for which we find evidence for the presence of a foreground interloper. We then discuss the six LAEs with NB3640 detections for which we were unable to confirm redshifts and are thus not included in our sample, and conclude the section with a summary of our LAE NB3640 detections.

##### 4.2.1. LAE Lyman-continuum Candidates

As indicated in Table 3, we spectroscopically confirm redshifts of  $3.070 \leq z \leq 3.108$  with no evidence for contamination for 17 LAEs with NB3640 detections. The images and spectra for these LAEs are shown in Figures 7 – 12. We briefly discuss each individual field in

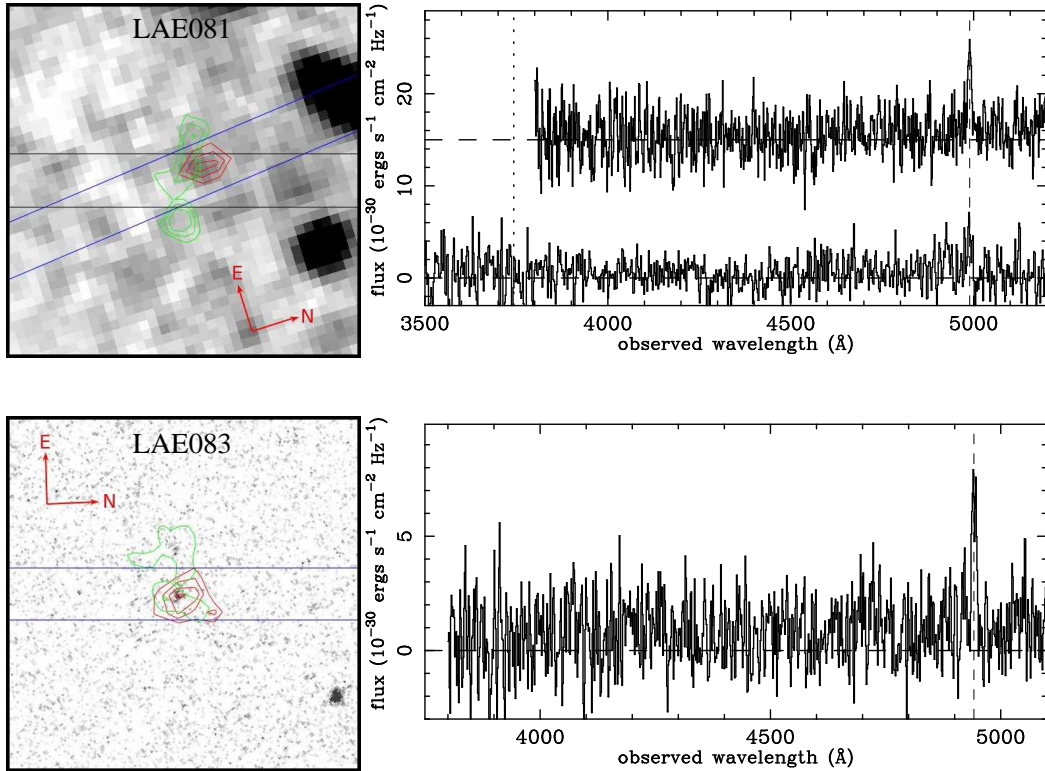


FIG. 12.— Same as Figure 7, but for LAE081 and LAE083. For LAE081, we show both the shallow- (offset, upper) and deep-mask (lower) spectra and BV image as it does not have *HST*/ACS-F814W imaging.

the appendix. Of particular note is LAE053, for which the *LyA* and NB3640 emission are offset by  $\simeq 0''.9$ . The F814W image reveals that each of the *LyA* and NB3640 detections is coincident with one of two distinct emission clumps. Our shallow- and deep-mask slits cover only the clump associated with the *LyA* and NB3640 fluxes, respectively. In the shallow-mask spectrum, we detect *LyA* in emission at  $z = 3.090$ . In the deep-mask spectrum, however, we detect an absorption feature at the same wavelength as the emission line in the shallow-mask spectrum. We interpret this feature as *LyA* absorption at  $z = 3.090$ , which is compelling evidence that the clump associated with the NB3640 emission is also at  $z = 3.090$  and, in turn, that the NB3640 flux is indeed LyC emission. In contrast, however, we caution that for four of the candidates shown in Figures 7–12 (LAE021, LAE046, LAE048 and LAE069), the position of the NB3640 flux was not covered by any of the slit spectra. Thus we are unable to search directly for evidence of foreground contamination being responsible for the detected NB3640 flux. Additionally, the F814W images of LAE046 (Figure 9) and LAE048 (Figure 10) reveal that the NB3640 and *LyA* fluxes, respectively, are coincident with sources of non-ionizing continuum that are significantly ( $\gtrsim 1''.5$ ) spatially offset from each other, suggesting the sources are unrelated. In the absence of direct spectroscopic evidence confirming contamination for these individual systems, we ran a Monte Carlo simulation (described in Section 5) to statistically address the possibility of contamination in the entire sample of 17 detections. In this simulation, NB3640 detections with large offsets are likely to be rejected as foreground interlopers. Thus, while individually the conclusions that LAEs such as LAE046 and

LAE048 are LyC-leaking galaxies should be taken with caution, our statistical results are robust to the possibility of foreground contamination.

#### 4.2.2. LAEs With Evidence For Contamination

We find evidence for the presence of a foreground galaxy in the spectra of three of our LAEs, which we present below. Additionally, one of the LAE candidates from Nestor et al. (2011), LAE034, is at a low enough redshift that it experiences contamination of its NB3640 flux from non-ionizing UV radiation. We have thus removed LAE034 from our list of possible LyC-emitting galaxies as well as from the parent  $z \geq 3.055$  LAE sample.

##### LAE003

LAE003 has the brightest NB3640 detection ( $m_{\text{NB3640}} = 24.74$ ) of any of our LBGs or LAEs in Nestor et al. (2011). The top-left panel of Figure 13 shows the F814W image indicating the relative positions of the non-ionizing UV flux, the deep and shallow-mask slits, the *LyA* flux and the NB3640 flux. The middle panel shows the region of the two-dimensional spectrum corresponding to the expected location of the redshifted *LyA* line. We identify the line detected at  $\lambda = 4980$  as *LyA*, indicating that LAE003 is at  $z = 3.097$ .

However, as can be seen in the lower panel, which shows a bluer region of the two-dimensional spectrum, there is another emission line spatially consistent with the LAE. If this line is also *LyA* emission, it corresponds to a redshift of  $z = 1.763$ . The bluer line is very slightly offset to the south, consistent with the tail-like structure seen in the *HST*/ACS image. It is therefore possible that the  $z = 3.097$  LAE003 is opaque below the Lyman limit

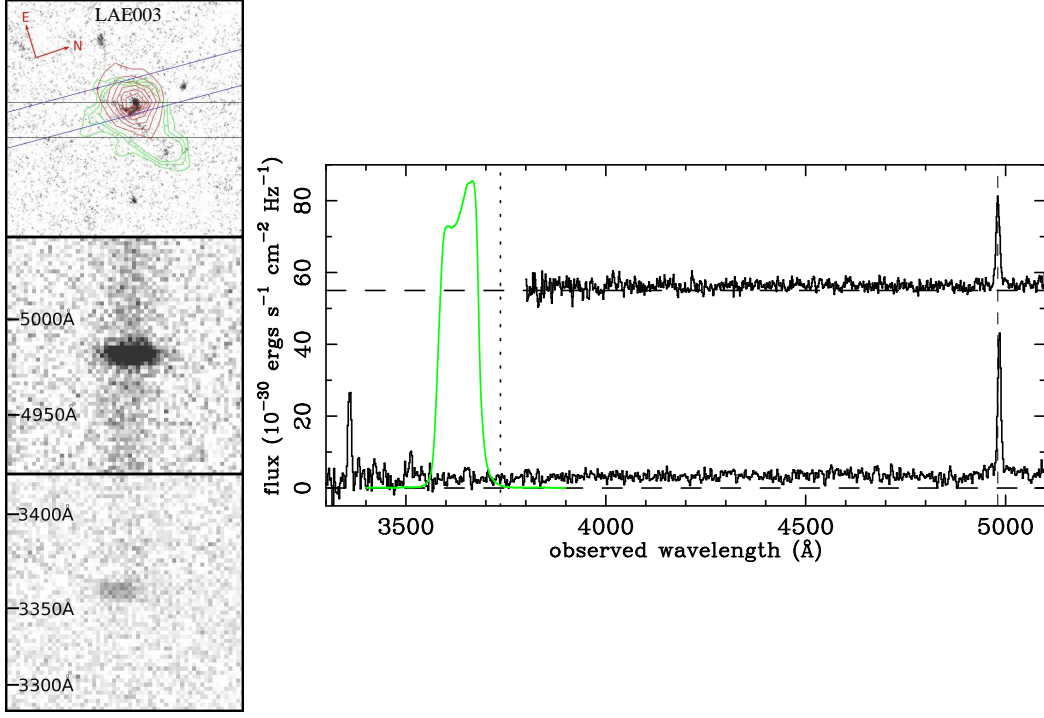


FIG. 13.— The emission features of LAE003. Left: The top panel shows the *HST*/ACS-F814W image. The middle panel shows the two-dimensional spectrum in the redshifted Ly $\alpha$  region, while the bottom panel shows a redder region of the spectrum, centered at the wavelength (3359Å) of a bluer emission line. Right: The extracted one-dimensional spectra of LAE003. Shown are both the shallow- (offset, upper) and deep-mask (lower) spectra. We identify the emission feature at  $\lambda = 4984$  Å as Ly $\alpha$  at redshift  $z = 3.097$ . The corresponding Lyman break is marked with a vertical dotted line. The bluer emission line is clearly detected at  $\lambda = 3359$  Å in the deep-mask spectrum. The green curve below the Lyman limit indicates the shape of the NB3640 filter.

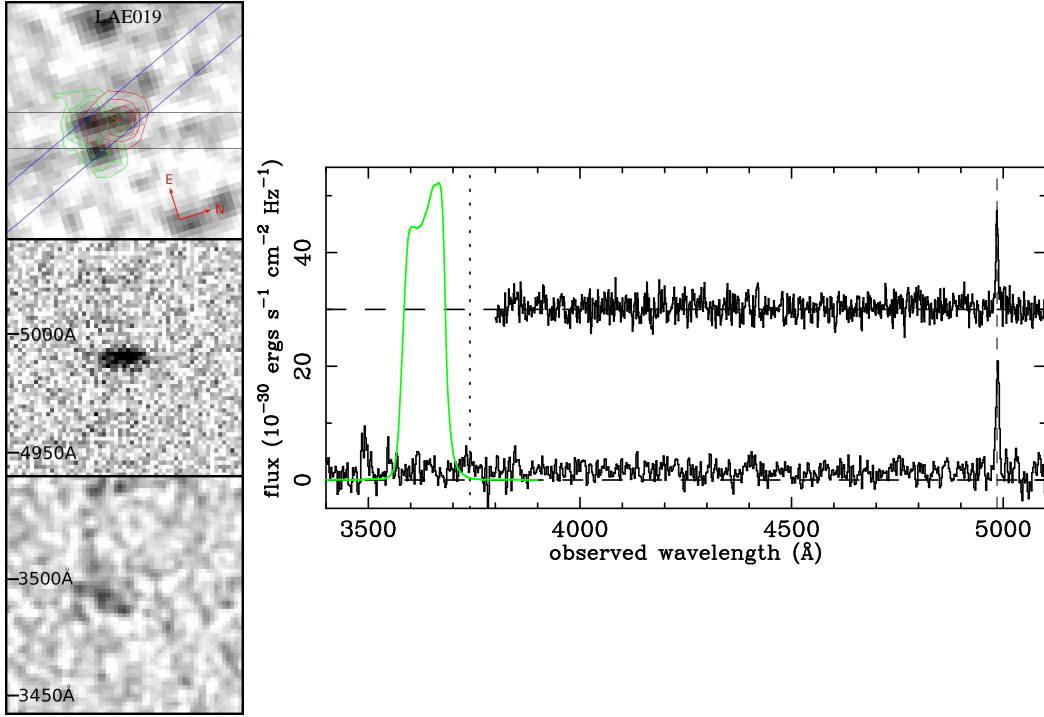


FIG. 14.— The emission features of LAE019. Left: The top panel shows our BV image. The middle and bottom panels show the two-dimensional deep-mask spectrum in the regions of the redshifted Ly $\alpha$ , and the bluer emission line, respectively. Right: The extracted one-dimensional spectra of LAE019. Shown are both the shallow- (offset, upper) and deep-mask (lower) spectra. We identify the emission feature at  $\lambda = 4985$  Å as Ly $\alpha$  at redshift  $z = 3.101$ . The corresponding Lyman break is marked with a vertical dotted line. The bluer emission line can be seen at  $\lambda = 3490$  Å in the deep-mask spectrum.



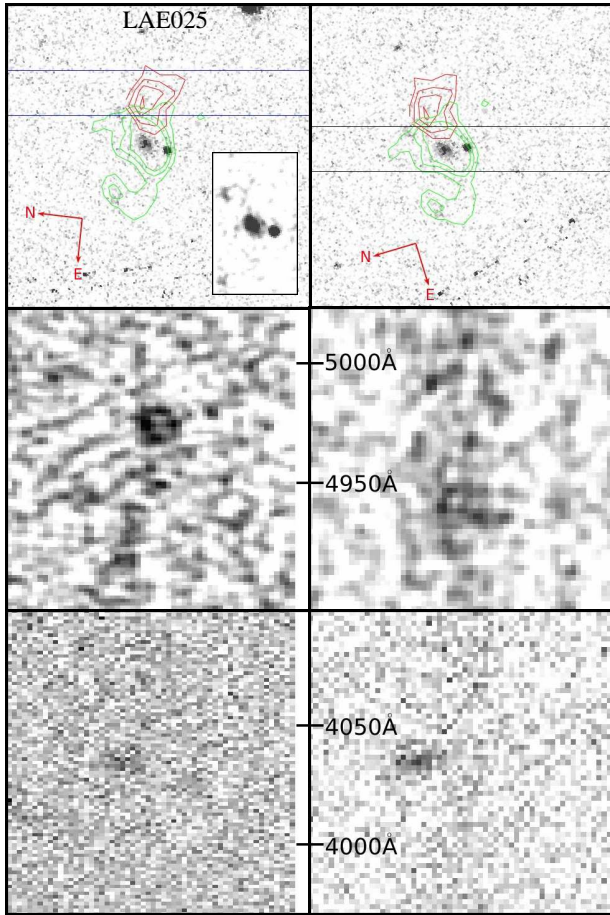


FIG. 15.— The emission features of LAE025. The top panels show the *HST*/ACS-F814W image. The boxes indicate the positions of the slits in the shallow- (left) and deep- (right) masks. The inset in the top-left panel shows the central region without contours after slight (2.35-pixel FWHM) smoothing. The middle panels show the two-dimensional spectra in the redshifted  $\text{Ly}\alpha$  region for the corresponding slit spectra, with an emission line at  $\simeq 4974\text{\AA}$  in the shallow-mask spectrum and, possibly, at  $\simeq 4942\text{\AA}$  in the deep-mask spectrum. The bottom panels show the two-dimensional spectra in the vicinity of the emission line at  $\simeq 4035\text{\AA}$ .

and the NB3640 flux is non-ionizing continuum emerging from this lower-redshift galaxy. It is noteworthy that the NB3640 flux is not centered on the portion of the F814W flux that we associate with the lower-redshift interloper, and extends to the north-west. However, due to the clear presence of an interloper we take the conservative approach and remove LAE003 from our list of possible LyC-leaking galaxies. The one-dimensional extracted spectra are shown in the right panel of Figure 13.

LAE003 had previously been studied by Inoue et al. (2011) who determined a spectroscopic redshift of  $z = 3.100$ . Their spectrum did not extend blueward enough to detect the emission line at  $\lambda = 3359\text{\AA}$ , however. As the NB3640 (NB359 in Inoue et al. 2011) flux is spatially coincident with the *R*-band and *LyA* flux for LAE003, these authors argue that the probability of foreground contamination is small and therefore the NB359 flux is indeed LyC. They interpret the implied very high ratio of ionizing to non-ionizing UV flux density of four objects, including LAE003, in terms of very young stellar

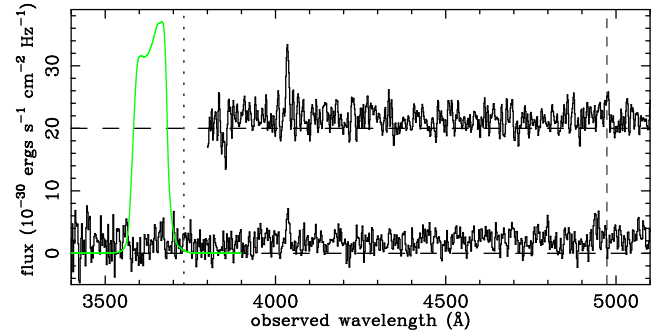


FIG. 16.— The extracted shallow- (offset, upper) and deep-mask (lower) spectra of LAE025. We identify the emission feature at  $\lambda = 4974\text{\AA}$  in the shallow-mask spectrum as  $\text{Ly}\alpha$  at redshift  $z = 3.091$ . The corresponding Lyman break is marked with a vertical dotted line. The bluer emission line at  $\lambda = 4035\text{\AA}$  can be seen in both spectra. The deep-mask spectrum appears to exhibit  $\text{Ly}\alpha$  emission at  $\lambda = 4942\text{\AA}$ , corresponding to  $z = 3.065$ . Also shown in green, below the Lyman limit, is the NB3640 filter transmission curve.

populations with top-heavy initial mass functions. This interpretation is invalidated for LAE003 by the discovery of the low-redshift interloper in our deep-mask spectrum. The case of LAE003 highlights the importance of obtaining spectra extending as far to the blue as possible for properly interpreting possible LyC-leaking galaxies.

#### LAE019

We do not have *HST* imaging of LAE019. The top panel of Figure 14 shows our *BV* image with the deep and shallow-mask slits indicated. The  $\text{Ly}\alpha$  emission centroid is slightly offset to the north in both the imaging and two-dimensional deep-mask spectrum (middle panel), while the NB3640 flux centroid is slightly offset to the south in our imaging. The deep-mask spectrum of LAE019, shown in Figure 14, also exhibits a bluer emission feature at  $\lambda \simeq 3490\text{\AA}$ . If this feature is  $\text{Ly}\alpha$  emission, it would indicate the presence of an interloper at  $z = 1.872$ . The bottom panel shows the two-dimensional spectrum in the  $\lambda \simeq 3490\text{\AA}$  region. This lower-redshift emission line is spatially consistent with the NB3640 flux, indicating that the NB3640 flux is likely due to the interloper. Therefore, we remove LAE019 from our list of possible LyC-leaking galaxies.

#### LAE025

We obtained spectra of LAE025 in both shallow and deep masks. The top panels of Figure 15 show the *HST*/ACS image, with the corresponding slit positions (shallow left; deep right). The inset in the top-left panel shows the central region without contours, after smoothing by a Gaussian kernel with  $\text{FWHM} = 2.35$  pixels ( $0''.1$ ). The bulk of the NB3640 flux is associated with the central clump. We detect flux in neither the F814W nor *BV* images at the location of the *LyA* flux centroid. The middle-left panel of Figure 15 shows the region of the two-dimensional shallow-mask spectrum corresponding to the expected location of the redshifted  $\text{Ly}\alpha$  line. We detect a strong emission line spatially coincident with the *LyA* flux, which we identify as  $\text{Ly}\alpha$  at  $z = 3.091$ . However, the non-ionizing UV flux detected in the *HST*/ACS image that is coincident with the NB3640 flux is just off of the slit. The middle-right panel shows the same



spectral region of the deep-mask spectrum, for which the slit was centered on the NB3640 detection. No obvious emission at  $\lambda \simeq 4974\text{\AA}$  is seen, as might be expected if the region coincident with the NB3640 flux was also at  $z = 3.091$ . Based on possible detections of Ly $\alpha$  emission at  $\lambda \simeq 4942\text{\AA}$  and perhaps corresponding SiII interstellar absorption, we tentatively assign a redshift of  $z = 3.065$ . This is a high enough redshift such that the NB3640 filter is still opaque to radiation longward of the Lyman limit. It should be noted, however, that the LAE at  $z = 3.091$  for which we searched for corresponding NB3640 flux would be unrelated to the  $z = 3.065$  object (the relative velocity between the two Ly $\alpha$  lines being  $\simeq 1800\text{ km s}^{-1}$ ) associated with the NB3640 flux; their proximity on the sky would be coincidental.

Further complicating this system is the presence of an additional, much bluer line at  $\lambda \simeq 4035\text{\AA}$ , which is detected in both spectra (Figure 16). It is spatially consistent with the faint, low surface-brightness flux detected in the F814W image to the north-northwest of the central clump, which falls in both slits. If identified as Ly $\alpha$ , it implies a redshift of  $z = 2.319$ .

With the data at hand it is difficult to either confirm or refute the claim that the detected NB3640 flux is ionizing continuum. Nonetheless, considering (a) there is evidence for a nearby foreground object, and (b) our identification of the redshift of the blob associated with the NB3640 emission is tentative, we remove LAE025 from our list of possible LyC detections.

#### 4.2.3. Unconfirmed LAE Candidates with NB3640 Detections

We were unable to confirm the redshifts of six of our LAE candidates with NB3640 detections. Of these six, we did not observe one, LAE084. The other five, LAE077, LAE087, LAE096, LAE101 and LAE102 all have relatively small photometrically-estimated REWs and upper-limits to their predicted detection significance (Section 3 and Table 3) between  $SL \simeq 1 - 6$ . Furthermore, their fluxes in the Ly $\alpha$  image are relatively diffuse (see Nestor et al. 2011, Figure 4). We remove these six systems from our statistical sample, but are not able to rule them out as  $z \simeq 3.09$  galaxies with escaping LyC flux.

#### 4.2.4. Summary: LAEs

Our original sample of LAE candidates from Nestor et al. (2011) contained 27 sources with NB3640 detections. Our new dataset includes spectra of 26 of these 27 sources. We were able to identify an emission line that we attribute to Ly $\alpha$  in 21 of the 26, although one source (LAE034) is at a redshift that is too low for inclusion in our sample. The other five sources with NB3640 detections may also be LAEs at  $z \simeq 3.1$  as our data are not of sufficient sensitivity to detect the expected Ly $\alpha$  emission line. However, we conservatively remove these five systems from our statistical sample. We also remove three LAEs with NB3640 detections that show evidence for foreground interlopers in the spectroscopic data. Thus, our current statistical sample of 91 spectroscopically confirmed  $z \geq 3.055$  LAEs contains 17 objects with NB3640 detections and no evidence for contamination of their NB3640 flux by foreground interlopers. We

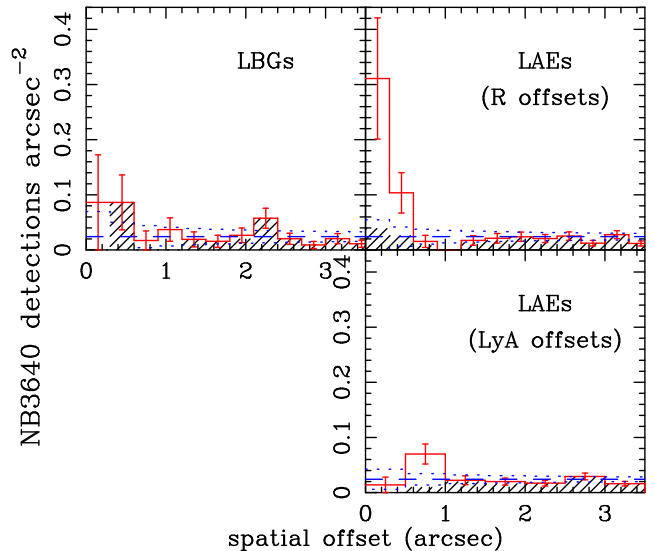


FIG. 17.— The radial surface density of NB3640 detections around galaxies in our LBG and LAE samples. The solid red histograms include all detected sources; the subset of these sources associated with obvious neighbors (which we have excluded as possible LyC detections, see §5.1) are represented by the hatched region. The dashed lines indicate the global surface density of sources in our NB3640 magnitude range and thus represent the expected levels of contamination, while the dotted lines represent the expected  $1\sigma$  scatter in the contamination. The excess surface density at low-offsets indicates that some of our low-offset LBG NB3640 detections and many of the low-offset LAE NB3640 detections are physically associated with the  $z \simeq 3.09$  sources and not random foreground interlopers. The top panels use the displacement of the LyC centroid from that of the  $R$  band detection (or  $BV$  or NB4980 for LAEs undetected in  $R$ ). The bottom panel uses displacements from the Ly $\alpha$  detections of LAEs. As the NB3640 detections tend to be more spatially coincident with the non-ionizing UV continuum than with the Ly $\alpha$  emission, the significance of the excess of surface density is greater when using the  $R$  band offsets.

stacked the NB3640 images of the 71 LAEs having no NB3640 detections and detected no flux down to an  $3\sigma$  limit on the average magnitude of  $m_{\text{NB3640}} = 28.39$ .

### 5. ACCOUNTING FOR LOWER-REDSHIFT INTERLOPERS AND IGM ABSORPTION

As in Nestor et al. (2011), we use the retained NB3640 detections in our samples to estimate the contributions to the cosmic ionizing background from LBGs and LAEs at  $z \sim 3$ . However, we must first account for two effects. Although we have removed from our samples targets with evidence of foreground galaxies contaminating their NB3640 flux measurements, the non-detection of emission or absorption features belonging to a lower-redshift system is not sufficient to rule out the presence of an interloper. Such an interloper may, for example, lack features strong enough to be detected in our data, lie at a redshift such that no strong spectral features fall within our wavelength coverage, or not be covered by the position of the slit. Not accounting for such interlopers would result in an overestimation of  $\epsilon_{\text{LyC}}$ . At the same time, the ionizing flux from LyC-leaking galaxies will experience an unknown amount of absorption by neutral gas in the intervening IGM, which will decrease the observed value of  $\epsilon_{\text{LyC}}$  relative to the intrinsic value. We

account for these two effects in a statistical manner using a pair of Monte Carlo simulations, which make use of the global surface density of NB3640 detections in the relevant magnitude range, and the observed Ly $\alpha$  forest statistics at  $z \simeq 3$ . The procedures are similar to those used by Shapley et al. (2006) and Nestor et al. (2011), but employ updated methods and statistics. We briefly summarize each method here.

### 5.1. Contamination Simulation

The centroids of the NB3640 detections in our samples are generally offset from the corresponding centroids of the non-ionizing UV emission. Many of these NB3640 detections, despite their relatively close proximity on the sky to LBGs and LAEs, have clear associations with unrelated neighboring sources and thus have already been rejected as possible LyC emission by Nestor et al. (2011). We have now also removed from our samples those galaxies with unconfirmed redshifts, and have rejected NB3640 detections displaying evidence for contamination in their LRIS or NIRSPEC spectra. In Figure 17 we show the resulting surface density of the total (open histogram) and rejected (hatched region) number of NB3640 detections, as a function of offset, for both the LBG and LAE samples. For the LAEs, we present surface densities computed using the offsets of the NB3640 detections from both the UV continuum (i.e.,  $R$ -band, or  $BV$  for LAE081 which is undetected in  $R$ ) and Ly $A$ -band centroids. The dashed line in Figure 17 indicates the global surface density of sources in the range of NB3640 magnitudes spanned by our detections,  $\rho_S = 0.024 \text{ arcsec}^{-2}$  over  $25 \leq m_{\text{NB3640}} \leq 27.25$ , which corresponds to the expected level of contamination. Both the LBG and LAE samples have, at relatively small ( $\lesssim 1''$ ) offsets, an excess of NB3640 detection surface density above the expected foreground level. In particular, the excess for the LAEs using  $R$ -band offsets is strikingly significant. In order to quantify the number NB3640 detections that may be due to foreground interlopers, in addition to those already rejected, we performed a Monte Carlo simulation using the observed surface densities of sources and predicted levels of contamination.

To account for the increased probability that NB3640 detections at larger offsets are contaminants, we considered each individual detection in turn, computing the contamination probability based on offset in the following manner. For the  $k^{\text{th}}$  detection, we constructed an annulus, having area  $A^k$ , encompassing the detection and centered on the non-ionizing UV flux centroid. We applied this same annulus to each of the  $N$  galaxies in the sample ( $N = 41$  or  $91$  for the LBG or LAE samples, respectively) and determined the number of previously rejected detections,  $n_{rej}^k$ , and putative LyC detections,  $n_{LyC}^k$ , contained within the  $N$  annuli. We then constructed the probability distribution for the number of expected random foreground interlopers,  $n_{fore}^k$ , in the regions spanned by the annuli:

$$P(n_{fore}^k) = \binom{N}{n_{fore}^k} p^{n_{fore}^k} (1-p)^{(N-n_{fore}^k)}, \quad (1)$$

where  $p = A^k \times \rho_S$  is the probability that a given LBG or LAE has a random foreground contaminant in  $A^k$

(see, e.g., Vanzella et al. 2010; Nestor et al. 2011). In each realization of the Monte Carlo simulation, we randomly chose a value for  $n_{fore}^k$  from  $P(n_{fore}^k)$ . Of these  $n_{fore}^k$  interlopers,  $n_{rej}^k$  had already been accounted for. Thus the number of *additional* interlopers predicted to lie within the  $N$  annuli is  $n_{fore}^k - n_{rej}^k$ . The NB3640 detection in question was flagged as an interloper if  $n_{fore}^k - n_{rej}^k \geq n_{LyC}^k$ , and was retained if  $n_{fore}^k - n_{rej}^k \leq 0$ . Otherwise, we randomly determined if the NB3640 detection was to be flagged as an interloper based on a probability  $= (n_{fore}^k - n_{rej}^k) / n_{LyC}^k$ . We then proceeded to the next (i.e.,  $k^{\text{th}} + 1$ ) detection and repeated the entire process. Once each possible LyC detection in the sample had been considered, we recorded the total predicted number of additional interlopers. The simulation was repeated for a total of 1000 iterations to determine the expected number and uncertainty in the average number of uncontaminated NB3640 detections.

The distribution of the number of NB3640 detections flagged as interlopers in each realization of the simulation is shown in Figure 18 for the LBG and LAE samples. The widths of the distributions depend slightly on the size of annular apertures used in the simulations due to NB3640 detections stochastically entering and exiting the apertures when their sizes were varied. The variability in the distribution widths was small and did not depend systematically on the aperture sizes. We used a circle of radius equal to the seeing FWHM in the NB3640 image ( $0''.8$ ) for detections with offsets  $\leq 0''.4$ . For detections at larger offsets, the radii of the annuli were set such that all values of  $A^k$  were equal. Our simulation suggests that  $2.6 \pm 1.2$  of the 6 possible LBGs with LyC detections are contaminated by foreground sources. Together with the three LBGs showing evidence for contamination in their spectra discussed in Section 4.1.2, the resulting contamination rate is  $62 \pm 13\%$  (i.e.,  $5.6 \pm 1.2$  of 9). The contamination-corrected detection rate for the sample as a whole is  $8 \pm 3\%$  ( $3.4 \pm 1.2$  of 41).

Using  $R$ -band offsets, our simulation suggests that  $3.8 \pm 1.3$  of the 17 possible LAEs with LyC detections are contaminated. Together with the three LAEs with contamination discussed in Section 4.2.2, the resulting contamination rate for the LAE sample is  $34 \pm 7\%$  ( $6.8 \pm 1.3$  of 20) and the contamination-corrected detection rate is  $15 \pm 1\%$  ( $13.2 \pm 1.3$  of 91). If we instead use Ly $A$  offsets, the predicted number additional contaminants becomes  $6.4 \pm 1.9$ , the contamination rate becomes  $47 \pm 10\%$  ( $9.4 \pm 1.9$  of 20) and the detection rate becomes  $12 \pm 2\%$  ( $10.6 \pm 1.9$  of 91).

In addition to estimating the number of foreground interlopers, our simulation computes the (contamination-corrected) average LyC and  $R$  magnitudes and uncertainties. The uncertainties include sample variance computed by first randomly reassigning individual magnitudes based on the measured magnitude and error, assuming Gaussian magnitude uncertainties determined from our photometric simulations, and then bootstrap re-sampling each data set. When computing the sample-average LyC magnitudes, we alternately assumed that NB4630 non-detections and detections flagged as interlopers had flux levels equal to zero or the maximum average magnitude consistent with the ( $1\sigma$ ) limits set by our

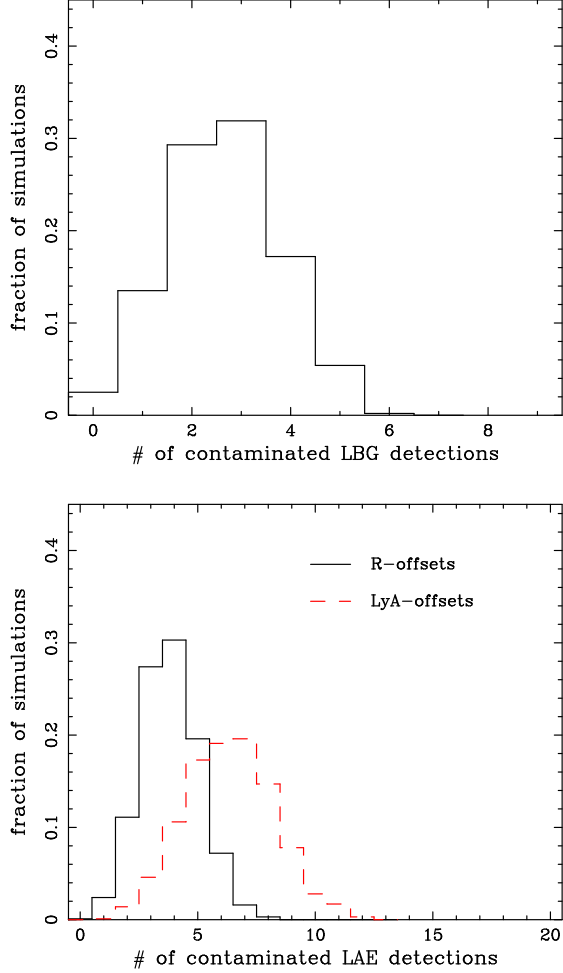


FIG. 18.— The distribution of the number of contaminated NB3640 detections as predicted by our Monte Carlo simulations, excluding the three LBGs and three LAEs showing evidence for foreground contamination in their spectra. The upper panel shows the results for the LBGs, which have a total of six possible LyC detections, while the lower panel shows the results for the LAEs, which have a total of 17 possible LyC detections. In the simulations, NB3640 detections with larger spatial offsets from the corresponding non-ionizing UV flux centroids are more likely to be flagged as interlopers. For the LAE sample, we considered offsets from both the  $R$  band (black solid histogram) and  $LyA$  (red dashed histogram) flux centroids.

stacking analysis. The resulting contaminated-corrected sample-average NB3640- $R$  colors are listed in Table 4.

### 5.2. IGM Simulation

To investigate the attenuation of escaping LyC flux by absorption from the IGM, we used the observed column density and frequency distributions of the Ly $\alpha$  forest over the relevant redshift range,  $1.7 \leq z \leq z_{\text{source}}$ , to model 500 random sightlines through the IGM for each LBG and LAE redshift. We then computed the attenuation of the continuum flux in the NB3640 filter due to the randomly generated neutral clouds. In this manner we determined the fraction of flux transmitted,  $t^j$ , for each of the 500 sightlines. The process was identical to that described in Nestor et al. (2011) except that we made use of updated estimates of the IGM opacity (Rudie et

al. 2012, in prep.) and a more precise treatment of the higher-order Lyman absorption lines from each cloud. As the galaxies in our sample lie either in or behind the SSA22a protocluster, it may be expected that the IGM in the proximate foreground of our sources is either more opaque due to the mass-overdensity of the region, or less opaque due to the overdensity of ionizing emissivity. In either scenario, the difference in average IGM opacity should manifest in differences in rest-frame UV colors that span Ly $\alpha$  emission and/or the Lyman limit. We compared the  $U - G$  and  $G - R$  colors for our sources at  $3.06 \leq z \leq 3.12$  with those of field LBGs in the same redshift range and found no statistical differences in their distributions, suggesting that any such effect is small in relation to our other uncertainties.

For each of the  $N$  redshifts in a sample, the expectation value for the fraction of transmitted flux,  $\langle t(z) \rangle$ , is simply the average of the 500 simulated  $t^j(z)$  values. For a single galaxy at  $z \simeq 3.09$ , the distribution of  $t$  is very broad, ranging from  $\approx 0 - 60\%$  (see, e.g., Figure 8 of Nestor et al. 2011). The uncertainty in  $t(z)$  is thus a major uncertainty in our estimate of the contribution to  $\epsilon_{\text{LyC}}$  from each individual source. The LBG and LAE *sample-average* LyC flux values, however, can be corrected with much less uncertainty. We define the sample-average transmission as

$$\bar{t}_{\text{sample}} \equiv \frac{\sum_{i=1}^N t(z_i) F_i}{\sum_{i=1}^N F_i}, \quad (2)$$

where  $F_i$  are the  $N$  individual intrinsic (i.e., prior to any IGM absorption) NB3640 fluxes, and  $t(z_i)$  are the actual IGM transmission values. As before,  $N = 41$  or 91 for the LBG or LAE samples, respectively. Although both the individual  $F_i$  and  $t(z_i)$  values are unknown, as the two sets are independent the expectation value for  $\bar{t}_{\text{sample}}$  is simply the average of the  $N$  values of  $\langle t(z) \rangle$ , and is thus independent of the values of  $F_i$  and  $t(z_i)$ . The uncertainty in  $\bar{t}_{\text{sample}}$ ,  $\sigma_{\bar{t}}$ , does depend on the  $t(z)$  and  $F$  distributions, however. While we have an accurate model for the probability distributions for the  $t(z_i)$  values, the  $F_i$  values are poorly constrained. In Nestor et al. (2011), we estimated  $\sigma_{\bar{t}}$  by randomly drawing the  $N$  values of  $t(z_i)$  from the corresponding  $t^j(z_i)$  values to compute  $\bar{t}_{\text{sample}}$ . We computed  $\bar{t}_{\text{sample}}$  in this manner 1000 times, and equated  $\sigma_{\bar{t}}$  to the standard deviation of the resulting  $\bar{t}_{\text{sample}}$  values. That procedure is equivalent to assuming the  $N$  values of  $F_i$  are all equal, and will underestimate  $\sigma_{\bar{t}}$  for more realistic distributions of  $F$ .

To improve upon our estimation of  $\sigma_{\bar{t}}$ , we assumed an exponentially decreasing function for the intrinsic flux probability distributions:  $p(F) \propto e^{-F/\beta}$ . This choice of parametrization has the advantage that the results are only mildly sensitive to the  $e$ -folding parameter,  $\beta$ . To determine the best choice for  $\beta$ , we convolved  $p(F)$  with the  $t(z)$  distributions for a range of  $\beta$  values. We then used the resulting attenuated-flux probability distributions to compute the likelihood of our contamination-corrected LBG and LAE NB3640 data sets, retaining the value of  $\beta$  that maximized these likelihoods. To determine  $\sigma_{\bar{t}}$ , we randomly selected the  $N$   $F_i$  values from the maximum likelihood exponential distributions. For each flux value, we also randomly selected  $t(z_i)$  from one of

the sets of  $t^j(z_i)$  values. These  $F_i$  and  $t(z_i)$  values were used with Equation 2 to determine  $\bar{t}_{sample}$ . This process was repeated 1000 times, and  $\sigma_{\bar{t}}$  was set equal to the standard deviation in the 1000 simulated  $\bar{t}_{sample}$  values.

We found that an exponential form for  $p(F)$ , when convolved with our modeled IGM transmission values, resulted in a qualitatively acceptable match to our observed NB3640 fluxes. However, as the actual  $F$  distributions are only poorly constrained by the data, it is likely that other functional forms are also able to match the observations and may result in different estimates of  $\sigma_{\bar{t}}$ . In particular, if the true  $p(F)$  distributions contain a spike at zero flux (as suggested by our non-detection of NB360 flux in the stacked images of the non-detections), we would still be underestimating  $\sigma_{\bar{t}}$ . Nonetheless, as our exponential model represents an improvement over the past method which effectively assumed  $p(F) = \text{constant}$ , and the error budget in  $\epsilon_{LyC}$  is not dominated by the uncertainty in  $\bar{t}_{sample}$ , we adopt the  $\sigma_{\bar{t}}$  values determined with an exponential  $p(F)$ .

For our LBG sample, we found  $\bar{t}_{sample} = 0.298 \pm 0.040$ , and for our LAE sample we found  $\bar{t}_{sample} = 0.320 \pm 0.027$ . We used these values to correct the sample-average NB3640 magnitudes and NB3640- $R$  colors. These colors can be expressed in terms of the sample-average UV-to-LyC flux-density ratios,  $\eta \equiv \langle F_{UV}/F_{LyC} \rangle$ . After applying the contamination and IGM corrections, we find  $\eta_{LBG} = 18.0_{-7.4}^{+34.8}$  for our LBG sample, and  $\eta_{LAE} = 3.7_{-1.1}^{+2.5}$  for our LAE sample. These values are consistent with, though larger than, those estimated by Nestor et al. (2011):  $\eta_{LBG} = 11.3_{-5.4}^{+10.3}$  for LBGs and  $\eta_{LAE} = 2.2_{-0.6}^{+0.9}$  for LAEs. The relative uncertainties in our updated estimates of  $\eta$  are larger than those in our previous estimates, due to an improved treatment of the errors. The updated samples also contribute to the increased relative uncertainties, as the newly confirmed LBGs have, on average, larger  $R$ -band photometric uncertainties than those in the previous sample, and the spectroscopically-confirmed LAE sample used here is smaller than the full photometrically-selected LAE sample. Nonetheless, by refining our samples and including empirical evidence for the presence or absence of foreground contamination in individual systems, our revised values represent improved estimates of  $\eta$  for LBGs and LAEs at  $z \sim 3$ . We list the colors and  $\eta$  values in Table 4 for our raw LBG and LAE samples, for those samples after application of the contamination corrections, and after correcting for both contamination and IGM absorption. The contamination- and IGM-corrected values are used below to estimate  $\epsilon_{LyC}$ .

## 6. RESULTS

### 6.1. Revised Estimate of $z \simeq 3.01$ LyC Emissivity

One of the primary goals of this paper is to determine the global luminosity space density of ionizing radiation,  $\epsilon_{LyC}$ , contributed by star-forming galaxies at  $z \sim 3$ . As the SSA22 protocluster represents an overdense volume of the Universe, computing  $\epsilon_{LyC}$  directly from our data would overestimate the space density of ionizing flux. However, the UV-continuum luminosity functions of LBGs and LAEs have been measured over relatively representative volumes, at rest-frame effective wavelengths close to those of our  $R$ -band data

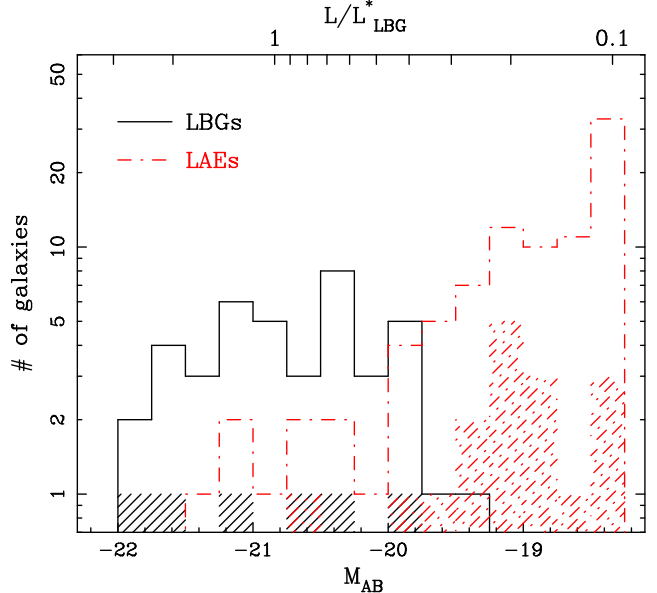


FIG. 19.— The rest-frame  $\lambda \sim 1600$  Å absolute magnitude distribution for our LBG (solid black) and LAE (dash-dot red) samples. The hatched regions indicate galaxies with NB3640 detections. The faintest bin in the LAE histogram also contains the 10 LAEs fainter than our detection limit of  $M_{AB} = -18.3$ . The top axis indicates the corresponding luminosity relative to the LBG characteristic luminosity  $L_{LBG}^*$ . Our LBG sample is dominated by galaxies brighter than  $M_{AB} = -20$ , corresponding to  $L \simeq 0.46 L_{LBG}^*$ , while our LAE sample is dominated by sources fainter than  $M_{AB} = -20$ .

( $\lambda \sim 1600$  Å), by Reddy et al. (2008) and Ouchi et al. (2008), respectively. Thus, we can use the values determined for the sample-average UV-to-LyC flux-density ratios together with the corresponding luminosity functions to determine  $\epsilon_{LyC}$ :

$$\epsilon_{LyC} = \int \frac{1}{\eta} L \Phi dL, \quad (3)$$

where  $L$  refers to the *non-ionizing* UV continuum luminosity, and  $\eta$  may be a function of  $L$ . When determined in this fashion, the value computed for  $\epsilon_{LyC}$  will depend on the choices of shape and normalization for the luminosity function, and the range in luminosity over which Equation 3 is integrated.

Reddy et al. (2008) give Schechter function parameters for the  $\lambda \sim 1700$  Å UV-continuum luminosity function of LBGs at  $z \sim 3$  of  $\phi_{LBG}^* = 1.66 \times 10^{-3} \text{ Mpc}^{-3}$ ,  $M_{LBG}^* = -20.84$ , and  $\alpha_{LBG} = -1.57$ . For LAEs at  $z \sim 3.1$ , Ouchi et al. (2008) determine  $\lambda \sim 1600$  Å UV-continuum luminosity function parameters of  $\phi_{LAE}^* = 0.56 \times 10^{-3} \text{ Mpc}^{-3}$ ,  $M_{LAE}^* = -19.8$ , and  $\alpha_{LAE} = -1.6$ . However, their luminosity function is determined for LAEs having  $\text{REW} \gtrsim 64$  Å, while our sample has  $\text{REW} \gtrsim 20$  Å. From the REW distribution determined by Gronwall et al. (2007), we estimate that LAEs represented by our sample are a factor of  $\approx 1.8$  more common at  $z \sim 3$  than those described by Ouchi et al. (2008). We therefore adopt  $\phi_{LAE}^* = 1.01 \times 10^{-3} \text{ Mpc}^{-3}$  for our LAE



sample.<sup>4</sup>

The absolute magnitude distributions for our LBG and LAE samples are shown in Figure 19. Spectroscopic confirmation of color-selected LBGs in the SSA22a field was limited to  $\mathcal{R} \leq 25.5$ . Consequently, the bulk of our LBG sample is brighter than  $M_{AB} = -20$ . In contrast, our LAE sample, which includes galaxies down to our photometric limit of  $R = 27.3$  (or  $M_{AB} \simeq -18.3$  at  $z \simeq 3.09$ ), is dominated by galaxies fainter than  $M_{AB} = -20$ . Thus, we first compute the contributions to  $\epsilon_{LyC}$  from LBGs and LAEs separately, and only from sources within the UV-continuum luminosity ranges over which we determined the values of  $\eta$ :  $M_{AB} \leq -20.0$  for our LBG sample, and  $-20 < M_{AB} \leq -18.3$  for our LAE sample. The absolute magnitude limits  $M_{AB} = -20.0$  and  $-18.3$  correspond to  $L_{min} = 0.46L_{LBG}^*$  and  $0.1L_{LBG}^*$ , respectively. With these magnitude ranges, the parameters for the respective luminosity functions discussed above, and  $\eta_{LBG} = 18.0^{+34.8}_{-7.4}$  for LBGs and  $\eta_{LAE} = 3.7^{+2.5}_{-1.1}$  for LAEs as determined in Section 5, we find  $\epsilon_{LyC}^{LBG} = 5.2^{+3.6}_{-3.4} \times 10^{24}$  ergs s<sup>-1</sup> Hz<sup>-1</sup> Mpc<sup>-3</sup> for  $M_{AB} \leq -20.0$  and  $\epsilon_{LyC}^{LAE} = 6.7^{+3.6}_{-3.4} \times 10^{24}$  ergs s<sup>-1</sup> Hz<sup>-1</sup> Mpc<sup>-3</sup> for  $-20 < M_{AB} \leq -18.3$ .

We now turn our attention to the total contribution to  $\epsilon_{LyC}$  from *all* star-forming galaxies brighter than  $M_{AB} = -18.3$  at  $z \sim 3$ . First, however, we must address the principle source of the large (factor of  $\sim 5$ ) difference between the values determined for  $\eta$  in our LBG and LAE samples. As the LBG and LAE samples are dominated by galaxies with relatively bright and faint UV-continuum luminosities, respectively, it may be that  $\eta$  has a strong dependence on galaxy luminosity. In this scenario, which we refer to as our luminosity-dependent  $\eta$  model, we identify  $\eta_{LBG}$  with *all* star forming galaxies having  $M_{AB} \leq -20.0$  and  $\eta_{LAE}$  with *all* star forming galaxies having  $-20 < M_{AB} \leq -18.3$ . Here we make the approximation that the Reddy et al. (2008) luminosity function, which is determined from color-selected galaxies, is a complete census of all star-forming galaxies with  $M_{AB} \leq -18.3$ ; i.e., that there are no sources brighter than this limit that contribute to  $\epsilon_{LyC}$  at  $z \sim 3$  with UV colors such that they would not be selected as LBGs. With these assumptions we can integrate Equation 3 piecewise:

$$\epsilon_{LyC}^{lum.-dep.} = \frac{1}{\eta_{LAE}} \int_{0.1L^*}^{0.46L^*} L \Phi_{LBG} dL + \frac{1}{\eta_{LBG}} \int_{0.46L^*}^{\infty} L \Phi_{LBG} dL, \quad (4)$$

finding  $\epsilon_{LyC}^{lum.-dep.} = 32.2^{+12.0}_{-11.4}$  ergs s<sup>-1</sup> Hz<sup>-1</sup> Mpc<sup>-3</sup>, with contributions from sources fainter and brighter than  $M_{AB} = -20$  of  $27.0^{+11.4}_{-10.9} \times 10^{24}$  ergs s<sup>-1</sup> Hz<sup>-1</sup> Mpc<sup>-3</sup> and  $5.2^{+3.6}_{-3.4} \times 10^{24}$  ergs s<sup>-1</sup> Hz<sup>-1</sup> Mpc<sup>-3</sup>, respectively. This value of  $\epsilon_{LyC}^{lum.-dep.}$  is  $\approx 60\%$  of that estimated in

Nestor et al. (2011), primarily due to our refined values for  $\eta_{LBG}$  and  $\eta_{LAE}$ .

Alternatively, the large difference in  $\eta$  between the LBG and LAE samples may be driven by some property of star-forming galaxies associated with LAEs. In this scenario, which we refer to as our LAE-dependent  $\eta$  model, we can estimate the total value of  $\epsilon_{LyC}$  by assuming  $\eta_{LAE}$  holds for all LAEs over the full range  $M_{AB} \leq -18.3$ , and  $\eta_{LBG}$  is representative of all LBGs with  $M_{AB} \leq -18.3$  that are not also LAEs. The fraction of LBGs that are not LAEs is determined from the LBG and LAE space densities, which can be computed by integrating the respective LBG and LAE luminosity functions,  $\rho = \int_{L_{min}}^{\infty} \Phi dL$ .<sup>5</sup> Setting  $L_{min} = 0.1L_{LBG}^*$ , we estimate that 23% of LBGs are also LAEs with  $REW \gtrsim 20\text{\AA}$ , which is consistent with past results at  $z \sim 3$  (Steidel et al. 2000; Shapley et al. 2003; Kornei et al. 2010). Here we have made the approximation that LAEs comprise a sub-sample of LBGs; i.e., that all LAEs at  $z \sim 3$  with  $M_{AB} \leq -18.3$  would meet the color-selection criteria used by Reddy et al. (2008). Equation 3 then becomes:

$$\epsilon_{LyC}^{LAE-dep.} = \frac{0.77}{\eta_{LBG}} \int_{0.1L^*}^{\infty} L \Phi_{LBG} dL + \frac{1}{\eta_{LAE}} \int_{0.1L^*}^{\infty} L \Phi_{LAE} dL, \quad (5)$$

resulting in  $\epsilon_{LyC}^{LAE-dep.} = 16.8^{+6.9}_{-6.5} \times 10^{24}$  ergs s<sup>-1</sup> Hz<sup>-1</sup> Mpc<sup>-3</sup>, with contributions from non-LAE and LAE galaxies of  $8.2^{+5.8}_{-5.5} \times 10^{24}$  ergs s<sup>-1</sup> Hz<sup>-1</sup> Mpc<sup>-3</sup> and  $8.6^{+3.7}_{-3.5} \times 10^{24}$  ergs s<sup>-1</sup> Hz<sup>-1</sup> Mpc<sup>-3</sup>, respectively.

This value of  $\epsilon_{LyC}^{LAE-dep.}$  is similar to that estimated for just LBGs with  $L \geq 0.1L^*$  in Nestor et al. (2011), and  $\approx 30\%$  of the total value of  $\epsilon_{LyC}$  estimated by Nestor et al. (2011). This difference is due to the combination of our improved measurements of  $\eta_{LBG}$  and  $\eta_{LAE}$  and the reduced contribution from sources with low values of  $\eta$  in our LAE-dependent model.

It is difficult, given the present data, to distinguish which of the luminosity-dependent or LAE-dependent  $\eta$  models is more appropriate. In Nestor et al. (2011), we investigated differences in the average Ly $\alpha$  emission strengths of systems with NB3640 detections compared to those without detections by creating stacks of LRIS spectra of our LBGs, and by comparing the distributions of photometrically-estimated Ly $\alpha$  REWs of our LAEs. For both LBGs and LAEs, we found that systems with NB3640 detections tend to have weaker Ly $\alpha$  emission relative to those not detected in NB3640. We repeated these tests using our refined LBG and LAE samples and excluding systems showing evidence for contamination in their spectra, and found trends consistent with our previous results. Thus, it is unlikely that Ly $\alpha$  emission strength has a direct influence on the average value of  $\eta$ . However, the LyC properties of  $z \sim 3$  galaxies may be dependent on some other property or combination of properties, such as star formation surface density, stellar pop-

<sup>4</sup> Although the UV luminosity function of LAEs having  $20\text{\AA} \leq REW \lesssim 64\text{\AA}$  (which compose  $\sim$  half of LAEs with  $REW \geq 20\text{\AA}$ ) may, in principle, have different values of  $M^*$  and  $\alpha$  compared to LAEs with  $REW \geq 64\text{\AA}$ , we proceed under the assumption that the Ouchi et al. (2008) values for  $M^*$  and  $\alpha$  apply for our entire range of REW.

<sup>5</sup> In this simple model, we do not account for the observed luminosity dependence of the fraction of LBGs that are also LAEs (see, e.g., Stark et al. 2010).

ulation age, metallicity, etc., that is more typical of the LAEs in our sample compared to our LBGs, independent of UV-continuum luminosity. For example, in a sample of local LBG analogs, Heckman et al. (2011) present evidence for small covering factors for optically thick neutral gas in the most compact galaxies in their sample. Indeed, in the available *HST*/ACS F814W imaging, the LAEs in our sample do appear, qualitatively, more compact on average than the LBGs. Nonetheless, as our LBG and LAE samples are largely distinct in magnitude range, future work including including fainter LBGs and larger LAE samples is needed to clearly differentiate between the two proposed scenarios.

We summarize the various contributions to  $\epsilon_{LyC}$  in Table 5. The uncertainties in the values of  $\epsilon_{LyC}$  are dominated by the uncertainties in our estimates  $\eta$ , which are large compared to the errors in the first moments of the luminosity functions. The uncertainties in  $\epsilon_{LyC}$  do not, however, include systematic errors arising from our choice of luminosity functions. For example, Reddy & Steidel (2009) find a steeper faint-end slope at  $z \sim 3$  previous works (see discussion in Reddy & Steidel 2009). Furthermore, in estimating  $\eta$  we have only accounted for the contribution from galaxies brighter than  $0.1L^*$ , i.e., the luminosity range over which we have empirical estimates of  $\eta$ . We note that, for the Reddy et al. (2008) luminosity function, galaxies fainter than  $0.1L^*$  contribute  $\sim 40\%$  of the luminosity density at  $1600\text{\AA}$ .

Given the spectral shape of the ionizing continuum flux and the mean free path to ionizing radiation in the IGM,  $\lambda_{mfp}$ , the value of  $\epsilon_{LyC}$  implies a corresponding (proper) hydrogen photoionization rate in the IGM,  $\Gamma_{HI}$ . If we assume a power law form for the LyC flux density such that  $f_\nu \propto \nu^{-\alpha}$ , then

$$\Gamma_{HI} = \frac{(1+z)^3 \sigma_{HI} \lambda_{mfp}}{h(3+\alpha)} \epsilon_{LyC}^{all, L \geq 0.1L^*}. \quad (6)$$

where  $h$  is Planck's constant, and  $\sigma_{HI} = 6.3 \times 10^{-18} \text{ cm}^{-2}$  is the atomic hydrogen photoionization cross section at the Lyman limit. Following Nestor et al. (2011), we adopt  $\alpha = 3$  and  $\lambda_{mfp} = 75.6 \text{ Mpc}$ . For the two estimates of  $\epsilon_{LyC}$  determined above, we find  $\Gamma_{HI}^{lum.-dep.} = 2.7^{+1.0}_{-0.9} \times 10^{-12} \text{ s}^{-1}$  in our luminosity-dependent  $\eta$  model, and  $\Gamma_{HI}^{LAE-dep.} = 1.4 \pm 0.6 \times 10^{-12} \text{ s}^{-1}$  in our LAE-dependent  $\eta$  model.<sup>6</sup> We list these values of  $\Gamma_{HI}$  in Table 6, together with estimates of  $\Gamma_{HI}$  in the  $z \sim 3.1$  Ly $\alpha$  forest by Meiksin & White (2004), Bolton & Haehnelt (2007), and Faucher-Giguère et al. (2008). The values we obtain for  $\Gamma_{HI}$  are larger than the values reported in the literature by a factor of  $\approx 2 - 4$ , although they are consistent given the uncertainties with the literature values at  $\sim 2\sigma$  and  $\sim 1\sigma$ , for the luminosity- and LAE-dependent  $\eta$  assumptions, respectively.

## 6.2. Escape Fractions

<sup>6</sup> More recent estimates of the mean free path of ionizing photons at  $z \sim 3$  suggest  $\lambda_{mfp} = 63 \text{ Mpc}$  in the IGM, and  $\lambda_{mfp} = 49 \text{ Mpc}$  if the opacity contributed by the circum-galactic medium of LBGs is included (G. Rudie, private communication). Adopting these values would lead to estimates of  $\Gamma_{HI}$  that are 83% and 65%, respectively, of the values presented here.

It is often of interest to estimate the fraction of LyC radiation produced by star formation that escapes into the IGM,  $f_{esc}^{LyC}$ . This value can be useful for constraining models of star formation histories, star formation feedback in the interstellar medium (ISM), etc. Additionally,  $f_{esc}^{LyC}$  can provide a useful parametrization in reionization models. The value of  $f_{esc}^{LyC}$  can be estimated empirically by

$$f_{esc}^{LyC} = \frac{\eta^{stars}}{\eta} f_{esc}^{UV}, \quad (7)$$

where  $\eta^{stars}$  is the intrinsic ratio of UV-to-LyC luminosity densities in star-forming regions, and  $f_{esc}^{UV}$  is the escape fraction of non-ionizing UV radiation. Reddy et al. (2008) have estimated  $f_{esc}^{UV} \approx 20\%$  in LBGs at  $z \sim 3$ . LAEs, however, exhibit bluer average UV continua and smaller UV attenuation, with  $f_{esc}^{UV} \approx 30\%$  (e.g., Ouchi et al. 2008; Kornei et al. 2010; Blanc et al. 2011). The term  $\eta^{stars}/\eta$ , which is often referred to as the relative escape fraction, is a measure of the attenuation of the UV flux relative to that of the LyC flux. In this work we have estimated  $\eta$  for samples of LBGs and LAEs. The value  $\eta^{stars}$ , however, must be obtained from spectral synthesis models, and depends on the ages of the stellar populations. Even for a given star-formation history, various models produce differing values for  $\eta^{stars}$ . To illustrate the dependencies of the inferred value of  $f_{esc}^{LyC}$  on different models and parameters, we determined  $\eta^{stars}$  using the stellar population synthesis models of Bruzual & Charlot (2003, BC03), as well as a recent set of model integrated spectral energy distributions produced by The Binary Population and Spectral Synthesis code (BPASS, Eldridge & Stanway 2009), which includes the effects of massive binary stars and nebular emission. For each of the models we adopted a constant SFR and two different metallicities ( $Z = 0.004$  and  $0.020$ ) and measured  $\eta^{stars}$ , using our NB3640 and *R* filter passbands, at three ages ( $T = 10^6, 10^7$  and  $10^8 \text{ yr}$ ). The model values we obtain for  $\eta^{stars}$  range from  $\simeq 1.3$  for the  $T = 10^6 \text{ yr}$ ,  $Z = 0.004$  population in the BPASS models, to  $\simeq 6.4$  for the  $T = 10^8 \text{ yr}$ ,  $Z = 0.02$  population in the BC03 models. The complete set of modeled  $\eta^{stars}$  values are given in Table 7.

For a given combination of  $\eta$  and  $f_{esc}^{UV}$ , the modeled values of  $f_{esc}^{LyC}$  imply a corresponding  $f_{esc}^{LyC}$ . We show these  $f_{esc}^{LyC}$  values in Table 7 for each value of  $\eta^{stars}$ , assuming  $\eta_{LBG} = 18.0$  for LBGs and  $\eta_{LAE} = 3.7$  for LAEs, and adopting, in turn,  $f_{esc}^{UV} = 0.2$ ,  $f_{esc}^{UV} = 0.3$ , and the limiting dust-free case where  $f_{esc}^{UV} = 1$ . The  $f_{esc}^{LyC}$  values vary by factors of  $\sim 5 - 7$  for a given  $\eta$  and  $f_{esc}^{UV}$ . They vary from 1% for LBGs in the youngest  $f_{esc}^{UV} = 0.2$  BPASS model, to  $\sim 50\%$  for LAEs in the oldest  $f_{esc}^{UV} = 0.3$  BC03 models, and reach greater than unity for several of the dust-free LAE models. For a given  $f_{esc}^{UV}$  and  $\eta$ ,  $f_{esc}^{LyC}$  varies most with stellar population age, although the choice of BC03 or BPASS model also affects the inferred value of  $f_{esc}^{LyC}$  by as much as a factor of  $\sim 2$ . Over the range investigated, metallicity has only a small effect on  $f_{esc}^{LyC}$ . There are other model inputs that we have not varied, such as the stellar initial mass function or star-formation history, that are also likely to affect  $\eta^{stars}$  and therefore the determination of  $f_{esc}^{LyC}$ . With these caveats in mind, LBGs at  $z \sim 3$  have a median

age of  $\sim 300$  Myr (Kornei et al. 2010) with metallicities approaching  $\sim$  solar (Pettini et al. 2001; Shapley et al. 2004; Maiolino et al. 2008) and  $f_{esc}^{UV} \simeq 0.2$ , suggesting  $f_{esc}^{LyC, LBG} \simeq 5 - 7\%$ . High-redshift LAEs, in contrast, have typical ages  $\sim 20$  Myr (Gawiser et al. 2007), low metallicity (Finkelstein et al. 2011; Nakajima et al. 2012), and  $f_{esc}^{UV} \simeq 0.3$ , suggesting  $f_{esc}^{LyC, LAE} \simeq 10 - 30\%$ . In general, we caution against the naive use of LyC escape fractions in reionization models without consideration of the values of  $\eta^{stars}$  and  $f_{esc}^{UV}$  used in their determination.

In Table 4 we also list the values of  $\eta$  for only galaxies with LyC detections. Our sample of LBGs with LyC detections has  $\eta = 1.7_{-0.8}^{+1.7} \approx \eta^{stars}$  for most of our modeled  $\eta^{stars}$  values, with the exception of the older BC03 models, implying a  $\sim$  unity relative escape fraction in LBGs with LyC detections. Note that, as LyC radiation is more susceptible than non-ionizing UV radiation to attenuation by gas and dust,  $\eta \approx \eta^{stars}$  implies little attenuation and therefore a large value of  $f_{esc}^{UV}$ . For the LAEs with NB3640 detections, our IGM-corrected value  $\eta = 0.4_{-0.1}^{+0.2}$  is inconsistent with all of our modeled values of  $\eta^{stars}$  at more than  $3\sigma$  (note that it is unphysical to have  $\eta > \eta^{stars}$ ). We can bring our LAE detections-only value for  $\eta$  in line with the model predictions if we assume that we can only detect LyC in our LAE sample along fortuitously clear IGM sightlines, and therefore can neglect the IGM correction, resulting in  $\eta = 1.4_{-0.4}^{+0.7}$ . This scenario, however, is very unlikely.<sup>7</sup> Deciphering the correct interpretation of these surprising low values of  $\eta$  is a primary goal of our ongoing work, which includes *HST*/UVIS LyC and UV imaging of many of our NB3640 detections. Better multi-wavelength constraints on the stellar populations of NB3640-detected LAEs will also be a key component of determining their underlying nature.

In Section 5.1 we found a LyC detection rate of  $\sim 8\%$  in our LBG sample, and  $\sim 12 - 15\%$  in our LAE sample. While it is not clear if the LyC properties of a “typical”  $z \sim 3$  LBG or LAE are similar to that of the average system, these rates do indicate the solid angle over which LyC radiation escapes, at a level above our detection limit, averaged over all galaxies in each sample. In Nestor et al. (2011), we proposed a “blow out” model in which feedback from regions of dense star formation clear portions of the ISM of gas and dust. When viewed along favorable sightlines, such regions appear to have large escape fractions, as we find in our LBGs and LAEs with LyC detections. Galaxies that either have failed to sufficiently remove their ISM over significant solid angle, or are viewed along unfavorable sightlines, will appear to have negligible escape fractions. The strong LyC-flux upper-limits in systems without NB3640 detections, derived from our stacking analysis, are consistent with this picture. Additionally, in the subsample of our LAEs having *HST* imaging,<sup>8</sup> we find no significant difference

in the distributions of sizes or surface brightnesses for sources with and without NB3640 detections. The similarity of these properties between NB3640 detected and non-detected LAEs is consistent with a scenario in which viewing angle is a significant factor in the ability to detect escaping LyC.

## 7. DISCUSSION AND SUMMARY

Directly studying galaxies in the ionizing continuum is a difficult endeavor. The dearth of QSOs above  $z \sim 3$  suggests that, at high redshift, the ionization balance in the IGM is maintained by LyC flux escaping from star-forming galaxies. However, the increasingly opaque IGM makes the detection of any escaping LyC flux unlikely above  $z \sim 3.5$  (see, e.g., Vanzella et al. 2012). Below  $z \sim 2.4$ , the redshifted Lyman limit falls below the atmospheric cutoff requiring observations from space to detect ionizing flux. Current observations at  $z \approx 1.3$  sampling rest-frame  $\lambda \sim 700\text{\AA}$  have resulted only in upper limits to  $\epsilon_{LyC}$  (Siana et al. 2007, 2010). The non-detection of LyC emission at  $z \sim 1$  together with the apparent need for a galaxy contribution to  $\epsilon_{LyC}$  at high redshift implies that  $\epsilon_{LyC}$  evolves strongly over  $z \sim 1 - 3$  (see, e.g., Figure 9 of Nestor et al. 2011; Inoue et al. 2006). We note, however, that if the average UV to LyC flux-density ratio  $\eta$  is luminosity-dependent, the non-detection of LyC in star forming galaxies at  $z \sim 1.3$  could be due in part to a selection bias, as the galaxies observed by Siana et al. (2010) are preferentially bright.

In any case, short of a large space-based program, the window  $2.5 \lesssim z \lesssim 3.5$  offers the best opportunity to identify and study LyC-leaking galaxies. As this and other recent works have shown, however, difficulties remain even at  $z \sim 3$ . While the IGM is more transparent to ionizing radiation at  $z \sim 3$  compared to higher redshift, there remains an unknown level of IGM attenuation of escaping LyC flux. The only practical way to correct for the attenuation is by applying a statistical correction, determined through modeling of the IGM, to the sample-average LyC properties. In this work, we have improved upon past efforts to estimate this correction by using an updated estimate of the IGM opacity at  $z \sim 3$ , including a more precise treatment of the higher-order Lyman absorption lines, and developing a new method to obtain a more realistic estimate of the transmission uncertainties. For the sample-average IGM correction method to be effective, we require a relatively large statistical sample. This necessity presents a second difficulty, as each galaxy requires a deep observation at a large observatory to be detected in the UV and LyC at these redshifts. Thus, we conducted our observations in a single field that contains a large overdensity of galaxies in a narrow range of redshift, using Keck and archival Subaru and *HST* imaging data, and new Keck/LRIS multi-object spectroscopy. Our resulting LBG and LAE samples are the largest of their types to have been imaged below the Lyman limit in an attempt to identify LyC flux. The samples presented here are improvements of those in Nestor et al. (2011), through a  $\sim 60\%$  increase in the number of LBGs and the spectroscopic confirmation of  $\gtrsim 90\%$  of our LAE candidates. Finally, perhaps the most critical impediment to unambiguous identifi-

LBGs without NB3640 detections.

<sup>7</sup> The average of the largest 12% (equal to the LAE LyC detection rate) of our modeled IGM transmissions is 0.566. Even adopting this value for the IGM correction we find  $\eta = 0.79$ , which is still significantly below our lowest predicted value of  $\eta^{stars}$ .

<sup>8</sup> The number of LBGs with NB3640 detections and *HST* imaging is too small to make meaningful comparisons to the sample of

cation of leaking LyC at  $z \sim 3$  is the high sky surface density of foreground sources with observed-frame blue magnitudes similar to expected  $z \sim 3$  LyC magnitudes. Our new spectra mitigate this problem by allowing us to directly search for spectral features from galaxies at lower redshift nearby on the sky (and thus falling on the slit) to the  $z \sim 3$  galaxies. As in Nestor et al. (2011), we also statistically correct the samples for yet unidentified foreground contaminants, here using a slightly refined method. Overall, in addition to clarifying the interpretation of the NB3640 detections of several specific LBGs and LAEs, our new data have led to improved estimates of the galaxy contributions to the ionizing background flux and ionization rates. Our main results include:

1. We obtained spectra of 41 LBG candidates and confirm redshifts  $z > 2.45$  for 26. Of these 26, 16 have  $z > 3.055$  such that our NB3640 filter is opaque above the redshifted Lyman break. Together with the 25 previously identified  $z > 3.055$  LBGs in the field, our NB3640 image samples below the Lyman limit for a total of 41 confirmed LBGs at  $z > 3.055$ .
2. We obtained spectra of 96 of the 110 LAE candidates from Nestor et al. (2011). We confirm redshifts  $3.057 \leq z \leq 3.108$  for 87 of the candidates. An additional four candidates, which are also part of our LBG sample, have previously determined redshifts  $z > 3.055$ . Thus, our NB3640 image samples below the Lyman limit for a total of 91 confirmed LAEs.
3. Nine galaxies in our LBG sample are detected in NB3640. The spectra of three of these detections contain evidence for the presence of a lower-redshift interloper, and thus are removed from consideration as LyC leakers. Our Monte Carlo simulation suggests that an additional  $2.6 \pm 1.2$  of our NB3640 detections are contaminated. The resulting predicted contamination rate is  $62 \pm 13\%$ , and the predicted LyC detection rate is  $8 \pm 3\%$ .
4. We detect 20 galaxies in our LAE sample in the NB3640 image. The spectra of three of these detections contain evidence for the presence of a lower-redshift interloper, and thus are removed from consideration as LyC leakers. Our Monte Carlo simulation suggests that an additional  $6.4 \pm 1.9$  of our NB3640 detections are contaminated. The resulting predicted contamination rate is  $47 \pm 10\%$ , and the predicted LyC detection rate is  $12 \pm 2\%$ .
5. Using the sample-average NB3640- $R$  colors, we determined the sample-average UV-to-LyC flux-density ratios  $\eta = 18.0^{+34.8}_{-7.4}$  for our LBG sample and  $\eta = 3.7^{+2.5}_{-1.1}$  for our LAE sample. We then used these ratios, together with the  $z \sim 3$  LBG and LAE luminosity functions to estimate the contributions to  $\epsilon_{LyC}$  from each sample, over the luminosity ranges for which  $\eta$  was constrained:  $\epsilon_{LyC}^{LBG} = 5.2^{+3.6}_{-3.4} \times 10^{24} \text{ ergs s}^{-1} \text{ Hz}^{-1} \text{ Mpc}^{-3}$  for  $M_{AB} \leq -20$  and  $\epsilon_{LyC}^{LAE} = 6.7^{+3.6}_{-3.4} \times 10^{24} \text{ ergs s}^{-1} \text{ Hz}^{-1} \text{ Mpc}^{-3}$  for  $-20 < M_{AB} \leq -18.3$ . The total

galaxy contributions are  $\epsilon_{LyC}^{lum.-dep.} = 32.2^{+12.0}_{-11.4} \times 10^{24} \text{ ergs s}^{-1} \text{ Hz}^{-1} \text{ Mpc}^{-3}$  in our luminosity-dependent  $\eta$  model or  $\epsilon_{LyC}^{LAE-dep.} = 16.8^{+6.9}_{-6.5} \times 10^{24} \text{ ergs s}^{-1} \text{ Hz}^{-1} \text{ Mpc}^{-3}$  in our LAE-dependent  $\eta$  model, for galaxies with  $M_{AB} \leq -18.3$  which corresponds to  $L \simeq 0.1L_{LBG}^*$  at  $z \sim 3$ .

6. The intergalactic hydrogen photoionization rates  $\Gamma$  inferred by our values of  $\epsilon_{LyC}$ ,  $\Gamma_{HI}^{lum.-dep.} = 2.7^{+1.0}_{-0.9} \times 10^{-12} \text{ s}^{-1}$  in our luminosity-dependent  $\eta$  model, and  $\Gamma_{HI}^{LAE-dep.} = 1.4 \pm 0.6 \times 10^{-12} \text{ s}^{-1}$  in our LAE-dependent  $\eta$  model, are larger than but consistent with published values for  $\Gamma$  measured in the Ly $\alpha$  forest.
7. We use two suites of stellar population synthesis models to predict the intrinsic UV-to-LyC flux-density ratio in star-forming regions,  $\eta^{stars}$ , finding values that range from 1.3 – 6.4. The inferred sample-average values of  $f_{esc}^{LyC}$  for our samples depend on the assumed values of  $\eta^{stars}$  and  $f_{esc}^{UV}$ . Despite the uncertainty in these two values, our best estimates of  $f_{esc}^{LyC}$  are  $\sim 5 - 7\%$  for LBGs and  $\sim 10 - 30\%$  for LAEs. In our “blow out” model for LyC escape, we predict near-unity apparent escape fractions in galaxies with LyC detections, and negligible escape fractions in other systems.

Despite our significant progress, several outstanding issues remain. In order to assess the robustness of our contamination corrections, it is important to determine unambiguously the LyC or interloper nature of as many of our NB3640 detections as possible. For many of our galaxies with NB3640 detections, our LRIS and/or NIRSPEC data enable us to associate a redshift with one or more specific regions (or “clumps”) of non-ionizing UV flux. With the data at hand, we are already able to place high confidence on the association of NB3640 detections with  $z > 3.055$  clumps in at least two of our objects, MD46 and LAE053. We expect to increase the number of such high-confidence LyC identifications in the near future with our ongoing programs. Notably, the resolution afforded by our ongoing *HST*/UVIS cycle 19 imaging program will allow the measurement of  $F_{UV}/F_{LyC}$  in the individual clumps, thus providing strong constraints on the nature of the NB3640 detections. *K*-band and/or *Spitzer*/IRAC data, together with our rest-frame UV observations, will enable investigations of the stellar populations of galaxies with and without LyC detections. It is also necessary to extend our investigation to other fields in order to ensure that our results are not a phenomenon (or, e.g., a systematic bias) unique to the SSA22a field. To this end, we are in the process of finalizing a similar study in an independent field at  $z \sim 2.85$  (Mostardi et al., in prep). Finally, the recently commissioned near-IR multi-object spectrograph MOSFIRE at the Keck observatory will allow the study of rest-frame optical spectral features of galaxies with LyC detections.

We thank Gwen Rudie for providing us with updated measurements of the  $z \sim 2 - 3$  IGM opacity, and Gwen Rudie and Milan Bogosavljević for their assistance in



the collection of some of the data used in this paper. D.B.N., A.E.S. and K.A.K. acknowledge support from the David and Lucile Packard Foundation. C.C.S. acknowledges additional support from the John D. and Catherine T. MacArthur Foundation, the Peter and Patricia

Gruber Foundation, and NSF grants AST-0606912 and AST-0908805. We wish to extend special thanks to those of Hawaiian ancestry on whose sacred mountain we are privileged to be guests. Without their generous hospitality, most of the observations presented herein would not have been possible.

## REFERENCES

- Blanc, G. A., Adams, J. J., Gebhardt, K., Hill, G. J., Drory, N., Hao, L., Bender, R., Ciardullo, R., Finkelstein, S. L., Fry, A. B., Gawiser, E., Gronwall, C., Hopp, U., Jeong, D., Kelzberg, R., Komatsu, E., MacQueen, P., Murphy, J. D., Roth, M. M., Schneider, D. P., & Tufts, J. 2011, *ApJ*, 736, 31
- Bolton, J. S. & Haehnelt, M. G. 2007, *MNRAS*, 382, 325
- Bouwens, R. J., Illingworth, G. D., Oesch, P. A., Labbe, I., Trenti, M., van Dokkum, P., Franx, M., Stiavelli, M., Carollo, C. M., Magee, D., & Gonzalez, V. 2010, *ArXiv e-prints*
- Bridge, C. R., Teplitz, H. I., Siana, B., Scarlata, C., Conselice, C. J., Ferguson, H. C., Brown, T. M., Salvato, M., Rudie, G. C., de Mello, D. F., Colbert, J., Gardner, J. P., Giavalisco, M., & Armus, L. 2010, *ApJ*, 720, 465
- Bruzual, G. & Charlot, S. 2003, *MNRAS*, 344, 1000
- Bunker, A. J., Wilkins, S., Ellis, R. S., Stark, D. P., Lorenzoni, S., Chiu, K., Lacy, M., Jarvis, M. J., & Hickey, S. 2010, *MNRAS*, 1378
- Cowie, L. L., Barger, A. J., & Trouille, L. 2009, *ApJ*, 692, 1476
- Eldridge, J. J. & Stanway, E. R. 2009, *MNRAS*, 400, 1019
- Faucher-Giguère, C., Lidz, A., Hernquist, L., & Zaldarriaga, M. 2008, *ApJ*, 688, 85
- Finkelstein, S. L., Hill, G. J., Gebhardt, K., Adams, J., Blanc, G. A., Papovich, C., Ciardullo, R., Drory, N., Gawiser, E., Gronwall, C., Schneider, D. P., & Tran, K.-V. 2011, *ApJ*, 729, 140
- Gawiser, E., Francke, H., Lai, K., Schawinski, K., Gronwall, C., Ciardullo, R., Quadri, R., Orsi, A., Barrientos, L. F., Blanc, G. A., Fazio, G., Feldmeier, J. J., Huang, J., Infante, L., Lira, P., Padilla, N., Taylor, E. N., Treister, E., Urry, C. M., van Dokkum, P. G., & Virani, S. N. 2007, *ApJ*, 671, 278
- Grimes, J. P., Heckman, T., Aloisi, A., Calzetti, D., Leitherer, C., Martin, C. L., Meurer, G., Sembach, K., & Strickland, D. 2009, *ApJS*, 181, 272
- Gronwall, C., Ciardullo, R., Hickey, T., Gawiser, E., Feldmeier, J. J., van Dokkum, P. G., Urry, C. M., Herrera, D., Lehmer, B. D., Infante, L., Orsi, A., Marchesini, D., Blanc, G. A., Francke, H., Lira, P., & Treister, E. 2007, *ApJ*, 667, 79
- Heckman, T. M., Borthakur, S., Overzier, R., Kauffmann, G., Basu-Zych, A., Leitherer, C., Sembach, K., Martin, D. C., Rich, R. M., Schiminovich, D., & Seibert, M. 2011, *ApJ*, 730, 5
- Hopkins, P. F., Richards, G. T., & Hernquist, L. 2007, *ApJ*, 654, 731
- Inoue, A. K., Iwata, I., & Deharveng, J.-M. 2006, *MNRAS*, 371, L1
- Inoue, A. K., Kousai, K., Iwata, I., Matsuda, Y., Nakamura, E., Horie, M., Hayashino, T., Tapken, C., Akiyama, M., Noll, S., Yamada, T., Burgarella, D., & Nakamura, Y. 2011, *MNRAS*, 411, 2336
- Iwata, I., Inoue, A. K., Matsuda, Y., Furusawa, H., Hayashino, T., Kousai, K., Akiyama, M., Yamada, T., Burgarella, D., & Deharveng, J. 2009, *ApJ*, 692, 1287
- Kornei, K. A., Shapley, A. E., Erb, D. K., Steidel, C. C., Reddy, N. A., Pettini, M., & Bogosavljević, M. 2010, *ApJ*, 711, 693
- Krug, H. B., Veilleux, S., Tilvi, V., Malhotra, S., Rhoads, J., Hibon, P., Swaters, R., Probst, R., Dey, A., Dickinson, M., & Jannuzi, B. T. 2012, *ApJ*, 745, 122
- Lorenzoni, S., Bunker, A. J., Wilkins, S. M., Stanway, E. R., Jarvis, M. J., & Caruana, J. 2011, *MNRAS*, 414, 1455
- Maiolino, R., Nagao, T., Grazian, A., Cocchia, F., Marconi, A., Mannucci, F., Cimatti, A., Pipino, A., Ballero, S., Calura, F., Chiappini, C., Fontana, A., Granato, G. L., Matteucci, F., Pastorini, G., Pentericci, L., Risaliti, G., Salvati, M., & Silva, L. 2008, *A&A*, 488, 463
- Malkan, M., Webb, W., & Konopacky, Q. 2003, *ApJ*, 598, 878
- McLure, I. S., Becklin, E. E., Bendiksen, O., Brims, G., Canfield, J., Figer, D. F., Graham, J. R., Hare, J., Lacayanga, F., Larkin, J. E., Larson, S. B., Levenson, N., Magnone, N., Teplitz, H., & Wong, W. 1998, in *Proc. SPIE Vol. 3354*, p. 566-578, *Infrared Astronomical Instrumentation*, Albert M. Fowler; Ed., Vol. 3354, 566-578
- McLure, R. J., Dunlop, J. S., de Ravel, L., Cirasuolo, M., Ellis, R. S., Schenker, M., Robertson, B. E., Koekemoer, A. M., Stark, D. P., & Bowler, R. A. A. 2011, *MNRAS*, 418, 2074
- Meiksin, A. & White, M. 2004, *MNRAS*, 350, 1107
- Nakajima, K., Ouchi, M., Shimasaku, K., Hashimoto, T., Ono, Y., & Lee, J. C. 2012, *ArXiv e-prints*
- Nestor, D. B., Shapley, A. E., Steidel, C. C., & Siana, B. 2011, *ApJ*, 736, 18
- Oesch, P. A., Bouwens, R. J., Illingworth, G. D., Gonzalez, V., Trenti, M., van Dokkum, P. G., Franx, M., Labbe, I., Carollo, C. M., & Magee, D. 2012, *ArXiv e-prints*
- Oke, J. B., Cohen, J. G., Carr, M., Cromer, J., Dingizian, A., Harris, F. H., Labrecque, S., Lucinio, R., Schaal, W., Epps, H., & Miller, J. 1995, *PASP*, 107, 375
- Ono, Y., Ouchi, M., Mobasher, B., Dickinson, M., Penner, K., Shimasaku, K., Weiner, B. J., Kartaltepe, J. S., Nakajima, K., Nayyeri, H., Stern, D., Kashikawa, N., & Spinrad, H. 2012, *ApJ*, 744, 83
- Ota, K., Iye, M., Kashikawa, N., Shimasaku, K., Ouchi, M., Totani, T., Kobayashi, M. A. R., Nagashima, M., Harayama, A., Kodaka, N., Morokuma, T., Furusawa, H., Tajitsu, A., & Hattori, T. 2010, *ApJ*, 722, 803
- Ouchi, M., Shimasaku, K., Akiyama, M., Simpson, C., Saito, T., Ueda, Y., Furusawa, H., Sekiguchi, K., Yamada, T., Kodama, T., Kashikawa, N., Okamura, S., Iye, M., Takata, T., Yoshida, M., & Yoshida, M. 2008, *ApJS*, 176, 301
- Ouchi, M., Shimasaku, K., Furusawa, H., Saito, T., Yoshida, M., Akiyama, M., Ono, Y., Yamada, T., Ota, K., Kashikawa, N., Iye, M., Kodama, T., Okamura, S., Simpson, C., & Yoshida, M. 2010, *ApJ*, 723, 869
- Pentericci, L., Fontana, A., Vanzella, E., Castellano, M., Grazian, A., Dijkstra, M., Boutsia, K., Cristiani, S., Dickinson, M., Giallongo, E., Giavalisco, M., Maiolino, R., Moorwood, A., Paris, D., & Santini, P. 2011, *ApJ*, 743, 132
- Pettini, M., Shapley, A. E., Steidel, C. C., Cuby, J., Dickinson, M., Moorwood, A. F. M., Adelberger, K. L., & Giavalisco, M. 2001, *ApJ*, 554, 981
- Reddy, N. A. & Steidel, C. C. 2009, *ApJ*, 692, 778
- Reddy, N. A., Steidel, C. C., Pettini, M., Adelberger, K. L., Shapley, A. E., Erb, D. K., & Dickinson, M. 2008, *ApJS*, 175, 48
- Schenker, M. A., Stark, D. P., Ellis, R. S., Robertson, B. E., Dunlop, J. S., McLure, R. J., Kneib, J.-P., & Richard, J. 2012, *ApJ*, 744, 179
- Shapley, A. E., Erb, D. K., Pettini, M., Steidel, C. C., & Adelberger, K. L. 2004, *ApJ*, 612, 108
- Shapley, A. E., Steidel, C. C., Pettini, M., & Adelberger, K. L. 2003, *ApJ*, 588, 65
- Shapley, A. E., Steidel, C. C., Pettini, M., Adelberger, K. L., & Erb, D. K. 2006, *ApJ*, 651, 688
- Siana, B., Teplitz, H. I., Colbert, J., Ferguson, H. C., Dickinson, M., Brown, T. M., Conselice, C. J., de Mello, D. F., Gardner, J. P., Giavalisco, M., & Menanteau, F. 2007, *ApJ*, 668, 62
- Siana, B., Teplitz, H. I., Ferguson, H. C., Brown, T. M., Giavalisco, M., Dickinson, M., Chary, R., de Mello, D. F., Conselice, C. J., Bridge, C. R., Gardner, J. P., Colbert, J. W., & Scarlata, C. 2010, *ApJ*, 723, 241
- Stark, D. P., Ellis, R. S., Chiu, K., Ouchi, M., & Bunker, A. 2010, *MNRAS*, 408, 1628
- Steidel, C. C., Adelberger, K. L., Dickinson, M., Giavalisco, M., Pettini, M., & Kellogg, M. 1998, *ApJ*, 492, 428

- Steidel, C. C., Adelberger, K. L., Shapley, A. E., Pettini, M., Dickinson, M., & Giavalisco, M. 2000, *ApJ*, 532, 170  
—, 2003, *ApJ*, 592, 728
- Steidel, C. C., Pettini, M., & Adelberger, K. L. 2001, *ApJ*, 546, 665
- Steidel, C. C., Shapley, A. E., Pettini, M., Adelberger, K. L., Erb, D. K., Reddy, N. A., & Hunt, M. P. 2004, *ApJ*, 604, 534
- Trenti, M., Bradley, L. D., Stiavelli, M., Shull, J. M., Oesch, P., Bouwens, R. J., Muñoz, J. A., Romano-Diaz, E., Treu, T., Shlosman, I., & Carollo, C. M. 2012, *ApJ*, 746, 55
- Vanzella, E., Giavalisco, M., Inoue, A. K., Nonino, M., Fontanot, F., Cristiani, S., Grazian, A., Dickinson, M., Stern, D., Tozzi, P., Giallongo, E., Ferguson, H., Spinrad, H., Boutsia, K., Fontana, A., Rosati, P., & Pentericci, L. 2010, *ApJ*, 725, 1011
- Vanzella, E., Guo, Y., Giavalisco, M., Grazian, A., Castellano, M., Cristiani, S., Dickinson, M., Fontana, A., Nonino, M., Giallongo, E., Pentericci, L., Galametz, A., Faber, S. M., Ferguson, H. C., Grogin, N. A., Koekemoer, A. M., Newman, J., & Siana, B. D. 2012, *ApJ*, 751, 70
- Vanzella, E., Pentericci, L., Fontana, A., Grazian, A., Castellano, M., Boutsia, K., Cristiani, S., Dickinson, M., Gallozzi, S., Giallongo, E., Giavalisco, M., Maiolino, R., Moorwood, A., Paris, D., & Santini, P. 2011, *ApJ*, 730, L35
- Wilkins, S. M., Bunker, A. J., Stanway, E., Lorenzoni, S., & Caruana, J. 2011, *MNRAS*, 417, 717

## APPENDIX

## LAE LYMAN-CONTINUUM CANDIDATES

*LAE010*

We show the *HST*/ACS imaging and one-dimensional shallow-mask spectrum of LAE010 in the top panel of Figure 7. An emission line is clearly detected at  $\lambda = 4979\text{\AA}$ , indicating a redshift of  $z = 3.096$ . The shallow-mask slit also covers the position of the NB3640 detection. No additional emission features are detected in the spectrum. Thus, we retain LAE010 as a possible LyC-leaking galaxy.

*LAE016*

We show the *HST*/ACS imaging and one-dimensional shallow-mask spectrum of LAE016 in the middle panel of Figure 7. An emission line is clearly detected at  $\lambda = 4973\text{\AA}$ , indicating a redshift of  $z = 3.091$ . The NB3640 detection is weak and offset by  $0''.8$ , but covered by the slit. As no additional emission features are detected in the spectrum, we retain LAE016 as a possible LyC-leaking galaxy.

*LAE018*

The bottom panel of Figure 7 shows the *HST*/ACS image of LAE018 as well as the shallow and deep-mask spectra. An emission line at  $\lambda = 4976\text{\AA}$  is detected in both spectra, indicating  $z = 3.093$ . The *LyA* flux is centered on a compact source to the north east, while the NB3640 flux extends over more diffuse non-ionizing UV flux to the south and west. Both slits cover the NB3640 flux. However, no other emission features were detected in either spectrum. Thus, we retain LAE018 as a possible LyC-leaking galaxy.

*LAE021*

As we do not have *HST* imaging of LAE021, we show our *BV* image and shallow-mask spectrum in the top panel of Figure 8. An emission line is clearly detected at  $\lambda = 4948\text{\AA}$ , indicating a redshift of  $z = 3.070$ . No other emission features are detected and we retain LAE021 as a possible LyC-leaking galaxy. We note, however, that the NB3640 flux is offset by  $1''.4$  from the *LyA* flux, and is not covered by the shallow-mask slit. As with all of our retained NB3640 detections, we account for the possibility the NB3640 flux is due to a foreground interloper in our Monte Carlo simulation.

*LAE028*

We obtained spectra of LAE028 on both shallow and deep masks. The middle panel of Figure 8 shows the *HST*/ACS image. There is an offset of  $\simeq 0''.9$  between the *LyA* and NB3640 flux centroids, each of which is centered on an individual clump. An emission line is detected at  $\lambda \simeq 4973\text{\AA}$  in both spectra indicating a redshift of  $z = 3.088$ . No additional emission or absorption features are detected in either spectra. We therefore retain LAE028 as a possible LyC-leaking galaxy.

*LAE038*

We obtained spectra of LAE038 in the deep mask as well as two of the shallow masks. The *HST*/ACS image, the deep-mask spectrum and one of the shallow-mask spectra are shown in the bottom panel of Figure 8. An emission line at  $\lambda \simeq 4983\text{\AA}$ , indicating  $z = 3.099$ , is detected in each of the spectra. In all three of the spectra, the *Ly $\alpha$*  emission line is offset from the continuum by  $\simeq 0''.5$ . The directions and magnitude of the offsets are consistent with the continuum emanating from the location of NB3640 flux and the *Ly $\alpha$*  emission from the *LyA* flux. No additional lines are detected in any of the three spectra. We therefore retain LAE038 as a possible LyC-leaking galaxy.

*LAE039*

We show the *BV* image and shallow-mask spectrum of LAE039 in the top panel of Figure 9. We identify an emission line at  $\lambda = 4978\text{\AA}$ , indicating  $z = 3.095$ . No additional lines are detected. We therefore retain LAE039 as a possible LyC-leaking galaxy.

*LAE041*

We obtained spectra of LAE041 in the deep mask as well as two of the shallow masks. The *HST*/ACS image, the deep-mask spectrum and one of the shallow-mask spectra are shown in the middle panel of Figure 9. We identify an emission line at  $\lambda \simeq 4983\text{\AA}$ , indicating  $z = 3.066$ . No additional lines are detected in any of the three spectra. We therefore retain LAE041 as a possible LyC-leaking galaxy.

*LAE046*

We show our *BV* image and shallow-mask spectrum of LAE046 in the bottom panel of Figure 9. An emission line is detected at  $\lambda = 4984\text{\AA}$ , indicating a redshift of  $z = 3.100$ . No other emission features are detected and we retain LAE046 as a possible LyC-leaking galaxy. We note, however, that the NB3640 flux is offset by  $1''.8$  from the *LyA* flux, and is not covered by the shallow-mask slit. As with all of our retained NB3640 detections, we account for the possibility the the NB3640 flux is due to a foreground interloper in our Monte Carlo simulation.

*LAE048*

We show the *HST*/ACS image and shallow-mask spectrum of LAE048 in the top panel of Figure 10. An emission line is detected at  $\lambda = 4977\text{\AA}$ , indicating a redshift of  $z = 3.094$ . No other emission features are detected and we retain LAE048 as a possible LyC-leaking galaxy. We note, however, that the NB3640 flux is offset by  $1''.7$  from the *LyA* flux, and is not covered by the shallow-mask slit. As with all of our retained NB3640 detections, we account for the possibility the the NB3640 flux is due to a foreground interloper in our Monte Carlo simulation.

*LAE051*

We show the *HST*/ACS imaging and shallow-mask spectrum of LAE051 in the middle panel of Figure 10. An emission line is clearly detected at  $\lambda = 4977\text{\AA}$ , indicating a redshift of  $z = 3.094$ . The shallow-mask slit also covers the position of the NB3640 detection. No additional emission features are detected in the spectrum. Thus, we retain LAE051 as a possible LyC-leaking galaxy.

*LAE053*

We obtained spectra of LAE053 in one of the shallow masks and the deep mask. The bottom panel of Figure 10 shows the *HST*/ACS image and extracted spectra. There is an offset of  $\simeq 0''.9$  between the *LyA* and NB3640 flux centroids, each of which is centered on an individual clump. Each clump and corresponding *LyA* or NB3640 flux is covered by only one of the masks. A relatively broad emission line is detected at  $\lambda \simeq 4973\text{\AA}$  in the shallow-mask spectrum, indicating a redshift of  $z = 3.088$ . An absorption feature is detected in the deep mask at  $\lambda \simeq 4967\text{\AA}$  indicating  $\text{Ly}\alpha$  in absorption at  $z = 3.085$ . This absorption feature suggests that the NB3640 source is also at  $z \simeq 3.09$ . No other emission or absorption features are detected in either spectra. We therefore retain LAE053 as a possible LyC-leaking galaxy.

*LAE064*

We show the *HST*/ACS imaging and the combined shallow-mask spectrum of LAE064 in the top panel of Figure 11. An emission line is clearly detected at  $\lambda = 4994\text{\AA}$ , indicating a redshift of  $z = 3.108$ . Both slits also cover the position of the NB3640 detection, which is offset by  $1''.0$  from the *LyA* flux. The extraction apertures for the spectra shown were centered on the  $\text{Ly}\alpha$  line, which was offset from faint continuum emission consistent in magnitude ( $\sim 1''$ ) and direction from the position of the NB3640 flux. No additional emission features are detected in either (one- or two-dimensional) spectra. Thus, we retain LAE064 as a possible LyC-leaking galaxy.

*LAE069*

We show our *BV* image and shallow-mask spectrum of LAE069 in the middle panel of Figure 11. An emission line is detected at  $\lambda = 4953\text{\AA}$ , indicating a redshift of  $z = 3.074$ . No other emission features are detected and we retain LAE069 as a possible LyC-leaking galaxy. We note, however, that the NB3640 flux is offset from the *LyA* flux by  $0''.9$ , and is not covered by the shallow-mask slit.

*LAE074*

The bottom panel of Figure 11 shows the *HST*/ACS image of LAE074 as well as the shallow and deep-mask spectra. An emission line at  $\lambda = 4990\text{\AA}$  is detected in the shallow-mask spectrum, indicating  $z = 3.093$ . While the  $\text{Ly}\alpha$  emission line is not detected in the deep-mask spectrum, the slit covers only part of the diffuse *LyA* flux flux. No other emission features were detected in either spectrum. Thus, we retain LAE074 as a possible LyC-leaking galaxy.

*LAE081*

The top of Figure 12 shows the *HST*/ACS image of LAE081 as well as the shallow and deep-mask spectra. An emission line at  $\lambda = 4989\text{\AA}$  is detected in both spectra, indicating  $z = 3.104$ . Both slits cover the bulk of the *LyA* and NB3640 flux. No other emission features were detected in either spectrum. Thus, we retain LAE081 as a possible LyC-leaking galaxy.

*LAE083*

The bottom of Figure 12 shows the *HST*/ACS image of LAE083 as well as the shallow-mask spectrum. An emission line at  $\lambda = 4942\text{\AA}$  is detected, indicating  $z = 3.065$ . The slit also covers the bulk of the NB3640 flux. No other emission features were detected. Thus, we retain LAE083 as a possible LyC-leaking galaxy.



TABLE 1  
 THE  $z > 3.055$  LBG SAMPLE.

ID	RA (J2000)	Dec (J2000)	$z_{em}$ <sup>a</sup>	$z_{abs}$ <sup>b</sup>	$R$	NB3640	$\Delta_R$ <sup>c</sup>	$\frac{F_{UV}}{F_{LyC\ obs}}$ <sup>d</sup>
C3	22:17:32.53	00:10:57.4	3.098	3.091	24.59	...	...	> 12.1
C4	22:17:38.91	00:11:02.0	3.076	...	24.28	...	...	> 16.2
C7	22:17:24.60	00:11:31.3	...	3.062	24.06	...	...	> 19.8
C9	22:17:28.29	00:12:12.3	3.071	3.072	25.84	...	...	> 3.8
C11	22:17:25.68	00:12:35.4	3.101	3.096	24.21	...	...	> 17.3
C12	22:17:35.29	00:12:47.9	3.107	3.095	24.22	...	...	> 17.0
C14	22:17:34.04	00:12:51.3	3.220	...	25.67	26.43	0''1	$2.0 \pm 0.5$
C15	22:17:26.13	00:12:55.4	3.094	...	25.02	...	...	> 8.2
C16	22:17:31.95	00:13:16.3	...	3.065	23.62	26.43	1''9	$13.3 \pm 4.0$
C24	22:17:18.94	00:14:45.4	3.103	3.096	24.19	...	...	> 17.6
C26	22:17:39.54	00:15:15.6	3.178	...	25.01	...	...	> 8.2
C28	22:17:21.13	00:15:27.7	3.076	...	24.87	...	...	> 9.3
C30	22:17:19.29	00:15:45.0	3.104	3.097	23.70	...	...	> 27.5
C32	22:17:25.63	00:16:12.9	3.294	3.292	23.64	...	...	> 29.2
C35	22:17:20.23	00:16:52.5	...	3.098	24.06	...	...	> 19.7
C39	22:17:20.99	00:17:09.5	3.076	...	25.04	...	...	> 8.0
C47	22:17:20.24	00:17:32.5	3.075	3.065	23.78	...	...	> 25.7
C48	22:17:18.58	00:18:16.7	3.090	3.079	24.57	...	...	> 12.3
C49	22:17:19.81	00:18:18.8	3.163	3.149	23.81	26.84 <sup>e</sup>	0''4	...
C50	22:17:37.68	00:18:21.2	...	3.086	25.01	...	...	> 8.2
D3	22:17:32.40	00:11:33.6	3.074	3.066	23.92	...	...	> 22.4
D17	22:17:18.86	00:18:17.0	3.090	3.070	24.29	27.00	0''9	$12.2 \pm 5.1$
M2	22:17:33.51	00:11:10.8	3.388	3.386	25.19	25.99	0''8	$2.1 \pm 0.4$
M5	22:17:26.07	00:11:33.1	3.327	...	25.71	26.31 <sup>e</sup>	0''4	...
M6	22:17:28.13	00:11:40.5	3.180	...	25.65	...	...	> 4.6
M8	22:17:25.10	00:11:56.8	3.064	3.062	24.56	...	...	> 12.5
M10	22:17:26.80	00:12:21.3	3.103	3.095	24.50	...	...	> 13.1
M11	22:17:31.77	00:12:51.3	3.107	3.103	25.22	...	...	> 6.8
M13	22:17:31.46	00:12:55.2	3.107	...	25.38	...	...	> 5.9
M14	22:17:39.05	00:13:30.1	3.091	...	25.20	...	...	> 6.9
M19	22:17:36.90	00:15:00.9	...	3.082	24.96	...	...	> 8.6
M20	22:17:34.40	00:15:02.9	3.109	3.096	25.08	...	...	> 7.7
M25	22:17:31.49	00:16:31.2	3.098	3.091	24.79	...	...	> 10.1
M28	22:17:31.66	00:16:58.0	3.094	3.088	24.75	...	...	> 10.4
M29	22:17:37.40	00:17:08.8	...	3.228	24.93	26.76	1''0	$5.4 \pm 1.3$
M31	22:17:36.87	00:17:12.4	3.099	...	25.70	...	...	> 4.4
M34	22:17:33.80	00:17:57.2	...	3.084	25.41	...	...	> 5.7
MD14	22:17:37.91	00:13:43.9	...	3.097	24.49	...	...	> 13.4
MD23	22:17:28.01	00:14:29.6	3.085	3.075	24.34	...	...	> 15.2
MD32	22:17:23.70	00:16:01.6	3.102	...	25.14	25.51 <sup>e</sup>	0''4	...
MD46	22:17:27.28	00:18:09.7	3.091	3.080	23.49	25.22	1''0	$4.9 \pm 0.7$
aug96M16 <sup>f</sup>	22:17:30.86	00:13:10.8	...	...	24.47	25.23	0''7	$2.0 \pm 0.4$

<sup>a</sup> Ly $\alpha$  emission redshift.

<sup>b</sup> Interstellar absorption redshift.

<sup>c</sup> Spatial offset between the centroids of  $R$ -band and NB3640 emission.

<sup>d</sup> Observed ratio and uncertainty in non-ionizing UV and LyC flux densities, inferred from the NB3640– $R$  color. This value has not been corrected for either contamination by foreground sources or IGM absorption.

<sup>e</sup> Spectrum contains evidence for the presence of a foreground object. Thus, the NB3640 flux is likely contaminated by non-ionizing UV flux from the interloper.

<sup>f</sup> We were unable to determine the redshift of the LBG aug96M16, which in Nestor et al. (2011) was erroneously associated with a nearby galaxy with  $z_{em} = 3.298$ . We have removed it from our sample but include it in this table for completeness.

TABLE 2  
LBGS WITH NEW REDSHIFTS  $z < 3.055$ .

ID	RA (J2000)	Dec (J2000)	$z_{em}$ <sup>a</sup>	$z_{abs}$ <sup>b</sup>	$R$
C8	22:17:27.64	00:11:59.1	2.459	...	26.42
C19	22:17:38.36	00:14:16.4	2.993	...	24.84
D5	22:17:34.65	00:12:33.6	2.699	2.690	25.24
D10	22:17:38.92	00:14:32.1	...	2.605	24.61
M3	22:17:35.81	00:11:16.5	2.876	...	25.27
M16	22:17:24.66	00:14:07.8	3.021	3.018	24.88
M35	22:17:32.67	00:18:05.0	2.938	...	25.42
MD11	22:17:34.94	00:13:22.7	...	2.857	24.79
MD42	22:17:35.83	00:17:19.8	...	2.792	25.37
MD45	22:17:25.36	00:18:04.2	3.025	3.022	24.39

<sup>a</sup> Ly $\alpha$  emission redshift.

<sup>b</sup> Interstellar absorption redshift.

TABLE 3  
 SUMMARY OF LAE DATA

ID	RA (J2000)	Dec (J2000)	$R$	NB3640	$\Delta_R^a$	$\Delta_{LyA}^a$	$\frac{F_{UV}}{F_{LyC\,obs}}^b$	$z_{em}^c$
001 <sup>d,e</sup>	22:17:32.40	0:11:34.1	23.92	> 27.3	...	...	> 22.4	3.075
002 <sup>d,e</sup>	22:17:38.90	0:11:01.8	24.28	> 27.3	...	...	> 16.2	3.076
003	22:17:24.79	0:17:17.4	24.42	24.74 <sup>f</sup>	0''3	0''6	...	3.097
004 <sup>d,e</sup>	22:17:28.01	0:14:30.0	24.34	> 27.3	...	...	> 15.2	3.092
005	22:17:35.86	0:15:59.4	25.65	> 27.3	...	...	> 4.6	3.096
006	22:17:24.80	0:11:16.8	> 27.0	> 27.3	...	...	...	3.071
007	22:17:27.78	0:17:36.9	> 27.0	> 27.3	...	...	...	3.089
008 <sup>d,e</sup>	22:17:21.11	0:15:28.0	24.87	> 27.3	...	...	> 9.3	3.076
009 <sup>d</sup>	22:17:28.29	0:12:12.3	25.84	> 27.3	...	...	> 3.8	3.071
010	22:17:20.38	0:18:04.2	25.77	26.74	0''3	0''3	2.4 ± 1.1	3.096
011	22:17:33.85	0:12:14.9	26.07	> 27.3	...	...	> 3.1	3.102
012 <sup>d,e</sup>	22:17:31.69	0:16:57.6	24.75	> 27.3	...	...	> 10.5	3.094
013	22:17:27.18	0:16:21.7	25.98	> 27.3	...	...	> 3.4	3.095
014	22:17:19.25	0:14:50.9	25.82	> 27.3	...	...	> 3.9	3.067
015	22:17:21.84	0:12:12.7	> 27.0	> 27.3	...	...	...	3.067
016	22:17:35.61	0:18:00.2	26.24	26.91	0''9	0''8	1.8 ± 0.9	3.091
017	22:17:25.40	0:17:16.8	26.22	> 27.3	...	...	> 2.7	3.105
018	22:17:39.01	0:17:26.4	26.25	25.69	0''1	1''0	0.6 ± 0.2	3.093
019	22:17:26.15	0:13:20.1	25.70	26.24 <sup>f</sup>	0''4	0''9	...	3.101
020	22:17:37.33	0:16:31.4	25.45	> 27.3	...	...	...	...
021	22:17:18.77	0:15:18.1	> 27.0	27.17	1''3	1''4	< 1.8	3.070
022	22:17:19.68	0:11:49.4	26.11	> 27.3	...	...	> 3.0	3.066
023	22:17:31.73	0:16:06.9	24.91	> 27.3	...	...	> 9.1	3.101
024	22:17:34.17	0:16:09.7	26.73	> 27.3	...	...	> 1.7	3.096
025	22:17:36.74	0:16:28.8	25.54	25.85 <sup>f</sup>	0''3	1''2	...	3.091
026	22:17:18.96	0:12:00.8	26.59	> 27.3	...	...	> 1.9	3.092
027	22:17:24.94	0:17:17.3	26.25	> 27.3	...	...	> 2.6	3.101
028	22:17:31.80	0:17:17.9	25.50	26.71	0''3	0''9	3.1 ± 1.3	3.088
029 <sup>d</sup>	22:17:31.49	0:12:55.0	25.38	> 27.3	...	...	> 5.9	3.107
030	22:17:21.75	0:11:38.8	> 27.0	> 27.3	...	...	...	3.096
031	22:17:33.63	0:17:15.1	26.37	> 27.3	...	...	> 2.3	3.092
032	22:17:26.61	0:13:18.1	26.61	> 27.3	...	...	> 1.9	3.101
033	22:17:37.50	0:14:08.3	26.62	> 27.3	...	...	> 1.9	3.076
034	22:17:23.41	0:16:35.4	25.42	25.76 <sup>h</sup>	0''5	0''0	1.4 ± 0.4	3.044
035	22:17:27.03	0:13:13.2	> 27.0	> 27.3	...	...	...	3.093
036	22:17:22.25	0:11:55.1	> 27.0	> 27.3	...	...	...	3.084
037	22:17:20.96	0:18:07.3	25.61	> 27.3	...	...	> 4.7	3.089
038	22:17:34.77	0:15:41.3	26.17	25.82	0''1	0''7	0.7 ± 0.3	3.099
039	22:17:24.08	0:11:31.7	26.48	26.77	0''4	0''8	1.3 ± 0.7	3.095
040	22:17:31.93	0:13:08.5	> 27.0	> 27.3	...	...	...	3.105
041	22:17:24.54	0:15:06.7	25.97	25.94	0''4	0''5	1.0 ± 0.4	3.066
042	22:17:21.50	0:17:04.7	25.50	> 27.3	...	...	> 5.2	3.072
043	22:17:21.65	0:12:23.4	26.24	> 27.3	...	...	> 2.7	3.071
044	22:17:36.41	0:12:51.0	> 27.0	> 27.3	...	...	...	3.059
045	22:17:35.97	0:16:30.2	> 27.0	> 27.3	...	...	...	3.094
046	22:17:21.47	0:14:54.6	> 27.0	26.43	1''8	1''8	< 0.8	3.100
047	22:17:36.05	0:15:06.9	> 27.0	> 27.3	...	...	...	3.096
048	22:17:27.37	0:16:51.5	26.73	26.00	2''2	1''7	0.5 ± 0.2	3.094
049	22:17:39.29	0:16:10.5	> 27.0	> 27.3	...	...	...	3.094
050	22:17:24.56	0:15:56.8	> 27.0	> 27.3	...	...	...	3.082
051	22:17:33.72	0:15:04.9	26.26	27.21	0''3	0''7	2.4 ± 1.3	3.094
052	22:17:36.84	0:13:17.2	26.63	> 27.3	...	...	> 1.8	3.102
053	22:17:34.70	0:16:33.4	26.53	26.98	0''6	0''9	1.5 ± 0.8	3.090
054	22:17:39.05	0:11:33.9	26.25	> 27.3	...	...	> 2.6	3.096
055	22:17:35.80	0:11:50.0	26.67	> 27.3	...	...	> 1.8	3.072

TABLE 3  
SUMMARY OF LAE DATA (*Continued*)

ID	RA (J2000)	Dec (J2000)	$R$	NB3640	$\Delta_R^a$	$\Delta_{LyA}^a$	$\frac{F_{UV}}{F_{LyC}}^b_{obs}$	$z_{em}^c$
056	22:17:22.42	0:17:20.7	26.86	> 27.3	...	...	> 1.5	3.073
057	22:17:25.40	0:10:58.3	26.84	> 27.3	...	...	> 1.5	3.070
058	22:17:19.61	0:15:38.4	> 27.0	> 27.3	...	...	...	... <sup>i</sup>
059	22:17:24.98	0:12:30.0	25.31	> 27.3	...	...	> 6.2	3.096
060	22:17:28.19	0:11:17.1	26.61	> 27.3	...	...	> 1.9	3.065
061	22:17:34.10	0:15:40.2	> 27.0	> 27.3	...	...	...	3.101
062	22:17:22.87	0:14:41.7	26.53	> 27.3	...	...	> 2.0	3.057
063	22:17:23.32	0:15:52.9	26.55	> 27.3	...	...	> 2.0	3.099
064	22:17:35.42	0:12:14.6	26.05	26.74	0''1	1''0	1.9 ± 0.9	3.108
065	22:17:28.15	0:14:36.4	26.91	> 27.3	...	...	> 1.4	3.102
066	22:17:20.86	0:15:11.8	26.64	> 27.3	...	...	> 1.8	3.066
067	22:17:36.26	0:13:11.7	26.40	> 27.3	...	...	> 2.3	3.106
068	22:17:18.37	0:17:26.1	> 27.0	> 27.3	...	...	...	3.072
069	22:17:18.96	0:11:12.0	24.62	27.22	0''2	0''9	10.9 ± 5.1	3.074
070	22:17:39.28	0:14:00.2	25.98	> 27.3	...	...	> 3.4	3.090
071	22:17:21.61	0:12:20.5	26.77	> 27.3	...	...	> 1.6	3.072
072	22:17:31.24	0:17:32.1	27.00	> 27.3	...	...	> 1.3	3.084
073	22:17:39.12	0:17:11.7	26.35	> 27.3	...	...	> 2.4	3.083
074	22:17:36.47	0:12:54.8	26.16	25.52	0''1	0''7	0.6 ± 0.2	3.105
075	22:17:22.97	0:11:25.8	> 27.0	> 27.3	...	...	...	... <sup>i</sup>
076	22:17:20.67	0:15:13.2	> 27.0	> 27.3	...	...	...	3.066
077	22:17:37.95	0:11:01.3	26.01	26.36	0''2	1''1	...	... <sup>g</sup>
078	22:17:37.68	0:16:48.3	25.95	> 27.3	...	...	> 3.5	3.090
079	22:17:34.68	0:11:10.5	> 27.0	> 27.3	...	...	...	3.103
080	22:17:35.95	0:13:43.3	> 27.0	> 27.3	...	...	...	3.104
081	22:17:29.22	0:14:48.7	> 27.0	26.79	0''6 <sup>j</sup>	0''7	< 1.2	3.104
082	22:17:35.44	0:16:47.6	> 27.0	> 27.3	...	...	...	3.087
083	22:17:28.46	0:12:08.9	26.46	26.84	0''4	0''6	1.4 ± 0.7	3.065
084	22:17:19.90	0:15:14.9	> 27.0	26.50	0''1	0''8	...	... <sup>i</sup>
085	22:17:30.86	0:14:38.2	26.94	> 27.3	...	...	...	... <sup>i</sup>
086	22:17:28.42	0:13:42.8	> 27.0	> 27.3	...	...	...	3.100
087	22:17:37.07	0:13:21.5	> 27.0	27.26	0''1 <sup>j</sup>	1''6	...	... <sup>g</sup>
088	22:17:38.45	0:13:18.3	> 27.0	> 27.3	...	...	...	... <sup>i</sup>
089	22:17:38.54	0:15:22.5	26.59	> 27.3	...	...	...	... <sup>i</sup>
090	22:17:18.25	0:14:06.4	> 27.0	> 27.3	...	...	...	3.095
091	22:17:36.14	0:15:40.7	> 27.0	> 27.3	...	...	...	3.095
092	22:17:23.97	0:15:27.8	> 27.0	> 27.3	...	...	...	... <sup>i</sup>
093	22:17:27.48	0:13:57.5	26.35	> 27.3	...	...	> 2.4	3.106
094	22:17:39.14	0:17:00.6	> 27.0	> 27.3	...	...	...	... <sup>i</sup>
095	22:17:37.19	0:13:28.0	26.17	> 27.3	...	...	> 2.8	3.094
096	22:17:38.93	0:11:37.4	26.64	26.45	0''6	0''6	...	... <sup>g</sup>
097	22:17:27.11	0:14:08.7	> 27.0	> 27.3	...	...	...	3.064
098	22:17:24.01	0:13:19.5	> 27.0	> 27.3	...	...	...	... <sup>g</sup>
099	22:17:36.46	0:13:00.3	> 27.0	> 27.3	...	...	...	3.102
100	22:17:30.61	0:18:11.6	> 27.0	> 27.3	...	...	...	... <sup>i</sup>
101	22:17:25.33	0:17:22.5	26.89	26.58	0''2	1''4	...	... <sup>g</sup>
102	22:17:24.00	0:16:27.6	25.91	26.05	0''1	0''2	...	... <sup>g</sup>
103	22:17:19.40	0:15:26.1	> 27.0	> 27.3	...	...	...	3.099
104	22:17:37.66	0:12:55.5	> 27.0	> 27.3	...	...	...	3.097
105	22:17:35.46	0:12:23.9	26.81	> 27.3	...	...	> 1.6	3.104
106	22:17:22.86	0:17:57.8	26.16	> 27.3	...	...	...	... <sup>i</sup>
107	22:17:20.96	0:14:46.7	26.57	> 27.3	...	...	> 2.0	3.075
108	22:17:24.78	0:17:40.4	26.84	> 27.3	...	...	> 1.5	3.100
109	22:17:23.98	0:17:57.8	26.77	> 27.3	...	...	...	... <sup>g</sup>
110	22:17:19.50	0:15:57.6	> 27.0	> 27.3	...	...	...	3.074



TABLE 3  
 SUMMARY OF LAE DATA (*Continued*)

ID	RA (J2000)	Dec (J2000)	$R$	NB3640	$\Delta_R^a$	$\Delta_{LyA}^a$	$\frac{F_{UV}}{F_{LyC}}^b$	$z_{em}^c$
111	22:17:31.14	0:16:42.9	> 27.0	> 27.3	...	...	...	3.096
112	22:17:32.72	0:15:54.2	> 27.0	> 27.3	...	...	...	3.096
113	22:17:24.80	0:13:26.9	> 27.0	> 27.3	...	...	...	3.069
114	22:17:34.50	0:14:20.0	> 27.0	> 27.3	...	...	...	3.103
115	22:17:33.46	0:17:01.2	> 27.0	> 27.3	...	...	...	3.093
116	22:17:28.00	0:12:14.2	> 27.0	> 27.3	...	...	...	3.096
117	22:17:39.08	0:12:01.9	> 27.0	> 27.3	...	...	...	3.098
118	22:17:35.28	0:10:59.9	26.20	26.11	0''4	1''4	...	... <sup>g</sup>
119	22:17:25.63	0:12:47.8	> 27.0	> 27.3	...	...	...	3.071
120	22:17:26.76	0:10:59.8	> 27.0	> 27.3	...	...	...	3.079
121	22:17:26.44	0:15:27.5	> 27.0	> 27.3	...	...	...	3.099
122	22:17:38.19	0:14:03.7	> 27.0	> 27.3	...	...	...	3.106
123	22:17:35.06	0:17:26.0	> 27.0	> 27.3	...	...	...	... <sup>i</sup>
124	22:17:22.80	0:17:48.7	> 27.0	> 27.3	...	...	...	... <sup>g</sup>
125	22:17:38.02	0:14:03.6	26.79	> 27.3	...	...	> 1.6	3.101
126	22:17:19.53	0:16:48.2	> 27.0	> 27.3	...	...	...	... <sup>i</sup>
127	22:17:36.91	0:11:27.1	> 27.0	> 27.3	...	...	...	3.107
128	22:17:23.43	0:16:07.4	> 27.0	> 27.3	...	...	...	3.095
129	22:17:22.28	0:10:57.9	> 27.0	> 27.3	...	...	...	3.111
130	22:17:32.84	0:16:48.8	> 27.0	> 27.3	...	...	...	3.092

<sup>a</sup> Spatial offset between the centroids of  $R$  or  $Ly\alpha$  and NB3640 emission.

<sup>b</sup> Observed ratio and uncertainty in non-ionizing UV and LyC flux densities, inferred from the NB3640– $R$  color. This value has not been corrected for either contamination by foreground sources or IGM absorption.

<sup>c</sup> Spectroscopic redshift based on the observed wavelength of  $Ly\alpha$  emission.

<sup>d</sup> Objects that are also identified as LBGs. 001 is LBG D3; 002 is LBG C4; 004 is LBG MD23; 008 is LBG C28; 009 is LBG C9; 012 is LBG M28; 029 is LBG M13.

<sup>e</sup> Objects with previously-known spectroscopic redshifts.

<sup>f</sup> Spectrum contains evidence for the presence of a foreground galaxy. Thus, we do not consider the NB3640 detection to be LyC flux.

<sup>g</sup> Objects with LRIS spectroscopic observations but without confirmed redshifts.

<sup>h</sup> The redshift of this LAE is such that some non-ionizing UV flux will contribute to the NB3640 detection, and therefore we exclude it from our LyC detection sample.

<sup>i</sup> Objects without LRIS spectroscopic observations.

<sup>j</sup> Offset determined from the centroid of the  $BV$  detection.

TABLE 4  
SAMPLE AVERAGE COLORS AND UV TO LYC FLUX DENSITY RATIOS.

Correction	LBGs $\langle \text{NB3640} \rangle - \langle R \rangle^a$	$\eta^b$	LAEs $\langle \text{NB3640} \rangle - \langle R \rangle^a$	$\eta^b$
Full Ensembles <sup>c</sup>				
none	$3.74^{+0.66}_{-0.42}$	$31.5^{+26.4}_{-10.0}$	$2.13^{+0.36}_{-0.29}$	$7.1^{+2.8}_{-1.7}$
contamination <sup>d</sup>	$4.45^{+1.16}_{-0.56}$	$60.5^{+115.4}_{-24.2}$	$2.66^{+0.56}_{-0.39}$	$11.6^{+7.8}_{-3.5}$
IGM + contamination <sup>e</sup>	$3.14^{+1.17}_{-0.57}$	$18.0^{+34.8}_{-7.4}$	$1.42^{+0.57}_{-0.40}$	$3.7^{+2.5}_{-1.1}$
Full Ensembles, maximum allowed flux for NB3640 non-detections <sup>f</sup>				
none	$3.40^{+0.43}_{-0.32}$	$23.0^{+11.0}_{-5.8}$	$1.90^{+0.29}_{-0.25}$	$5.7^{+1.7}_{-1.2}$
contamination <sup>d</sup>	$3.84^{+0.48}_{-0.34}$	$34.4^{+19.3}_{-9.3}$	$2.28^{+0.37}_{-0.29}$	$8.2^{+3.3}_{-1.9}$
IGM + contamination <sup>e</sup>	$2.53^{+0.51}_{-0.37}$	$10.2^{+6.1}_{-3.0}$	$1.04^{+0.38}_{-0.31}$	$2.6^{+1.1}_{-0.6}$
NB3640 detections only				
none	$1.77^{+0.67}_{-0.63}$	$5.1^{+4.4}_{-2.3}$	$0.29^{+0.41}_{-0.39}$	$1.3^{+0.6}_{-0.4}$
contamination <sup>d</sup>	$1.89^{+0.75}_{-0.66}$	$5.7^{+5.7}_{-2.6}$	$0.33^{+0.46}_{-0.42}$	$1.4^{+0.7}_{-0.4}$
IGM + contamination <sup>e</sup>	$0.57^{+0.77}_{-0.68}$	$1.7^{+1.7}_{-0.8}$	$-0.91^{+0.47}_{-0.43}$	$0.4^{+0.2}_{-0.1}$

<sup>a</sup> Color determined from average NB3640 and  $R$ -band fluxes. Uncertainties include individual flux and sample uncertainties.

<sup>b</sup> Ratio and uncertainty in non-ionizing UV and LyC flux density inferred from  $\langle \text{NB3640} \rangle - \langle R \rangle$  color.

<sup>c</sup> Color and flux-density ratio determined assuming NB3640 non-detections contribute zero LyC flux.

<sup>d</sup> Color and flux-density ratio after statistically correcting sample for foreground contamination of NB3640 fluxes.

<sup>e</sup> Color and flux-density ratio after correcting sample for foreground contamination and IGM absorption of NB3640 fluxes.

<sup>f</sup> Color and flux-density ratio determined assuming NB3640 non-detections contribute the maximum possible LyC flux consistent with our limits from stacking analysis.

TABLE 5  
CONTRIBUTIONS TO THE IONIZING BACKGROUNDS.

	LF <sup>a</sup>	$\eta^b$	Magnitude range <sup>c</sup>	$\epsilon_{\text{LyC}}^d$
(i)	LBG	$18.0^{+34.8}_{-7.4}$	$M_{AB} \leq -20.0$	$5.2^{+3.6}_{-3.4}$
(ii)	LAE	$3.7^{+2.5}_{-1.1}$	$-20 < M_{AB} \leq -18.3$	$6.7^{+2.8}_{-2.7}$
(iii)	LBG	$3.7^{+2.5}_{-1.1}$	$-20 < M_{AB} \leq -18.3$	$27.0^{+11.4}_{-10.9}$
(iv)	LBG	$18.0^{+34.8}_{-7.4}$	$M_{AB} \leq -18.3$	$10.7^{+7.5}_{-7.1}$
(v)	LAE	$3.7^{+2.5}_{-1.1}$	$M_{AB} \leq -18.3$	$8.6^{+3.7}_{-3.5}$
	Total (lum.-dep.) <sup>e</sup>	...	$M_{AB} \leq -18.3$	$32.2^{+12.0}_{-11.4}$
	Total (LAE-dep.) <sup>f</sup>	...	$M_{AB} \leq -18.3$	$16.8^{+6.9}_{-6.5}$

<sup>a</sup> Luminosity function parameters used in Equations 3–5: LBG from Reddy et al. (2008); or LAE from Ouchi et al. (2008) scaled to include LAEs having  $\text{REW} \geq 20\text{\AA}$ .

<sup>b</sup> Sample average flux-density ratio used in Equations 3–5.

<sup>c</sup> Magnitude range over which the first moment of the luminosity function is determined.  $M_{AB} = -20.0$  and  $-18.3$  correspond to  $0.46L_{LBG}^*$  and  $0.1L_{LBG}^*$ , respectively.

<sup>d</sup> Comoving specific emissivity of ionizing radiation in units of  $10^{24} \text{ ergs s}^{-1} \text{ Hz}^{-1} \text{ Mpc}^{-3}$ .

<sup>e</sup> Totals for our luminosity-dependent  $\eta$  model, determined by summing rows (i) and (iii).

<sup>f</sup> Total for our LAE-dependent  $\eta$  model, determined by summing  $0.77 \times$  row (iv) and row (v).

TABLE 6  
 ESTIMATES OF THE INTERGALACTIC HYDROGEN  
 PHOTOIONIZATION RATE AT  $z \simeq 3.1$ .

Reference	$\Gamma$ ( $\times 10^{-12} \text{s}^{-1}$ )
Meiksin & White (2004)	$0.88^{+0.14}_{-0.12}$
Bolton & Haehnelt (2007)	$0.86^{+0.34}_{-0.26}$
Faucher-Giguère et al. (2008)	$0.63 \pm 0.08$
This work, luminosity-dependent $\eta$	$2.7^{+1.0}_{-0.9}$
This work, LAE-dependent $\eta$	$1.4^{+0.6}_{-0.6}$

 TABLE 7  
 MODEL DEPENDENT INFERRED VALUES FOR  $f_{esc}^{LyC}$ .

Age (yr) <sup>c</sup>	$Z$ <sup>d</sup>	BC03 <sup>a</sup>			BPASS <sup>b</sup>		
		$\eta^{stars}$ <sup>e</sup>	$f_{esc}^{LyC, LBG}$ <sup>f</sup>	$f_{esc}^{LyC, LAE}$ <sup>g</sup>	$\eta^{stars}$ <sup>e</sup>	$f_{esc}^{LyC, LBG}$ <sup>f</sup>	$f_{esc}^{LyC, LAE}$ <sup>g</sup>
$f_{esc}^{UV} = 0.2$							
$10^6$	0.004	1.98	0.02	0.11	1.33	0.01	0.07
...	0.020	1.90	0.02	0.10	1.45	0.02	0.08
$10^7$	0.004	3.59	0.04	0.19	2.10	0.02	0.11
...	0.020	4.20	0.05	0.23	2.70	0.03	0.15
$10^8$	0.004	6.17	0.07	0.33	3.16	0.04	0.17
...	0.020	6.38	0.07	0.34	4.43	0.05	0.24
$f_{esc}^{UV} = 0.3$							
$10^6$	0.004	1.98	0.03	0.16	1.33	0.02	0.11
...	0.020	1.90	0.03	0.15	1.45	0.02	0.12
$10^7$	0.004	3.59	0.06	0.29	2.10	0.04	0.17
...	0.020	4.20	0.07	0.34	2.70	0.05	0.22
$10^8$	0.004	6.17	0.10	0.50	3.16	0.05	0.26
...	0.020	6.38	0.11	0.52	4.43	0.07	0.36
$f_{esc}^{UV} = 1.0$							
$10^6$	0.004	1.98	0.11	0.54	1.33	0.07	0.36
...	0.020	1.90	0.11	0.97	1.45	0.08	0.39
$10^7$	0.004	3.59	0.20	$> 1$	2.10	0.12	0.57
...	0.020	4.20	0.23	$> 1$	2.70	0.15	0.73
$10^8$	0.004	6.17	0.34	$> 1$	3.16	0.18	0.85
...	0.020	6.38	0.35	$> 1$	4.43	0.25	$> 1$

<sup>a</sup> Stellar population synthesis models of Bruzual & Charlot (2003).

<sup>b</sup> Stellar population synthesis models of Eldridge & Stanway (2009).

<sup>c</sup> Time since turn on of constant star formation.

<sup>d</sup> Metallicity of stellar population.

<sup>e</sup> Ratio of intrinsic  $F_{1600}$  to  $F_{NB3640}$  predicted by model.

<sup>f</sup> Resulting LyC escape fraction for the given UV escape fraction, using  $\eta_{LBG}$ .

<sup>g</sup> Resulting LyC escape fraction for the given UV escape fraction, using  $\eta_{LAE}$ .